TECHNISCHE UNIVERSITÄT DRESDEN

Fakultät Maschinenwesen Institut für Verfahrenstechnik und Umwelttechnik

Professur für Transportprozesse an Grenzflächen

Rare Earth Technology: Magnetic Cooling and Magnetic Separation

Von der
Fakultät Maschinenwesen
der
TECHNISCHEN UNIVERSITÄT DRESDEN
eingereichte

D i s s e r t a t i o n

zur Erlangung des akademischen Grades
Doktor-Ingenieur (Dr.-Ing.)

M.Sc. Zhe Lei
geb. am 18.11.1988 in Shaanxi, China

Erster Gutachter:	Prof. Dr. rer. nat. et Ing. habil. Kerstin Eckert
Zweiter Gutachter:	Prof. Andrej Kitanovski
Vorsitzender:	Prof. Dr. rer. nat. habil. Stefan Odenbach
Mitglieder:	Prof. Dr. rer. nat. et Ing. habil. Christoph Haberstroh
Mitglieder:	Prof. Dr. –Ing. habil. Rüdiger Lange
Tag der Einreichung:	29.09.2017
Tag der Verteidigung:	26.03.2018

This dissertation is dedicated to my beloved parents.
In memory of the gains and pains along the path ...

Abstract

This dissertation deals with two prospectives of rare earth technology. It's application in magnetic cooling as well as its harvesting and recycling phase. The emphasis is on mapping and manipulating the transport processes of energy and mass, during magnetic cooling and rare earth magnetic separation, under the influence of magnetic field. Distinguished by the driving force of flow field, they belong to the context of magnetohydrodynamics and ferrohydrodynamics, respectively.

Multiple aspects are investigated with respect to magnetic cooling. First, the transient dynamics of heat transfer from two periodically magnetized gadolinium (Gd) plates into a heat transfer fluid (n-decane) is studied. It demonstrates that the propagation of the thermal fronts emanating from the Gd plates after magnetization or demagnetization obeys a $\sqrt{t}$-dependence. A finite time required for magnetization and demagnetization causes a spatially delayed propagation of the thermal fronts. The diffusive heat flux, derived from the temperature profiles, experiences a drop down by about 80% after first 3 seconds while the percentage of thermal energy transferred into n-decane experiences a maximum there. With a stagnant fluid, this work provides reasons for lower bounds of geometry and operation frequency of a simplified parallel-plate structure in the diffusive limit. Furthermore, the potential of magnetohydrodynamic (MHD) convection to increase heat transfer during magnetic cooling is tested. To do this, a section of an active magnetic regenerator is considered, namely a flat gadolinium plate, immersed in an initially stagnant heat transfer fluid (NaOH) which is placed in a cuboid glass cell. To create the MHD flow, a small electric current is injected by means of two electrodes and interacts with the already present magnetic field. As a result, a Lorentz force is generated, which drives a swirling flow in the present model configuration. By means of particle image velocimetry and Mach-Zehnder interferometry, the flow field and its impact on the heat transfer at the gadolinium plate is analyzed. For the magnetization stage, a heat transfer enhancement by about 40 % can be achieved even with low currents of 3 mA is found. In parallel to enhance the heat transfer by an actively stirring of the heat transfer fluid by means of MHD, alternative fluid candidate is also investigated. A room temperature eutectic liquid metal GaInSn, with superior Pr$\approx$ 0.03, and comparable viscosity like that of water is tested in a segment of parallel plate AMR. Due to the high electric conductivity,

velocity field of GaInSn contrasting to that of aqueous based ones is strongly influenced by magnetic field due to Lorentz force. Therefore, preliminary velocity measurements by means of ultrasound doppler velocimetry with a quasi homogeneous static magnetic field (220 mT) in a duct channel at the non-conducting Shercliff walls are conducted. The Hartmann walls are constituted of two parallel Gd plates.

The second part of this dissertation, rare earth harvesting and recycling, aims to answer the question of why an enrichment of paramagnetic ions can be observed in a magnetic field gradient despite the presence of a counteracting Brownian motion. For that purpose, a rare-earth chloride (DyCl3) solution is studied in which weak evaporation is adjusted by means of small differences in the vapor pressure. The temporal evolution of the refractive index field of this solution, as a result of heat and mass transfer, is measured by means of a Mach–Zehnder interferometer. A numerical algorithm is developed that splits the refractive index field into two parts, one space-dependent and conservative and the other time-dependent and transient. By using this algorithm in conjunction with a numerical simulation of the temperature and concentration field, it is able to show that 90% of the refractive index in the evaporation-driven boundary layer is caused by an increase in the concentration of Dy(III) ions. A simplified analysis of the gravitational and magnetic forces, entering the Rayleigh number, leads to a diagram of the system's instability. Accordingly, the enrichment layer of elevated Dy(III) concentration is placed in a spatial zone dominated by a field gradient force. This leads to the unconditional stability of this layer in the present configuration. The underlying mechanism is the levitation and reshaping of the evaporation-driven boundary layer by the magnetic field gradient.

Acknowledgements

First of all, I would like to thank my PhD mentor Prof. Kerstin Eckert for her overall instruction throughout my PhD period in Dresden. With the freedom offered, I could dedicate liberally my main energy to the investigation of my projects. This ensures a rapid development in advancing my research potential in both scientific and engineering prospectives. The peaks among the moments that I cherish most are when I am shown how to logically sorting my excessive among of thoughts that could not converge to a clear blueprint.This is especially true in bring my findings in a manuscript format which requires not only high quality scientific results but clearly written texts with certain degree of elegancy. Especially, I appreciate the apprentice way of receiving those guidance.With all these experiences, I gradually learned the value of briefing and trimming the exploding thoughts in a logical and organized form with the merit of slowing down.

I am grateful to have worked with different research communities that are both transparent and communicative. I thank the talented and honorable scientists that I have met and communicated with. Each of them inspired me in different prospectives thus the integrated effect is remarkable on me. I appreciate:

Prof. Stefan Odenbach from TU Dresden for chairing my first 3 years of PhD period. I have learnt the fundamentals of ferrofluid and ferrohydrodynamics over the years in group discussions. Dr. Sven Eckert from HZDR for 10 months of co-chair my work when I carry out the liquid metal research in the experimental magnetohydrodynamic department. Prof. Michael Coey from Trinity College, Dublin for sharing me how important it is to enjoy science before building up a research based career. Prof. Dirk Lindackers from IFW in Dresden for showing me the concrete and rigorous German engineering supporting the German scientific community. Prof. Andrej Kitanovski for the communication in the prototype and engineering side of magnetic cooling research and the prospective research collaboration opportunity; Prof. Oliver Gutfleisch for the material side instruction regarding magnetic cooling; Dr. Kurt Engelbrecht and Dr. Christian Bahl from DTU for the showing me their magnetic cooling prototypes and offering possibility in future collaboration in testing MHD concept in real AMR.

Over the years, I have got the opportunities to work closely with scientists from different backgrounds. These "intimate" experiences defined my current understanding of professional attitude in research. I thank:

Dr.-Ing.Dirk Raebiger from HZDR for organizing the ultrasounic gears and the engineering details on the design of liquid metal duct channel flow. Dr. Natasha Shevchenko from HZDR for showing me the fantastic world of solidification. Dr. Joerg Grenzer for showing me the spectrum of light that is different from what I use. And showing me how important for scientists to get their hand dirty and struggle with the harsh condition for good scientific results. Thanks Kevin Maeder for the discussion in UDV techniques.

Colleagues with whom I conduct my daily routine together are acknowledged and appreciated:

Dr.-Ing. Hieram Neumann-Heyme for being 3 years of officemate with me. It is so much fun to work overtime together. The divergent thinking that both of us cherish or characterize makes our discussion both in scientific topics and life themes so fruitful. Thanks Barbara Fritsche for co-developing the magnetic separation work and a lot of discussions on both magnetic cooling and magnetic separation. Every colleagues who give me feedback on my defense presentation. Special thanks to Dr.-Ing. Karin Schwarzenberger, Dr.-Ing. Sascha Heitkam for the structural revision tips; Tobias Lappan for information of REE in a material prospective and Thomas Richter for formality tips. Dr. Xuegeng Yang for inviting me to taste Chinese food at his house which I miss from time to time. Bordeaux team of parabolic flight for showing me how robust the format a scientist must design their systems to. All the redundant engineering requirements eventually turned out to be essential for a both a better and safe operation system on board the plane.

China Scholarship Council (CSC) is acknowledged for providing 48 months of scholarship which makes my PhD initially possible. Deutsches Zentrum für Luft- und Raumfahrt (grant no. 50WM1350) is acknowledged for providing the funding for magnetic separation research.

I am grateful for the degree of transparency and internationality of the science and research community nowadays. It is science that provides the initial chance for me to step out of China and see the world which is as beautiful and fascinating as the place I was born and raised. I felt really lucky to have kept the curiosity and open mindedness towards the splendid world.

Thanks to the ones who loves me, you make who I am. Thanks to the ones who I love, you define the meaning of my life.

Thanks to my parents. Nothing about me could exist without you! I love you!

Table of contents

Chapter 1

Introduction

Rare earth elements (REE) are 17 chemical elements in chemical periodic table comprising 15 lanthanides plus scandium and yttrium. They are not rare in term of their abundance. Yet they tend to occur in the same ore in which they are sparsely distributed. World storage of rare earth is approximately 130 million tons. The primary storage is in China with a 42.3 % of the total amount. Brazil has around 16.9 % making it the second largest in terms of storage. Other dominant countries include Australia, USA and India [1]. For the supply side on the other hand, REE are chiefly distributed by China, with 84.7 % among overall 124 kiloton produced per year, and the amount of mining and production remains almost unchanged for the past 10 years [1–3]. Since the REE are distributed to different ores and typically occuring in low concentrations, complicated processes for REE separation and harvesting are mandatory.

Ore obtained from mining undergoes crushing, milling, flotation, separation into oxide form and is finished with reduction reaction. Yet, due to the relative high cost and immature technology, current REE recycling rates are low.

REE have been used in a broad range of mature applications, namely increasing strength of structural material while minimizing its density [4]; acting as novel catalysts with superior performance under certain conditions [5, 6]; acting as additives to glass for absorbing ultraviolet light or tuning refractive index; used as luminescent materials [7], etc.

Besides, novel green technologies relying on REE are developed facing uprising concerns about negative impact of the human activities on environment, cf. UNFCCC [8]. Wind turbine, which convert the wind energy to electric energy uses permanent magnet with high energy density to miniaturizing their size. Mobility relies on permanent magnet in electric motors instead of combustion engines to save non-recyclable fossil energy and eliminate emission on the road at the same time [9]. Both technologies demand large amount of neodymium iron boron permanent magnet which was discovered by Dr. Sagawa in 1978.

It delivers the highest energy density among dominant hard magnetic materials [10]. This permanent magnet requires large portion of neodymium and praseodymium with dysprosium as an additive to maintain performance in high temperature application. For hybrid cars, nickel metal hydride (NiMH) batteries are already maturally developed and applied. These batteries are constituted of multiple REE such as lanthanum, cerium, neodymium, praseodymium. Besides, storage system like hard disk also depend on permanent magnet [11]. Additional to these industrial widely adopted environmental friendly technologies based on permanent magnet, emerging ones such as magnetic cooling [12–14] are also actively studied at academic level and pending for further development and optimization. Magnetic cooling is the most promising alternative cooling technology to ease the tension on global warming. Hence a well developed procedure for beneficiation and upgrading of rare earth from raw ore and purification [15] is needed to feed the application.

Yet, green technology is not equivalent to an entire chain of clean and environmental friendly procedure. To some extend, the pollution is relocated from application phase to the production phase. Vast amount of pollution issues are reported on the factory for mining and processing of rare earth. Large amount of environmentally unfriendly organic based extracting agent during the separation and purification process intensifies this issue. This is further limited by the cost-inefficient recycling of used products. Therefore, necessity exists for developing novel separation and recycling technology in case of a future increase in the raw material price and shortage of supply. This dissertation wants to contribute to these issues by dealing with two important aspects of REE:

- REE application in magnetic cooling
- REE separation with permanent magnet

The first part deals with an improvement of the coefficient of performance (COP) in magnetic cooling devices by enhancing the heat transfer inside the active magnetic regenerator, i.e. solid state refrigerant and heat transfer fluid filled in between. The second part proposes and investigates the mechanism underlying a novel separation of REE from an initially homogeneous solution using permanent magnet.

The two parts of the dissertation have a strong bracket. Central aim is the manipulation of transport processes in liquid phase. This is achieved by applying electric field and/ or magnetic field which generate two body forces, namely the Lorentz force and the Kelvin force. Furthermore, interferometry is the primary measurement system used in both parts to analyze the transport of heat and mass.

Before going into the details, an introduction into magnetic cooling and magnetic separation is given on the next pages.

1.1 Rare earth element (REE) application in magnetic cooling

Magnetic cooling (MC) is an emerging alternative cooling technology [16] which offers certain advantages [13, 17, 18] compared to conventional cooling based on gas compression. It has the potential of high efficiency, compact design and silent operation ensured by the replacement of compressor with magnet. It maintains a possibility to use an environmentally friendly heat transfer fluid. Furthermore, it promises the use of solid state cooling material which has theoretically zero ozone depletion potential (ODP) and zero global warming potential (GWP) due to the essentially zero emission and zero vapor pressure. This subsection is dedicated to the working principle, thermodynamic theories of magnetic cooling and current state of art of magnetic cooling prototypes.

1.1.1 Magnetocaloric effect

Magnetic cooling is a technology to continuously bring heat from a cold source to a warm source using a magnetocaloric effect (MCE). This refers to a temperature change of a magnetocaloric material (MCM) when it is exposed to a varying magnetic field. This was first discovered in iron [19] and later found to be an intrinsic phenomenon for all magnetic materials. A direct vision into this phenomonon, under constant pressure, is through the entropy equation

$$S(T,B) = S_m(T,B) + S_{lat}(T) + S_{el}(T). \tag{1.1}$$

$S(T,H)$ is the total entropy, $S_m(T,H)$ is the magnetic entropy, $S_{lat}(T)$ is the lattice entropy and $S_{el}(T)$ is the electronic entropy. For certain material with a high electronic specific heat, e.g. Sc, $CeCu_2Si_2$, the dependence of electronic entropy on magnetic field has to be considered[20]. An applied external magnetic field reduces the magnetic disorder hence the magnetic entropy term. Such loss is compensated via lattice entropy and electric entropy term. Since the later two terms are both function of temperature, the material exhibits a warming up. Given an adiabatic condition, the temperature change ΔT_{ad} is at its maximum for a given temperature and reaches a plateau near its Curie temperature T_c. Reversely, the same holds a decreasing external magnetic field. MCM undergoes a cooling when it is being demagnetized.

The magnetocaloric effect is defined as

$$dS(T,B) = (\frac{\partial S(T,B)}{\partial T})_B dT + (\frac{S(T,B)}{\partial B})_T dB. \tag{1.2}$$

Given isothermal conditions, the magnetic entropy change ΔS_m is maximum. Integrating Eq. (1.2) under isothermal condition, the entropy change in MCE is obtained. Together with $(\frac{\partial S(T,H)}{\partial B})_T = (\frac{\partial M(T,B)}{\partial T})_B$ according to the exact differential character of Gibbs free energy,

$$\Delta S_m = \int_{B_0}^{B_1} (\frac{\partial M(T,B)}{\partial T})_B dB \tag{1.3}$$

is obtained.

On the other hand, if isentropic conditions are fulfilled, the temperature increase achieves its maximum, ΔT_{ad}, given an increasing applied magnetic field. By introducing thermodynamic correlation of heat capacity at constant magnetic field

$$C_B(T,B) = T(\frac{\partial S(T,B)}{\partial T})_B, \tag{1.4}$$

the adiabatic temperature ΔT_{ad} is obtained by integrating

$$dT = -\frac{T}{C_B(T,B)}(\frac{\partial M(T,B)}{\partial T})_B dB \tag{1.5}$$

as

$$\Delta T_{ad} = \int_{B_0}^{B_1} -\frac{T}{C_B(T,B)}(\frac{\partial M(T,B)}{\partial T})_B dB \tag{1.6}$$

Both ΔT_{ad} and ΔS_m, see Eq. (1.6) and (1.3), are directly correlated with the magnetization M, the iso-magnetic field heat capacity C_B and the temperature T. Both parameters evaluate the intensity of magnetocaloric effect. They can be measured directly, e.g. ΔT_{ad}, or indirectly calculated by measuring heat capacity or magnetization during the MCE. The above calculation works fine with magnetocaloric effect based on second order phase transition [21]. It refers to a new state of reduced symmetry which develops continuously from the disordered phase (high temperature), i.e. a non-sharp para-ferro phase transition [22, 23] with an instantaneous response in nanoseconds [12]. The equations are relevant also for MCE with first order phase transition, shart change of M at transition temperature, without hysteresis [24, 25].

On the other hand, the shape of MCM and the direction of applied magnetic field also influence the magnitude of MCE by the so called demagnetization field. To start with, Ampere's law neglecting displacement current in dielectric polarized term is

$$\nabla \times \vec{B} = \mu_0(\vec{j_c} + \vec{j_m}). \tag{1.7}$$

By letting $\vec{j_c}$ and $\vec{j_m}$ to be the curl of the auxiliary field and the magnetization, respectively, constitutive Eq. (1.8) is formed which relates the magnetic field B, the auxiliary field H and the magnetization M in a magnetic material

$$\vec{B} = \mu_0(\vec{H} + \vec{M}). \tag{1.8}$$

Consider another material exposed to an external field, $\vec{H_{ext}}$, e.g. stray field of a magnet. When the magnetization of the material is big enough, the auxiliary field of the magnetized magnetic material is impaired

$$\vec{H_{int}} = \vec{H_{ext}} + \vec{H}_d \tag{1.9}$$

where the second term is created by the magnetization distribution of the magnetic material known as demagnetization field inside or stray field outside the magnetized material. Inside the magnetic material, $\vec{H}_d$ is directed opposing the magnetization direction. The demagnetization field in a magnetized material with special shape such as an ellipsoid is homogeneous. A general relation between $\vec{H}_d$ and $\vec{M}$ is $\vec{H}_d = -N_{ij}M_j$ connected by a demagnetizing tensor N_{ij}. The principle components (N_{11}, N_{22}, N_{33}) are the demagnetizing factors, and their sum equals to unity. The demagnetization field has a considerable effect on the MCE. All calculation results of MCE, irrespectively on whether the Weiss mean field model, the Debye model or Sommerfeld model [26, 27] is used, exhibit a better agreement with the experiments when the demagnetization factor is taken into account [28, 29]. The influence of demagnetization field on magnetocaloric effect is also relevant in the present work and addressed in chapter 3.

Gadolinium (Gd) is widely used as a benchmark MCM since the pioneering work of Brown [30]. It is one of REE and has a relatively high MCE of about $\approx$ 3 K/T. The disadvantage is that it belongs to the heavy REE group, hence it is not cheap and easily corrosive. Both issues motivated material scientists to synthesize and evaluate novel replacement MCMs based on first or second order phase transition [17, 22, 31–34]. The magnetocaloric effect of Gd was studied extensively by researchers around the world. It has been shown that even a small amount of impurity can result in a remarkable decrease in MCE. A maximum of ΔT_{ad} = 3.6 K is measured at the Curie temperature T_c = 292.5 K [35]. A diminished MCE with 7% of reduction is found in slightly less pure material with 99.49% compared to 99.99% pure in a pulsed magnetic field from 0 to 2 T [36]. Besides, Curie temperature is tuned by a slight difference in the impurity both in its content type and the amount [36]. Crystalline structure also influences Curie temperature of Gd, e.g. the value in mono-crystalline Gd is 9 K higher than in a multi-crystalline structure[37]. Furthermore, the response of ΔT_{ad} to an applied field is more linear in multi-crystalline than that of single-crystalline Gd. By contrast, multi-crystalline Gd exhibits an impaired MCE with a higher magnetic flux density [38].

Hence, the experimental results of properties measurement are highly sample depending. Thus, a direct comparison of prototype machines with Gd from different source, i.e. slightly differs in their content, are therefore impossible due to the diverging MCE.

1.1.2 Active magnetic regenerator

Even for the benchmark MCM gadolinium(Gd), the maximum value of MCE of about 3.6 K/T [35] is not enough for refrigeration application. This is further limited by the magnetic field maximum O(2 T) provided nowadays by highest magnetization NdFeB permanent magnet with Halbach arrangement offering the highest flux density in its surrounding region [39, 40]. A direct transfer of MCM to cooling power near room temperature remained impossible until the concept of active magnetic regenerator (AMR) was developed by Barclay [41] in 1982. The core of the AMR is a porous structure made up of MCM, frequently realized as a packed sphere bed or as an ensemble of flat parallel plates, and filled with heat transfer fluid. The thermodynamic cycle depends highly on the machine, e.g. Stirling cycle in passive regenerator [42], magnetic Ericsson cycle in passive regeneration [43]. Comprehensive reviews were reported by Kitanovski and Gutfleisch [44, 45]. The most relevant AMR cycle is the magnetic Brayton cycle. One complete cycle for a single fraction of MCM consists of 1) an isentropic magnetization of the MCE, 2) a heat transfer fluid blow from the cold to hot end, 3) an isentropic demagnetization and 4) a fluid blow from the cold to the hot end, cf. Fig. 1.1. Using the AMR, a larger temperature span T_{span} than just the adiabatic temperature change ΔT_{ad} can be obtained. Each fraction of MCM undergoes the thermodynamic cycle at different initial temperature and its mean temperature forms a gradient along cold end to hot end, cf. Fig. 1.1b. This is the basis of near-room-temperature refrigeration, as was first demonstrated in [46].

The development of a rotating magnetic refrigerator by [47] and further advances as reviewed in Ref. [48] render the technology closer to a commercialized state. Based on the AMR principle, there has been at least 62 prototypes built. A general review of near-room-temperature MC prototypes can be found in [13, 18, 44, 49, 50]. The optimization of the system is a systematic research. But in general, 3 general aspects are pending for further advancements.

1. MCM material challenge and novel material synthesis
   a. High heat capacity with a low Debye temperature
   b. High magnetocaloric effect at working temperature
   c. No thermal or magnetic hysteresis
   d. Good mechanical properties and good resistance to corrosion

e. Low electric conductivity to avoid eddy current in fast changing magnetic fields
f. Low cost

2. Heat transfer inside the regenerator
   g. Good heat exchange between MCM and heat transfer fluid
   h. Low pumping power for heat transfer fluid oscillating between hot and cold end

3. High energy density achieved by optimization of magnetic field

1.1.3 Heat transfer in an active magnetic regenerator

In contrast to gas compression refrigerators, the refrigerant in magnetic cooling is not identical to the heat transfer fluid. Making an extra challenge of magnetic cooling machines is the additional heat transfer from the refrigerant (MCM) to the heat transfer fluid in the AMR. Hence, the optimization of the performance of the AMR is of primary importance. Precondition for this is an efficient heat transfer at small viscous losses. Numerical modeling was already performed both for parallel-plate AMR [26, 51–54] and for packed sphere-bed AMR [55–58]. Main objectives consist in the prediction of the temperature span between hot and cold end of the AMR and its cooling capacity e.g. as a function of the time [53, 55, 58], the frequency of operation [27, 54, 56], the utilization [27, 54, 59] or the thermal losses [60]. Experimental approaches to determine the temperature span and cooling capacity in different MCM geometries are discussed in [61]. This rotating AMR provides a cooling power of 100 W for a temperature span of 20.5 K with sphere packed bed [62]. Geometrical aspects of the AMR have been studied in [51] to identify optimum lengths, sphere diameters or plate spacings for different operation frequencies and cooling loads, or in [63] to understand how a non-uniform plate spacing affects the heat transfer.

The foregoing literatures worked out that optimum values for mass-flow rate and operating frequency exist for a particular AMR which are in turn functions of heat-transfer coefficient in the AMR. This optimum depends on the delicate coupling between geometry offered to the fluid flow, the viscous losses, the timing of mag-/demagnetization and the resulting formation of the thermal boundary layers. At present these issues are not fully resolved. Only a very few number of works provide space-resolved temperature data inside the AMR, (e.g. see [26, 58, 64]) while the majority of the works is focused onto global quantities such as the temperature span between hot and cold end of the AMR.

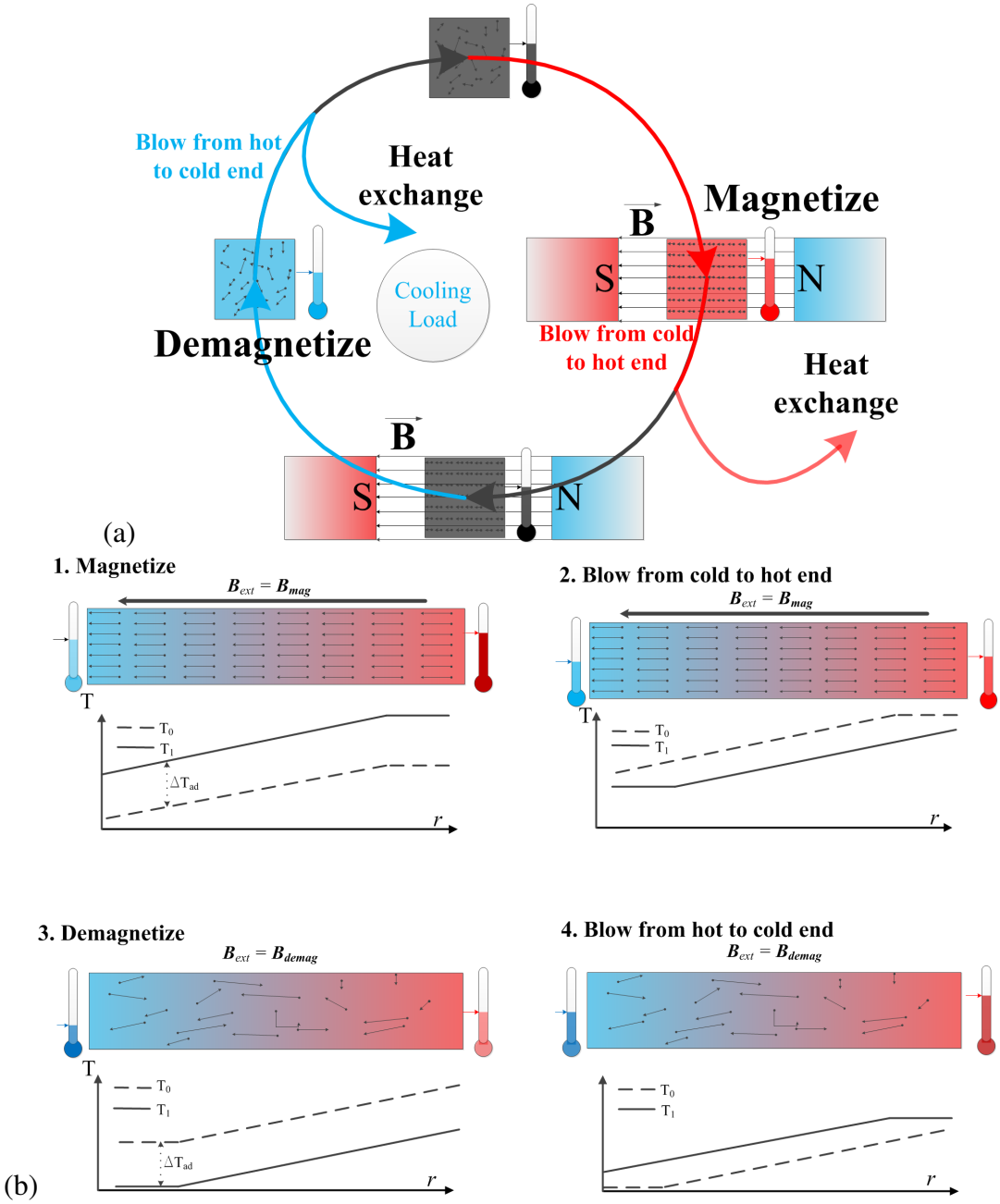

Fig. 1.1 (a) Thermodynamic cycle of a small fraction of an MCM in AMR and (b) the schematic illustration of an AMR with a established temperature span along hot and cold end. The dashed and solid line in each step denoted in (b) represent the temperature of the local MCM along two ends before and after the referred process is taken place, respectively.

Thus it make sense to study the dynamics of the heat transfer in the simplest case, namely from a periodically magnetized and demagnetized plane gadolinium plate into the stagnant heat transfer fluid, first without any natural or forced convection. By means of a Mach-Zehnder interferometer this dissertation is able to provide for the first time the space- and time-resolved temperature field inside the heat transfer fluid during the magnetization and the demagnetization phases. This work was published in Ref. [65] and is presented in Sec. 3.1.

Comparing the current efficiency of magnetic cooling with conventional refrigeration [66], room-temperature MC is still far from being competitive. This is partly due to the fact that the efficiency of active regeneration is strongly coupled to the efficiency of the convective heat transfer in the regenerator. Hence, optimizing the performance of the AMR is of primary importance. Despite the efforts mentioned, insufficient heat transfer is currently one major bottleneck of the AMR. This is in particular true at the desired high power density to achieve compact and economic MC devices, because the fluid flow through the active regenerator is oscillatory.

Therefore, the works presented in Sec. 3.2 reports a new heat transfer enhancement method by means of magnetohydrodynamic (MHD) convection. This type of convection is driven by the action of the Lorentz force density, $\vec{f}_L = \vec{j} \times \vec{B}$, generated by the interaction between an electric current density $\vec{j}$ and a magnetic flux density $\vec{B}$. The realization of this idea during MC is relatively cheap, especially during the magnetization phase, as the electric energy required is small and the magnetic field is already available. MHD flows have already been studied intensively in the context of magnetoelectrochemistry e.g. [67, 68]. They can be used to significantly enhance the mass transfer in electrolytic cells which, for example, speeds up the rate of electrodeposition and its quality [69]. The objective of the present work is to transfer this concept to MC. For this purpose we applied an experimental setup sufficiently simplified with respect to the magnetic field and current injection such that it is still possible to measure both the velocity and temperature field. By means of particle image velocimetry and Mach-Zehnder interferometery we are able to deliver for the first time a proof-of-principle for heat transfer enhancement in MC by MHD flows. This part of work was published in Ref. [70] and is presented in Sec. 3.2.

Multiple aspects for the engineering optimization of regenerator bed are carried out, i.e. flow field coupled with heat exchange in regenerator and design of more energy intensive magnet assembly. Besides, works in finding alternative heat transfer fluids to replace air or water as commonly used in AMR, are also conveyed. Nanofluids, i.e. suspensions of 1-100 nm Al_2O_3, are estimated to be superior than water in heat transfer by an increase in heat transfer 15% by means of simulation [71]. The work presented in Chapter 3.3, published in Ref. [72], tries to introduce a new type of heat transfer fluid, consisting in GaInSn[73–75]

representing an eutectic metal alloy which is liquid at room temperature. According to private conversation, Prof. Andrej Kitanovski from University of Ljubljana also have tested the operation behavior of a room temperature liquid metal in a simplified AMR device. Due to the low Pr number the thermal diffusion layer is not constrained in the flow boundary layer. In fact, fluid flow in current prototypes are usually in laminar flow regime. Hence, heat transfer could be captured already with a simplified model. The high thermal diffusivity is needed to guide rapidly energy out of the MCM via flow boundary layer. This then is convected along flow direction to the selected end of the machine. The advantage of GaInSn is not humbled because it has a moderate viscosity, comparable to that of water. Therefore, it is an interesting candidate as replacement heat transfer fluid pending to be evaluated more into details.

1.2 REE separation and recycling technologies

1.2.1 Conventional separation methods

Besides the research in the application side of REE, this dissertation places also intensive attention on the harvesting and recycling of raw material which still is both economically and environmentally expansive. Due to the similar physical and chemical properties of REE, separating them out from each other is still a challenging and expensive task. After crushing and milling, ore silt undergoes flotation [76] and separation processes to get the REE oxides. It is followed by a hydrometallurgical process to recover rare earth metals or compounds [77].

Separating individual REE from mixtures essentially depend on their small differences in basicity. This determines the solubility of salts, hydrolysis of ions and formation of complex compounds. This is the working principle of separation technologies like fractional crystallization, fractional precipitation, ion exchange and solvent extraction.

Cerium (Ce), the most abundant REE, could be separated easily. Heating REE ores in air to 650 °C or drying RE hydroxides in air at 120-130 °C, Ce(III) is selectively oxidized to Ce(IV) and removed from mixtures by selective dissolution with dilute acid or dissolution in higher concentrated acid followed by a selective precipitation [78]. Samarium (Sm), europium (Eu), Ytterbium (Yb), when concentrated after processed by other procedures, could be separated by selectively reducing them from trivalent mixtures to divalent state. Shastri et al. [79] report a work to upgrade Eu_2O_3 with 99.9 % purity from mixtures of REE with photochemical reduction and precipitation of divalent Eu(II). Fractional crystallization is used for light rare earth, i.e. lanthanum side of REE, beneficiation and separation due to the

decreasing contrast of solubility increase with uprising atomic number. This is a procedure of a slow extraction of salt from dissolved state to solid state, precipitation, due to a change in its solubility in varying temperature or water evaporations. This method is regarded as best conventional method to extract REE into highly purified individual elements[80]. Fractional precipitation is realized by forming less soluble rare earth compound by adding chemical reagents. This method is generally used to split REE mixtures in solution to different groups according to solubility of its sulfate compound. Consequently, extraction is done separately for different groups later. However, these methods are far from efficient and mostly time-consuming and labor intensive. Thus, after 1950s, ion exchange and solvent extraction have dominated the market. For a high purity extraction, ion exchange is used while for massive production solvent extraction [81] is more economic. However, these two methods suffer from high demanding in time consumption and require large amount of non-recyclable chemicals [82].

A separation factor, according to distribution law is used to evaluate the degree of separating species A from B in a mixed system. For that purpose, one considers a system of two immiscible liquid phase system, 1 and 2 under equilibrium conditions. Using the content ratio of species A and B in the different phases, given by are $D_A = \frac{C_{A1}}{C_{A2}}$ and $D_B = \frac{C_{B1}}{C_{B2}}$, respectively, the a separation factor is readily obtained

$$\alpha_B^A = \frac{D_A}{D_B}. \tag{1.10}$$

A good separation of A and B is achieved by either $\alpha >> 1$ or $<< 1$.

Ion exchanger contains salt in which a portion of ions are attached to an insoluble organic phase [83]. By forcing a direct contact between this exchanger and RE solution, ions in the exchanger are displaced by that in the solution. By applying complexing agents, ion exchange achieves enhanced separation factor and by forming citrate complexes with different stabilities of individual RE in a mixture. This is followed by eluting exchanger to extract separated RE compounds. Solvent extraction on the other hand, replaces the resin exchanger to organic phase to which a diffusion of REE from aqueous phase is allowed. The rare earth loading in solvent/extractant could be very high O(0.3 M) which result in a more compact device to function [84].

The above methods are used sometimes in conjunction with each other in the processing and purification of the REE. Magnetic separation, which is the work of this dissertation, tries to bring one more optional technology to the pool of already existing methods. The advantage of magnetic separation, as will be clear soon, is that it is simple in setup and green in its method. However, the first important step is to understand its working principle.

1.2.2 Magnetic separation of REE

The magnetic field gradient force, provided by an inhomogeneous magnetic field

$$\vec{f_m} = \frac{\chi_{mol}}{\mu_0}(\vec{B}\cdot\nabla)\vec{B} = \frac{\chi_{mol}}{2\mu_0}\nabla B^2 \tag{1.11}$$

is a versatile tool to separate ferro- and superparamagnetic components. It is a function of a magnetic susceptibilty χ based on the unfilled $4f$-orbits and μ_0 refers to the permeability of free space.

This means, a volume force is formed when a material is exposed to an external magnetic field with a spatial gradient. This force interacts with the material, and its direction is not correlated with magnetic flux density vector direction. The magnitude of this force is influenced by the magnetic susceptibility χ of the substance, i.e. a non-dimensional number indicating its degree of corresponding magnetization in an external magnetic field. When $\chi > 0$, such material is paramagnetic above its Curie temperature where all 17 rare earth elements are classified into. Material is diamagnetic if $\chi < 0$. Example of the static levitation of diamagnetic material is presented in [85]. Small diamagnetic susceptibility material such as water, $\chi \approx -9 \times 10^{-6}$, could also be levitated and an example of it is presented with flying frog in high magnetic field 16 T [86].

$\vec{f_m}$ has been commercially utilized for a long time in sorting scrap metal or in mineral processing to separate iron-bearing or paramagnetic ore particles [87]. The separable particle sizes extend over a wide range, starting from 10^{-2} m until about several 10^{-6} m, achieved in modern high-field-gradient magnetic separators (HGMS) [88]. Acting on a comparable particle size, $\vec{f_m}$ is now also extensively used in bioengineering to capture biological material by means of functionalized magnetic microparticles in HGMS [89–91].

The question of how to separate or manipulate even smaller objects, namely paramagnetic ions, by means of $\vec{f_m}$ has driven numerous research activities over the past two decades. In particular, $\vec{f_m}$ has been successfully applied in magnetoelectrochemistry, see recent review articles [92, 93] together with Ref. [94] which explains the basics of the $\vec{f_m}$-driven mass transport in the electrolyte in the vicinity of small high-power NdFeB magnets. If the paramagnetic ions are the electroactive species in the electrochemical system, the electric current inside the electrolyte causes a concentration gradient of the paramagnetic ions at the cathode. As a result, the curl of $\vec{f_m}$, i.e. $\nabla \times \vec{f_m}$, becomes different from zero and a small-scale convective flow appears [95]. This flow enhances mass transport, as shown recently at magnetic nanoparticle electrodes [96], or assists the patterning of metallic deposits [92, 93, 97, 98].

However, even without an electric current, paramagnetic ions in an aqueous solution are reported to behave remarkably in the presence of $\vec{f}_m$ [99–107]. Refs. [100] describes a confinement of the paramagnetic ions, produced by etching of a magnetized steel ball in an acid solution in areas of high magnetic flux density. While the shape of these zones could be explained qualitatively by the balance between hydrostatic and osmotic pressure, the large quantitative differences lead to the conclusion that $\vec{f}_m$ is too weak for the observed trapping of paramagnetic ions. In contrast to Ref. [100], previous works done by my colleagues did not contain a local source of paramagnetic ions but started with an initially homogeneous aqueous solution of either a transition metal ion, Mn(II) [99, 101], or a rare earth ion, Dy(III) [102]. In both cases, an enrichment of these ions up to 2 % of the bulk concentration was found in the high field gradient zone of permanent magnets placed on top of the solution. A comparable enrichment of about 2% was measured by another group in Ref. [106] in a $HoCl_3$ solution, where a permanent magnet was applied at the bottom of the container. In Ref. [107] the magnetomigration of paramagnetic (Dy^{3+}, Gd^{3+}) and diamagnetic (Y^{3+}) rare earth ions was studied in a gel. A continuous concentration increase up to 10% at 5 T was found for paramagnetic ions in the region of higher field gradient force, while a decrease was measured for diamagnetic Y^{3+} ions.

Generally, the possibility to separate the rare earth ions magnetically, instead of via liquid-liquid extraction, within the hydrometallurgical step integrated into the beneficiation of the rare earth from the raw ore or from industrial process residues [82, 108], would be very economically and environmentally beneficial. Indeed, the chemical similarity of the rare earth forces a large number of time-consuming extraction steps to be taken, which require a large amount of non-recyclable chemicals [82] as already outlined in the foregoing section. This could be reduced if the differences in the magnetic moments of the rare earth ions could be exploited efficiently.

However, the application of such a magnetic separation step is still hampered by the insufficient understanding of the above-mentioned observations. The underlying mechanism is physically unclear. This was mentioned briefly in a work of my colleagues, Ref. [99], with reference to the huge difference in the order of magnitude between the kinetic energy of 3/2 kT at a temperature T, associated with Brownian motion (k - Boltzmann constant), and the magnetic energy, proportional to the magnetic moment of the molecule times B. Hence, it actually seems unlikely that $\vec{f}_m$ has a direct influence on the paramagnetic ions.

To resolve this paradox, the concept of the effective magnetic susceptibility of nano- and micro-scale clusters of paramagnetic ions, called *magnions* was introduced in Refs. [104, 109] Magnions represent a charged region of continuous medium in a liquid containing a large number of paramagnetic ions. If the theory of magnions can be substantiated, their much

larger effective magnetic susceptibility compared to that of the single ions could indeed help to explain the above-mentioned findings.

The working hypothesis here is different. This dissertation postulates that a hidden trigger process is involved in Refs. [99, 101, 102, 106]. For the latter, solvent evaporation is the most likely candidate. Thus, the transport process of enriched paramagnetic clusters displays in a form of reduced mixing by suppressing convection through paramagnetic levitation. A similar work, but in different context, was reported with a soft magnet iron wire and external magnetic field on a dyed paramagnetic solution [110] and for liquid-liquid phase separation due to a difference in susceptibility between the two phases [109]. To verify the hypothesis of an evaporation-assisted magnetic separation, a combined experimental and numerical approach is conducted. This is followed by a stability analysis in the solution for a better understanding of transport process in the aqueous phase. This part of work has been published in Ref. [111] and is presented in Chapter 4.

1.3 Body forces in magnetohydrodynamics and ferrohydrodynamics

The two body forces, manipulating transport process relevant in this dissertation, are introduced in this section. These are the Lorentz force and Kelvin force which fall into the scope of magnetohydrodynamics (MHD) and ferrohydrodynamics (FHD), respectively. They are essentially formed in the presence of a magnetic field and /or electric field inside the fluid phase. Consequently, they enter Navier-Stokes equation as extra body force terms and alter the velocity field. The resulting velocity field then enters the transport equation and changes temperature and concentration transport process.

To generate magnetohydrodynamic (MHD) convection, both magnetic field and electric field has to be present. In a weakly electrically conducting fluid, an external electric potential must be applied via electrodes for a resulting Lorentz force of sufficient magnitude to have an impact on flow field. For high conducting medium on the other hand, an induced electric current could already interact with the applied magnetic field and influence the fluid motion. Therefore, a short introduction into magnetohydrodynamics, as relevant for the work in Chapter 3 is given first.

In Chapter 4, Kelvin force plays a vital role in manipulating mass transport of a locally enriched rare earth salt solution. This is realized by suppressing the onset of instability/ convection in the presence of such body force. Therefore, a brief account is given on ferrohydrodynamics which constitutes the second part of this section. Despite that rare earth

salt solution is only slightly paramagnetic, the name ferrohydrodynamics, used since the pioneering works of Rosensweig [112] on the fluid dynamics of superparamagnetic ferrofluid in the presence of a magnetic field, is also adopted here.

1.3.1 Magnetohydrodynamics (MHD) in low and high conducting media

For fluid which are conducting, an external body force, namely Lorentz force, can influence its motion. The Lorentz force density is the cross product of electric current j and magnetic field B

$$\vec{f_L} = \vec{j} \times \vec{B} \tag{1.12}$$

The magnetic field, as is explained earlier, is provided by permanent magnets. The electric field on the other hand is injected by different means. One method is by applying electrodes which force a gradient in electric potential within the fluid. This method is used in a low electric conducting liquid, e.g. 0.5 M NaOH in Sec. 3.2. Alternatively, electric field can also be generated by a locally alternating magnetic field or by relative motion of a conducting medium inside magnetic field. Thus, in high electrically conducting fluid, this induced electric current could in principle already have an effective influence on the medium. The induced electric field and current density are governed by Faraday equation Eq. (1.13) and Ohm's law (1.14), respectively.

$$\nabla \times \vec{E} = -\frac{\partial \vec{B}}{\partial t} \tag{1.13}$$

$$\vec{j} = \sigma(\vec{E} + \vec{u} \times \vec{B}) \tag{1.14}$$

Two dimensionless parameters are used to evaluate the significance of magnetic field on the fluid motion by means of the Lorentz force. The Hartmann number is defined as

$$Ha = Bl_c\sqrt{\frac{\sigma}{\rho\nu}} \tag{1.15}$$

where B is the magnetic flux density, l_c is the characteristic length, σ is the electric conductivity, ρ is the density, ν is the kinetic viscosity of the fluid, respectively. It represents the ratio between the Lorentz force and viscous force. The second number is the interaction parameter

$$N = \frac{Ha^2}{Re}. \tag{1.16}$$

It shows the ratio between the Lorentz force to inertia. Generally, for low conducting fluid like a salt solution, an external electric potential needs to be applied for an effective electric current to set in. For high conducting fluid like liquid metal, $\sigma = 3.1 * 10^6$ S/m [73], the electromotive force (EMF) term in Ohm's law give rise to electric dipole. When the EMF distribution is not homogeneous, e.g. an internal flow exposed in a perpendicularly superposed homogeneous magnetic field. The current would close at the momentum boundary, given non-conducting or finite conducting wall, where no-slip boundary condition must be respected. The obtained Lorentz force points anti-parallel to the flow direction in the middle part of the flow profile and parallel vector at wall. Therefore, an extra pressure loss gives a planer velocity profile and the significance of Lorentz force acting on the flow is determined by a Ha number. Given Ampere's law,

$$\nabla \times \vec{B} = -\mu \vec{J} \tag{1.17}$$

an induced magnetic field is produced theoretically. To evaluate the significance of this induced magnetic field, a dimensionless magnetic Reynold number, $R_m = \frac{ul_c}{\lambda_m}$ is used where $\lambda_m = \frac{1}{\mu_0 \sigma_0}$ is the magnetic diffusivity. This parameter defines the ratio between the advection and diffusion of magnetic field. For materials and working conditions which are relevant in this dissertation, the resulting R_m is always much smaller than one. This means they have a rather high magnetic diffusivity or slow motion and characteristic length. $Pr_m = \frac{\nu}{\lambda_m} << 1$, the magnetic Prandtl number, holds for all cases. It represents the ratio between momentum diffusivity to magnetic diffusivity. Consequently, a quasi static approximation is fulfilled. This means the magnetic field is considered as constant because the induced field by the electric current can be neglected [113].

1.3.2 Ferrohydrodynamics (FHD) in paramagnetic rare earth salt solution

Magnetic material means those that have a certain magnetization given an applied external field. According to degree and type of magnetization, they are classified as diamagnetic, paramagnetic, ferromagnetic, antiferromagnetic and ferrimagnetic [114]. Ferromagnetic materials, such as iron, cobalt and nickel, are those with an irreversible nonlinear response of magnetization M and a maximum saturation magnetization M_s when subjected to an imposed magnetic field at a given temperature. This is shown in the hysteresis loop where a remanent magnetization remains after the external magnetic field is removed.

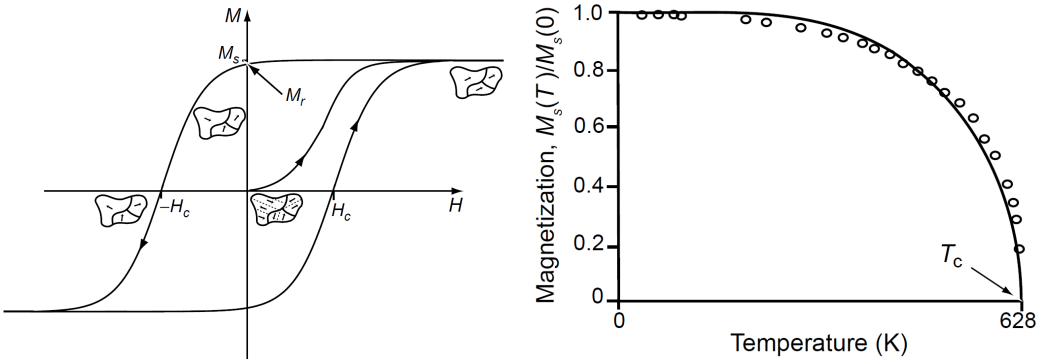

Fig. 1.2 (a)The hysteresis loop of a ferromagnet. Start from an unmagnetized state be magnetizated via an imposed magnetic field H to a saturated state M_s. Remanence and coercivity are M_r and H_c respectively; (b) Magnetization as function of temperature of Nickel with Curie temperature of $T_c = 628$ K. [114]

However, the magnetization of material decreases with an increase in its temperature. Saturation magnetization becomes zero when the Curie temperature is reached, e.g. $T_c = 628$ K for nickel in Fig. 1.2b. Above the Curie temperature, the ferromagnetic order collapse and the material becomes paramagnetic. Gadolinium, for example, has a Curie temperature of ca. 294 K[36] near room temperature. $\frac{\partial M}{\partial T}$ reaches its maximum at the Curie temperature. This explains in one way, recall Eq. 1.3 and 1.5, why a maximum magnetocaloric effect based on second order phase transition happens near its Curie temperature. Despite M_s is zero, some alignment of the magnetic moments appears when the material is subjected to an external magnetic field. This leads to a weak magnetization. The ratio of magnetization and applied magnetic field is defined as

$$\chi = \frac{\partial M}{\partial H}. \tag{1.18}$$

Except for large applied field or temperature close to the Curie temperature, the susceptibility χ is constant. As is mentioned in Sec. 1.1.1, when the material has a high enough magnetization, for example NdFeB permanent magnet or MCM, a demagnetization field H_d is formed which decrease the internal field inside the magnetic material. But this is irrelevant for a paramagnetic salt solution. When the applied magnetic field is inhomogeneous, a magnetic energy field is formed inside the fluid media which tunes Gibbs free energy $G = u + pv - Ts - \mu\vec{H_{ext}}$. Hence, a body force is formed which direction is anti-parallel to the gradient of corresponding magnetic energy field. The magnetic field gradient force or Kelvin force for short is calculated via

$$\vec{f_m} = \nabla(\mu_0 \vec{H}_{ext} \cdot \vec{M}) = \mu_0(\vec{M} \cdot \nabla)\vec{H}_{ext} \tag{1.19}$$

When magnetization $\vec{M}$ depends on internal magnetic field, Eq. (1.19) is therefore

$$\vec{f_m} = \mu_0(\vec{M}\cdot\nabla)\vec{H} - \mu_0\nabla[\int_0^H(\frac{\partial M}{\rho\cdot\partial(1/\rho)})dH] \tag{1.20}$$

But for diluted paramagnetic salt solution, e.g. $DyCl_3$ dissolved in water solution, the second term could be ignored. Therefore, Eq. 1.20 is simplified to

$$\vec{f_m} = \frac{\chi_{mol}}{\mu_0}(\vec{B}\cdot\nabla)\vec{B} = \frac{\chi_{mol}}{2\mu_0}\nabla B^2 \tag{1.21}$$

Although, this force is weaker in paramagnetic fluid compared to superparamagnetic fluid like a ferrofluid, some attracting influence acting on the fluid is demonstrated in the literature [106, 107, 110]. A typical example is the enrichment of Dy(III) from from its aqueous bulk by means of a small permanent magnet[115]. This forms the basics of ferrohydrodynamics and hence makes a magnetic separation of rare earth salt solution with permanent magnet possible.

1.4 Chapter summary

This chapter introduces the definition of REE and its application in various high-tech clean technologies. Two important themes of research are addressed, namely magnetic cooling and magnetic separation of REE. Literatures on the two subjects are reviewed. The manipulation method of transport process is introduced with an emphasis on two body forces generated with superposed electric and/ or magnetic fields.

Chapter 2

Experimental and numerical techniques

The focus of this dissertation is to resolve the transport phenomenon in the liquid single phase by means of experimental studies. Numerics are conducted to support the design of the setup or as a necessary assistance for understanding the experiment results.

Therefore, first and main part of this chapter presents the experimental techniques used throughout this dissertation. Setups which are used in later chapters will be summarized at the beginning and details could be found in their designated sections. Special emphasis is paid on interferometer and its versatile variations designed and used as well as its corresponding data processing algorithms. Velocity measurement system with ultrasound doppler velocimetry (UDV) and particle image velocimetry (PIV) as well as conventional thermocouple temperature measurement are also covered briefly.

The remaining part is dedicated to the introduction of the governing equations essential for simulation. First, Mexwell's equations are discussed for the simulation of magnetism related physical field. Momentum and transport equations integrating Lorentz force and Kelvin force in the context of conventional MHD and FHD are presented later. Simulation of transport process is limited to diffusion cases. Corresponding discretization scheme is presented.

2.1 Experimental

For transparent media, particle image velocimetry and interferometry are used to map the 2D velocity distribution and 2D (quasi 3D) temperature and concentration field inside the fluid, respectively. In opaque media, however, such as a room temperature liquid metal GaInSn, c.f. Sec. 3.3, an ultrasound doppler velocimetry is used to measure 1D velocity component distribution along the propagation direction of the ultrasonic wave. A conventional thermocouple based temperature measurement system is used to map the

background temperature. This at the same time offers the reference ambient temperature for the calibration of the relative temperature to exact temperature obtained by interferometry. Efforts are made in providing an automatic measurement systems via labview, matlab and python to minimize the labor effort. The automation framework is illustrated in Fig. 2.1 followed by a more detailed description in the next sections.

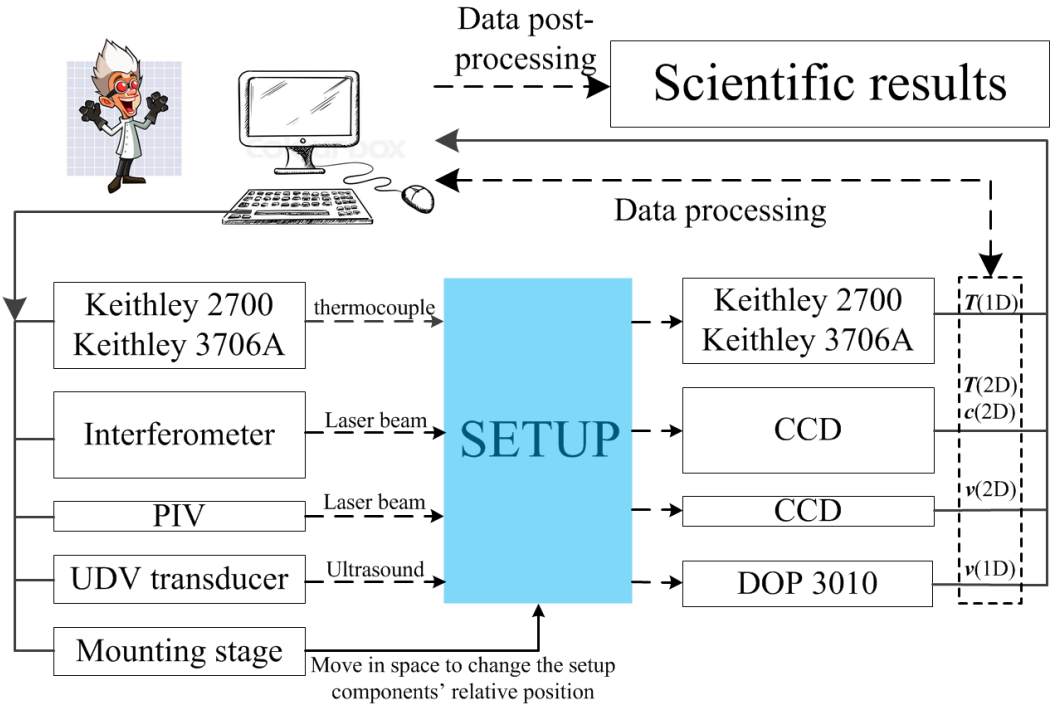

Fig. 2.1 Illustration of experiment systems and setups as designed and used in this dissertation.

Table 2.1 gives an overview about all important setups used along the dissertation. Details will be given in the corresponding sections. Table 2.2 collects, on the other hand, important material properties used throughout this dissertation.

2.1.1 Mach-Zehnder interferometer (MZI)

Light exhibits a combined character of wave and particle. Upon demonstrating certain phenomena such as diffraction and interference, it is convenient to regard it as an electromagnetic wave. This is true when photons are sampled in a time scale large enough that the observer only witness the accumulated result at a given space. Therefore, Fourier and ray optics related to interferometer are presented here.

Light can be regarded as a transverse electromagnetic wave propagating perpendicular to its oscillating plane. According to Maxwell's equations, a time varying local electric field

Table 2.1 Collection of all experimental setups designed and used in this dissertation

Setup Purpose and location	Basic Info			
	Fluid type	T method	c method	v method
MC Sec. 3.1	n-Decane	Int & TC	/	/
MC Sec. 3.2	0.5 M NaOH	Int	Int	PIV
MC Sec. 3.3	GaInSn	TC	/	UDV
MS Sec. 4.1	0.5, 1 M $DyCl_3$	Int	Int	/
Extension works:				
MC Sec. 5.2.1	0.5 M NaOH	Int & TC	Int	PIV
MS Sec. 5.2.2	0, 0.5, 1 M $DyCl_3$	Int	Int	PIV

* MC stands for magnetic cooling
* MS stands for magnetic separation
* Int stands for interferometer
* TC stands for thermocouple

Table 2.2 Collection of properties of solid & fluid as used throughout this dissertation

Substance info	Property info			
	Density	Heat capacity	thermal conductivity	dynamic viscosity
	ρ [kg/m^3]	C_p [kJ/kg·K]	λ [W/m·K]	μ [mPa · s]
Gd	7.895 $\times 10^3$	0.356	8	/
Quartz	2.2 $\times 10^3$	0.480	1.1	/
Plexiglass	/	/	0.2	/
n-decane	0.730 $\times 10^3$	2.210	0.12	/
water	1.000 $\times 10^3$	4.200	0.58	0.890 [116]
0.5 M NaOH	1.019 $\times 10^3$ [117]	4.023 [118]	/	0.9715 [117]
$DyCl_3$	parameters	are taken	from water	/
GaInSn	6.360 $\times 10^3$ [73]	0.366 [74]	23.9 [75]	1.90 [73]

Substance info	Property info		
	densification coefficient	electric conductivity	magnetic susceptibility
	α [m^3/ mol]	σ [S/ m]	χ [/]
Gd	/	7.63×10^5 [116]	/
water	/	/	-9×10^{-6}
0.5 M NaOH	/	9.3	/
$DyCl_3$	0.243×10^{-3} [102]	/	5.5 $\times 10^{-7}$ m^3/ mol [116]
GaInSn	/	3.1×10^6 [73]	/

will a generate magnetic field and a local change in magnetic field will result in an electric field. Since the two fields are correlated, it is usually sufficient to discuss electric field as a wave in space and time. Let us first consider a single fraction of wave from any source which the electric field varies along the direction of the unit vector $\vec{e_r}$ along a given plane, namely the x-y plane, and propagates along z direction. The electric field is then

$$\vec{E}(x,y,z,t) = \mathrm{a}\cdot\cos(2\pi(ft - z/\lambda))\cdot\vec{e_r} = \mathbb{R}\mathrm{e}\{\mathrm{a}\cdot e^{2\pi i(ft-z/\lambda)}\}\cdot\vec{e_r} = \mathbb{R}\mathrm{e}\{\mathrm{A}\cdot e^{2\pi ift}\}\cdot\vec{e_r} \quad (2.1)$$

where a is the amplitude; f is the frequency; λ is the wavelength of the light; A is the complex amplitude.

Now that when two fractions of waves overlap themselves in space, a resulting complex amplitude along $\vec{e_r}$ is

$$A = A_1 + A_2 = a_1\cdot e^{-2\pi iz_1/\lambda}\cdot\vec{e_{r1}}\cdot\vec{e_r} + a_2\cdot e^{-2\pi iz_2/\lambda}\cdot\vec{e_{r2}}\cdot\vec{e_r}. \quad (2.2)$$

The z coordinate of the two are adjusted to an universal one by introducing a phase $\phi = 2\pi z/\lambda$. With given the polarization direction $\vec{e_r}$ and amplitudes of the two considered to be the same, the equation is simplified by introducing the illumination intensity at given x-y plane of photon sampling

$$I(x,y,t) = \frac{c}{4\pi}\sqrt{\frac{\varepsilon}{\mu}}|\vec{E}(x,y,z,t)|^2 \quad (2.3)$$

of the light received at a certain plane to

$$I = |E|^2 = (E_1+E_2)^2 = I_1 + I_2 + 2(I_1I_2)^{0.5}\cos\Delta\phi \quad (2.4)$$

$\Delta\phi$ is the phase difference of the two wave trains. μ and ε are permeability and permittivity of the medium. Therefore, the highest and lowest illuminations are $I_1 + I_2 + 2(I_1I_2)^{0.5}$ and $I_1 + I_2 - 2(I_1I_2)^{0.5}$, respectively. When the same interference pattern for two beams in a continuous spatial range of light waves exist, it is said to be in spatially coherence length. Within coherence length(area), continuous interference pattern is obtained when a continuous change in the phase difference is offered by two beams.

In general, the rule of thumb for forming an interference pattern of a sufficient quality to be resolved in measurements are:

- Spatial coherence is large enough for a given measurement region.
- Time coherence is large enough for a given phase difference for both beams of optical path.

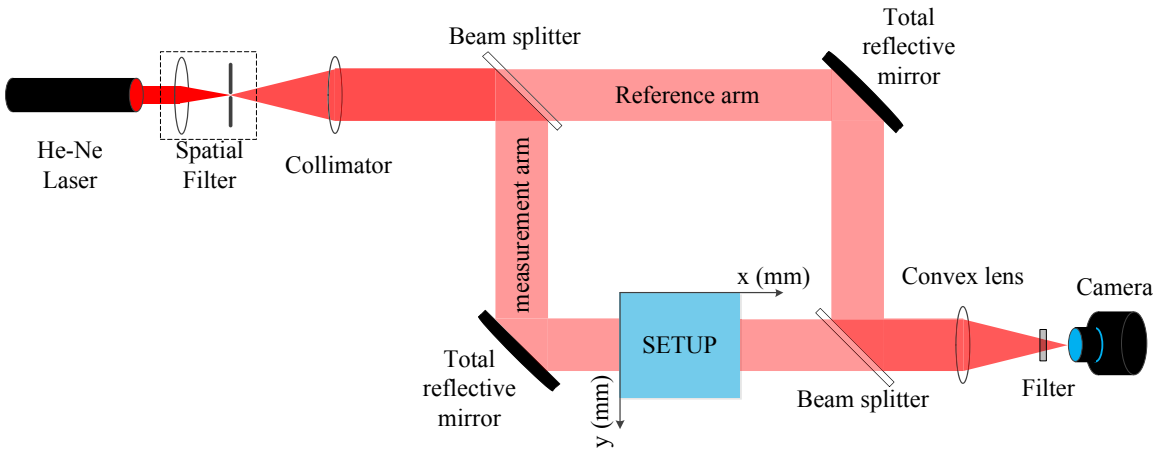

Fig. 2.2 A Mach-Zehnder interferometer system with beam direction parallel to x and a measurement plane y-z

- Both beams at the interference area, sampling area, must have the same polarization and wavelength.
- Energy level, amplitude of beam, should be the same to fulfill the maximum contrast of constructive interference and destructive interference illumination.

Setups and critical issues

The interferometer systems as used here in this dissertation is a Mach-Zehnder interferometry or variations of it. The Mach-Zehnder interferometer is an integrated system composed of a low noise He-Ne laser with high spatial and time coherence and is quasi longitudinal monochromatic with a wavelength $\lambda = 632.8$ nm. Spatial filter and collimator from Melles Griot are used to provide a spatial and temporal coherent light source with a homogeneous illumination. Beam splitters are used to split the wave amplitude to maintain the coherence of two beams. The sampling core is a high resolution camera and connected directly to a computer.

Following the preconditions discussed, there are several interferometers designed, built, calibrated and used in this dissertation. To name some, Mach-Zehnder interferometry, double Mach-Zehnder interferometry with up to 3 degrees of freedom in space are illustrated below.

To address the theories that are necessary for a data processing later, the elucidation start with a simple and classical Mach-Zehnder interferometer (MZI).

MZI has a broad application in transparent fluid media. This dissertation makes use of it in mapping time- and space- resolved temperature $T(\vec{r},t)$ and concentration $c(\vec{r},t)$ change by monitoring the refractive index $n(\vec{r},t)$ inside the fluid. $\vec{r} = r_1 \cdot \vec{e_{r_1}} + r_2 \cdot \vec{e_{r_2}} + r_3 \cdot \vec{e_{r_3}}$ is a random

vector in space and t refers to time. The interferograms were recorded with a frame rate of up to 30 Hz using a CCD camera (Dalsa DS-21-02M30). MZI is operated under finite fringe mode, in which the period λ_0 of the fringes, or their wave vector $\vec{k_0} = 2\pi/\lambda_0 \cdot \vec{e_k}$ where $\vec{e_k}$ is the unit wave vector, can be externally adjusted. The intensity $I(\vec{r})$ in the interferogram can be rewritten, see Eq. 2.4, as $I(\vec{r}) = I_0(\vec{r}) + I_a \cdot cos[\Delta\phi(\vec{r})]$ with $\Delta\phi(\vec{r}) = \vec{k_0} \cdot \vec{r} + \phi_0(\vec{r}) + \varphi(\vec{r})$. I_0 and I_a denote the slowly varying inhomogeneities of the illumination and the amplitude of the fringe contrast, respectively. Without optical inhomogeneity, i.e. in the isothermal heat transfer fluid, the optical phase $\Delta\phi(\vec{r})$ is equal to $\Delta\phi(\vec{r}) = \vec{k_0} \cdot \vec{r} + \phi_0(\vec{r})$, where $\phi_0(\vec{r})$ contains the optical aberrations of the system. In the absence of vibrations, $\phi_0(\vec{r})$ is the same in every interferogram recorded. Though an optical table is used, there is still a low level of vibrations, e.g. arising from the motorized translation stage for mounting permanent magnets and human walking nearby. These vibrations lead to a random noise described in $\phi_0(\vec{r},t)$. To get rid of this noise, multiple methods are developed facing different situations. They will be introduced later in detail at data post processing phase in later part of this section.

When there's a change in the properties of interest, namely T and c inside the setup, a change in optical phase difference

$$\Delta_t\phi(\vec{r}) = \Delta\phi(\vec{r})_{t+\Delta t} - \Delta\phi(\vec{r})_t \tag{2.5}$$

is formed due to a change in the refractive index. This is visible in the interferogram as a bending of the interference fringes, e.g. in the left part of Fig. 2.3b.

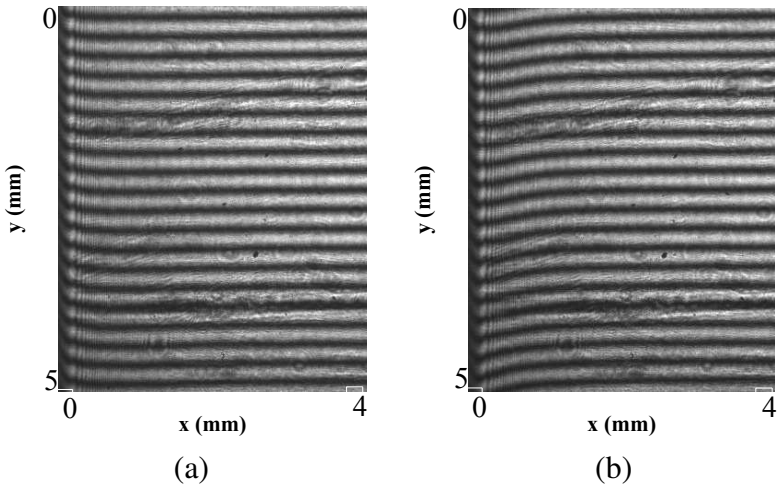

Fig. 2.3 The interferograms at 0 s (a) and after 4 s of magnetization (b). The Gd plate is located at the left margin of (a) and (b), cf. Sec. 3.1.

The MZI maps the phase difference $\Delta_t\varphi(\vec{r})$ between the cell under study and reference beam, which relates to the difference in the refractive index Δn_m as follows:

$$\Delta n = \frac{\Delta_t\varphi(\vec{r})\cdot\lambda}{2\pi l_c} \tag{2.6}$$

where $\lambda = 632.8$ nm is the wavelength of the He-Ne laser. l_c is the characteristic length of the beam which is its path through the optical cell and $\Delta_t\varphi(\vec{r})$ a phase difference spatial distribution compared in time line. The temperature and concentration change, $\Delta T(\vec{r'},t)$ and $\Delta c(\vec{r'},t)$ where $\vec{r'} = r_1\cdot\vec{e_{r_1}} + r_2\cdot\vec{e_{r_2}}$ is the vector in the measurement plane, is calculated from the refractive index change Δn_m and the known coefficient $\partial n/\partial T$ and $\partial n/\partial c$ according to $\Delta n_m(\vec{r},t) = n(T,c,\vec{r'},t) - n(T_0,c_0,\vec{r'},t_0)$. Since $\partial c/\partial n$ and $\partial T/\partial n$ are constant, a simplified calculation is obtained

$$\Delta T = \int_{T_0}^{T} dT(\vec{r'},t) = \int_{n_0}^{n} \partial T/\partial n\cdot d(n_m(\vec{r},t)) = \partial T/\partial n\cdot\Delta n_m \tag{2.7}$$

$$\Delta c = \int_{c_0}^{c} dc(\vec{r'},t) = \int_{n_0}^{n} \partial c/\partial n\cdot d(n_m(\vec{r},t)) = \partial c/\partial n\cdot\Delta n_m \tag{2.8}$$

Resolution of the Mach-Zehnder interferometer

To the best of my knowledge, a discussion of the resolution and accuracy of a Mach-Zehnder interferometer does not exist in all related textbooks and publications. This is partially due to its high complexity which makes it impossible in most cases.

However, there is a way to estimate spatial and temporal resolution when considering the resolution limit from its major source, i.e. a discretization in CCD. The CCD samples the continuously changing interferogram in a data format called bit map in greyscale. For a typical 8-bit greyscale map, there's a greyscale depth of $2^8 = 256$. Hence the minimum phase shift in space to be identified has to be bigger than the phase that each unit of greyscale represents

$$\Delta\phi_{min} = \frac{\pi}{256} \tag{2.9}$$

Therefore, the resolution limit is calculated by converting this minimum phase shift value to temperature resolution. n-Decane, for example, has a refractive index change as function of temperature of $\frac{\partial n}{\partial T} = \frac{1}{2230}\ \mathrm{T}^{-1}$, cf. Sec. 3.1.1. This results in a temperature resolution limit of $\frac{\Delta\phi_{min}\cdot\lambda}{2\pi l_c}\cdot\frac{\partial T}{\partial n} = 0.28$ mK. This is relevant for very fine discretized sampling, i.e. when half wavelength sampling points are more than 256. But the actual functioning sampling greyscale depth is diminished by background illumination or inequivalent illumination of the two beams, cf. Eq. 2.4. This is further influenced by a coarse sampling of the fringe, e.g.

Fig. 2.3. This results in a larger identifiable phase shift in the actual situation. Each of the pixel, in Fig. 2.3, represent a phase range of $\Delta\phi_{pixel} = \frac{N_{\lambda_r} * 2\pi}{N_{pixel}}$ where $N_{\lambda_r} = 20$ is the fringe number in the sampling area and $N_{pixel} = 400$ the pixel number along y directions inside the sampling area. This result in a temperature resolution of ≈ 7 mK.

To correctly extract the temperature and concentration from the measured refractive index, or even decouple them, several dedicated data processing algorithms are developed. They will be presented in data post-processing. More discussions with respect to the proper selection of measuring mode and methodology on evaluating the measurement accuracies of interferogram will be analyzed and summarized in a work in progress Ref. [119].

Versatile variations on interferometer

Upon clarifying the working principle of a classical Mach-Zehnder interferometer, some modifications are made offering an even more versatile measurement approach. Fig. 2.4 shows a compact double interferometer built with a single beam source measuring two setups at the same time. This system has been tested on the 29th Deutsche Luft und Raumfahrt (DLR) parabolic campaign on board of a A310 plane in Bordeaux in September 2016 with a total amount of 124 parabolas. It exhibit a very robust design in terms of hardware and a compact optimization of measurement arms in a limited space. Nevertheless, such sensitive measurement system without a vibration compensation has an unstable behavior on board. The pin hole and the convex lens in the spatial filter, see Fig. 2.4, are precisely correlated. Therefore, any vibration and any change of gravity influence the quality of the obtained interferogram to a great extent. Preliminary know-how and details from this attempt will be presented in later chapters.

Furthermore, a design which is based on the idea of a double interferometer but offering a measurement plane x-y as well is designed and built up, see Fig. 2.5. The green and blue planes are parallel to x-y and y-z, respectively. Such design has an advantage that two setups are measured simultaneously covering all three spatial dimensions. Although with a slight modification, a 3D interferometer could be easily built by correlating the measurement beam in a single setup but along non-parallel planes. But it is not convenient for current setups as will be presented in this dissertation to be directly measured with such arrangement.

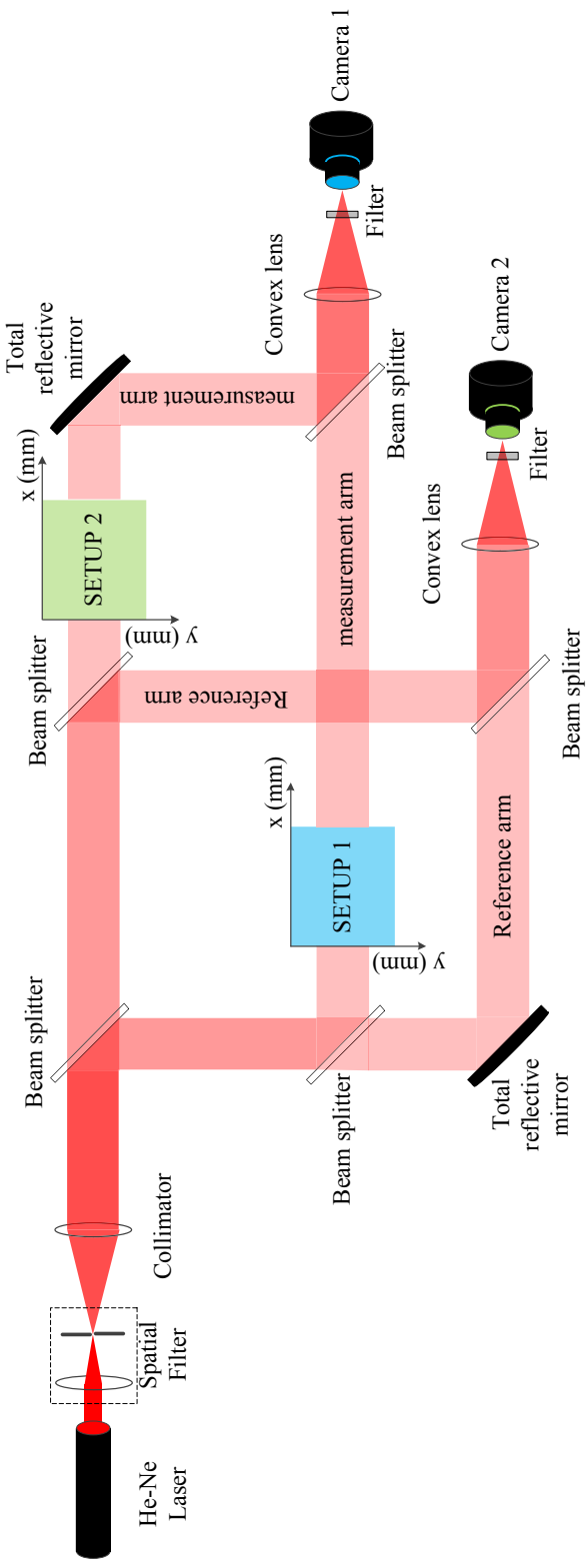

Fig. 2.4 A double Mach-Zehnder interferometer system with beam direction parallel to x-y plane and a measurement plane including z component for both setups. A zero point for both setups is determined.

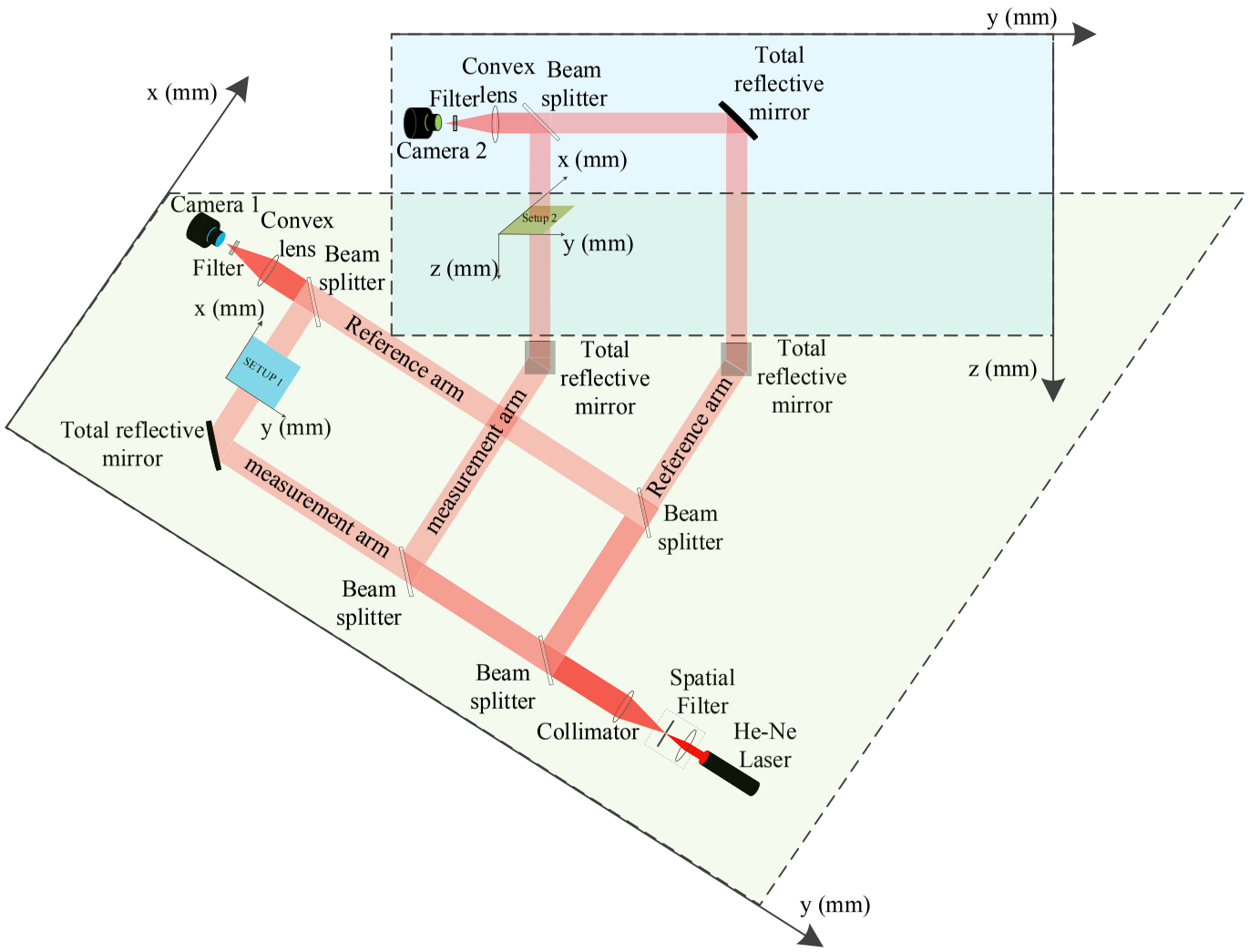

Fig. 2.5 A 3D double Mach-Zehnder interferometer system with beam direction (1) parallel to x-y plane and a measurement plane including z component for setup 1 and (2) beam direction parallel to z direction and a measurement plane x-y for setup 2. A zero point for both setups are determined respectively.

Data processing algorithm

After obtaining interferograms of sufficient contrast and quality, a data processing needs to take place. There's generally a maturely developed algorithm for extracting the refractive index out of the interferogram [65, 70]. For convenience, the structure of the algorithm developed and done in this work with respect to interferogram processing is named in a logical order. A pre-processing stage means all the raw data are allocated to a universal time and physical spatial coordinate, instead of pixel coordinate. They are at the mean time segregated and transformed into a sequence of identifiable information and been loaded. To some extent, a filtering step needs to be considered to improve the quality of the data. Due to the low noise to signal ratio of raw data, they are skipped but used to a very conservative extent for some special cases during post-processing phase.

The main processing algorithm is dedicated to bridge the way between an obtained refractive index and the preprocessed raw data, cf. Eq. 2.6. The interferogram processing to obtain the unknown $\Delta\varphi(\vec{r})$ was based on a complex Morlet wavelet transformation described in [120] and [65, 70] given by

$$\Psi(r_1) = e^{i\omega_0 r_1} \cdot e^{-\left(\frac{r_1}{\tau}\right)^2} \tag{2.10}$$

where $\omega_0 = 2\pi F_c$ with a control peak frequency $F_c = 1.5$ Hz and r_1 is the scaler with unit vector$\vec{e_{r1}}$ direction perpendicular to the fringe direction. The control width of the wave, τ, was set to $\tau = 1$. The daughter wavelet is obtained by

$$\Psi_{a,b}(r1) = \frac{1}{a}\Psi\left(\frac{r1-b}{a}\right) \tag{2.11}$$

where $a_j = 2^{-\frac{j}{N_v}}$ is the scaling factor and j is the scaling parameter. The choice of these parameters has to be tested each time but for us it works good when set to at 25 to 50 or 16 to 42 with a steps of 1, as well as a number of voices per octave N_v set at 12. The parameter b is determined by the discretized sample points of the interferogram in the signal direction, i.e. integer from 1 to the length of the signal in steps of 1. Through this, the wrapped phase $\phi_{wrapped}$ is extracted in a range in $[-\pi, \pi)$. Processing was followed by Goldstein's branch cut algorithm described by [121] to unwrap the extracted fringe phase $\phi_{unwrapped}$ which finally enters into Eq. (2.6).

Before stepping into next chapter, it is important to note again that the time and space domain resolution of refractive index field is determined by sampling frequency and the number of pixels of the CCD, respectively. The following data post-processing deals with the refractive index field $n(\vec{r},t)$ that is computed from this section.

Data post-processing algorithm

According to Eq. 2.6, the main data processing is to obtain the parameter $\Delta_t \phi(\vec{r})$. In the absence of vibrations, $\phi_0(\vec{r})$ is the same in every interferogram recorded. Though an optical table is used, there is still a low degree of vibrations, e.g. arising from the motorized translation stage for mounting. These vibrations lead to a shift in $\phi_0(\vec{r},t)$ over time. Recalling Eq. 2.5, such vibration lead to a sampling error of the real inteferogram which is delivered from and included in the main processing results. Therefore, the whole post-processing algorithm is dedicated to a correction of refractive index to its true value. To do this, its physical meaning plays a big role and some of the previous essential parameters has to be rediscussed here.

The refractive index obtained from the data processing algorithm is not without noise. The noise can be classified as

- Space domain transient random noise occurs in the refractive index maps due to the discretized sampling of the spatial optical path difference, $\varphi(\vec{r})$. To suppress this type of noise, preserving the magnitude of the signal, Gaussian low pass filtering is sufficient. A 2D N $\times$ N discretized filter window, $G(\vec{r'}) = \frac{1}{2\pi\sigma^2} e^{-\frac{(r_1-\mu_{r_1})^2+(r_2-\mu_{r_1})^2}{2\sigma^2}}$ could be used. A parameter must be verified for each cases, and an explicit denotation will be given later when the result is presented after filtering.

- Due to the vibration with small magnitude, the refractive index obtained has an overall vibrating phase shift overlapping the real refractive index. It a sort of random noise, there are multiple ways to eliminate such noise, e.g. 1.) time frequency domain filtering with a low pass filter, 2.) a correct sampling of a certain region or point to compensate the vibration at each time layer, or 3.) a fitting of a certain point along a certain time span with small system error to eliminate the random error. All three approaches are used in this dissertation and they will be explicitly denoted in each case later.

- Peak noise is the result of a large shift in $\phi_0(\vec{r})$ which emerges in the signal $\varphi(\vec{r})$. Usually, it is encountered in a single frame of the interferogram stack. This type of noise is a combined result of a sudden shock of the system causing fringe aberration at a time point which is above the phase unwrapping identification limit and CCD mal-sampling in a frame. This case could be identified when calculating the energy or mass evolution of the system by integral over space as a function of time. Minor isolated points, due to the result of peak noise, are easily distinguished due to the incontinuity due to there existence in a theoretically continuous curve. Hence, they are eliminated without a lot of effort.

- An extra aberration is introduced also in the process of phase unwrapping. Extraction of the reference zero phase at $t = t_0$ when having a refractive change locally, the shift $2\pi n + \phi_{shift}$ with range capable of identification is within a 2π range $\phi_{shift} \in [\pi, \pi)$. Therefore, one would expect an extra $2\pi n$ total phase shift of the measured phase change entering Eq. 2.5. Strictly speaking, this aberration is not in the category of noise but a legacy of aliasing from the data processing algorithm. But since same algorithm is used to eliminate peak noise, it is placed in this categorization for integrity reason only.

Corresponding to the sources of noise or error mentioned above, several methods for compensation are developed. In Section 3.1, the temperature data measured is calibrated using a fixed reference point with a known unwrapped phase to get rid of the shift. For this purpose, a point ($\vec{r'}$), far away from the gadolinium plate is introduced at which I set $\Delta T(\vec{r'}) = 0$. In the present experiment, this is physically correct over a time span of about 7...8 s, i.e. before the thermal front reaches the rear vertical boundary of the MZI section.

As for MHD convective heat transfer enhancement experiment in Section 3.2, a fixed point with a known temperature data is hard to find. But certain area, far away from the measurement region of interest with a vanishing temperature change, meaning $\Delta T \approx 0$, could be identified. The reference refractive index for compensation purpose is calculated by first applying a spatial filtering, $\sigma = 20$, $\mu_x = \mu_y = 26$ and N=50 in this region. The purpose of this step is to eliminate spatial error for an arithmetic mean to compensate an overall refractive index shift.

While for the work presented in sec. 4.1, due to an overlapping of temperature and concentration field. An approach combining multiple methods is used to decouple the two variables in refractive index and to compensate the measurement refractive index to a real one.

$$\Delta n_m(\vec{r},t) = \Delta n_c(\vec{r},t) + \Delta n_T(\vec{r},t) + n_n(t) \tag{2.12}$$

To get rid of $n_n(t)$ and gain access to the contributions $\Delta n_c(\vec{r},t)$ and $\Delta n_T(\vec{r},t)$, here an algorithm for data post-processing which is called a two-step compensation algorithm is developed and introduced. This algorithm takes into account the dynamics of mass and heat transport in the system. Referring to the physical picture, given in Fig. 4.4, the mass and heat in the system can be considered as the sum of a conserved field and corresponding flux terms across the boundaries. The conserved parts and time-dependent transient parts of heat and mass are combined into a conserved field $\Delta n_{cons}(\vec{r},t)$ and a time-dependent transient term $\Delta n_t(t)$, respectively. This allow to rewrite Eq. (4.8) into

$$\Delta n_m(\vec{r},t) = \Delta n_{cons}(\vec{r},t) + \Delta n_t(t) + n_n(t), \tag{2.13}$$

The definition of the conserved part of the refractive index field is that its integration over the field of view $A = Y \cdot Z$ (Y=Z=10 mm) gives

$$\iint \Delta n_{cons} dA = 0. \tag{2.14}$$

Thus its derivative with respect to time also vanishes:

$$\partial_t \iint \Delta n_{cons} dA = 0. \tag{2.15}$$

Note that a matrix is hidden beyond each refractive index field, given by the resolution of the camera (1600 x 1200). Making use of Eq.(2.14) and integrating Eq.(2.13) along the y-z plane in space, one obtains

$$\begin{aligned} \iint \Delta n_m dA &= \iint \Delta n_{cons} dA + \iint \Delta n_t dA + \iint n_n dA \\ &= 0 + \Delta n_t \cdot A + n_n(t) \cdot A \end{aligned} \tag{2.16}$$

Eq.(2.16) offers us two possibilities. In the first step, the time-dependent transient part Δn_t can be obtained via:

$$\Delta n_t = \frac{1}{A} \iint \Delta n_m dA - n_n(t), \tag{2.17}$$

The noise term $n_n(t)$ is not known beforehand. However, the analysis of the results shown later in Fig. 4.5 demonstrates that the noise in the experiment is both of a significantly higher frequency and of a much smaller amplitude than Δn_t. Therefore, a suitable fitting of Δn_t as carried out in Section 4.3 eliminates $n_n(t)$ and allows to extract Δn_t in the first step of the algorithm.

Differentiating Eq.(2.16) with respect to time under the constraint of Eq. 2.15 delivers

$$\begin{aligned} \partial_t \iint \Delta n_m dA &= (\partial_t \Delta n_t + \partial_t n_n) \cdot A \\ &= \partial_t (\Delta n_t + n_n) A. \end{aligned} \tag{2.18}$$

Upon invoking Eq.(2.13), Eq.(2.18) leads to

$$\partial_t \iint \Delta n_m dA = \partial_t (\Delta n_m - \Delta n_{cons}) A. \tag{2.19}$$

Integrating Eq.(2.19) is obtained, in the second step of the algorithm, the desired Δn_{cons} by

$$\Delta n_{cons} = \Delta n_m - \frac{\iint \Delta n_m dA}{A}. \tag{2.20}$$

2.1.2 Particle image velocimetry (PIV)

The velocity field of transparent fluid is measured by means of particle image velocimetry (PIV), as illustrated in Fig. 2.6. For this purpose, the solution was seeded with buoyancy-neutral polystyrene particles (9.6 μm mean diameter with density 1.05 g/cm^3 microparticles GmbH). The tracer particles are essential for this technique, since the velocity field of the fluid is calculated from their movement. Due to Stokes number,

$$St = \frac{t_0 u_0}{l_0} \tag{2.21}$$

where relaxation time is defined as $t_0 = \frac{\rho_p d_p^2}{18\mu}$. u_0 is the mean flow velocity; μ the dynamic viscosity of the fluid; l_0, ρ_p are the characteristic length and density of particle, respectively. For a good tracing accuracy of particles with respect to inertia effects, the Stokes number should be much smaller than one. At the same time, the settling velocity of the particles should be much smaller than the velocity of the flow. Both conditions are fulfilled better by sufficiently small particles. But on the other hand, they also have to be big enough so that they scatter the illuminating light with sufficient intensity, cf. Mie theory [122]. In this way, they appear with a good contrast to the background in the grayscale figure sampled by the CCD camera. The corresponding optical setup is described in the following.

A light sheet, generated by a laser diode with a wavelength of 620 nm in combination with a cylindrical lens, was employed to illuminate a vertical 2D plane as shown in Fig. 2.6. The light scattered by particles moving inside this plane was recorded perpendicular to the light sheet by a lens system and a DALSA 21-2M30 camera working in a 1 $\times$ 1 binning mode with up to 30 frames per second. The resulting 1600 pixel $\times$ 1200 pixel pictures were analyzed using the cross correlation algorithm of a commercial PIV software (PivTec Göttingen Germany). This cross correlation algorithm computes the displacement of the tracer particles in small sub-areas of the image (interrogation windows). Hence, every interrogation window yields a vector of the PIV velocity field.

2.1.3 Ultrasound doppler velocimetry (UDV)

Laser PIV provides velocity data in medium which is optically transparent or at least translucent. However, for those which are completely opaque to visible light, ultrasound or electromagnetic wave of other wavelength other than visible frequency such as X-ray radiography could be applied. Ultrasound include no ionized radiation, hence is cost-effective because it is free of insulation chamber and cheaper in devices. It has large field of view possible when multiple transducers are used. In the dissertation, an ultrasound echo based

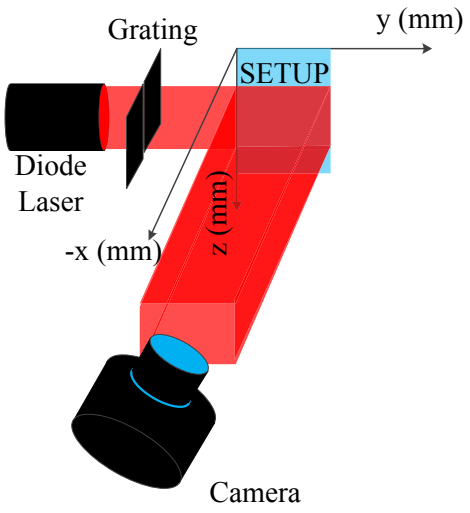

Fig. 2.6 Illustration of Particle image velocimetry 2D velocity measurement system

velocity measurement technique is applied for resolving spatially 1D velocity profile in a GaInSn room temperature liquid metal channel flow.

Sound wave, unlike light, is a form of longitudinal mechanical wave in fluid medium. Meaning that the propagation direction of sound is the same as the wave oscillation direction. Human can only hear sound in the range of approx. 16 to 16,000 Hz. The term ultrasound refers to mechanical oscillations, whose frequencies vary between 16 kHz, the upper audio limit of the human ear, and 10^{10} Hz. Like light, sound waves also refract according to Snell's law, $\frac{sin(\theta_1)}{sin(\theta_2)} = \frac{v_1}{v_2}$, when it propagate from one medium to another. This has to be taken into consideration when reconstructing the velocity distribution when the sound direction is not perpendicularly penetrated through different phases. This is because the velocity measured by UDV is the velocity projection along and at the ultrasound propagation direction.

The working principle of UDV, also called pulse wave doppler velocimetry, is based on the evaluation of phase shifts between pulse emissions. In fact, doppler effect of ultrasound is not a major phenomenon to be resolved in this technique. Transducer emits a harmonic ultrasound pulse with a frequency of f_e. The wavelength of the pulse is determined by the wavelength λ_e of ultrasound and repetitions of wavelength within a single pulse.pulse ultrasound with frequency of f_e. Since the size of tracing particles are much smaller than the ultrasound wavelength, smaller portion of wave scatters. The echo ultrasound is then sampled by the same transducer. Position of the particle is

$$P = \frac{c \cdot t_d}{2} \tag{2.22}$$

with speed of sound in this certain media. c and t_d are the time between the sending and perceiving of the ultrasound. The time between pulse emissions is t_{prf}. Therefore, the particle moves, with speed v_P at an angle θ_P with respect to the ultrasound propagation direction, a distance of

$$\Delta P = P_2 - P_1 = v \cdot t_{prf} \cos\theta_P = \frac{c}{2} \cdot \Delta t' \tag{2.23}$$

$\Delta t'$ is the time difference between time of flight for second and first pulse emission is $t_{d2} - t_{d1}$. Thus, the perceived wave shift of the ultrasound wave is

$$\phi_{t_{prf}} = \frac{2\pi c \Delta t'}{\lambda_{t_{prf}}} = 2\pi \cdot f_e \cdot \Delta t' \tag{2.24}$$

Combining Eq. (2.23 and 2.24), velocity of the particle at this distance is then obtained

$$v = \frac{c \cdot \phi_{t_{prf}}}{4\pi \cdot f_e \cdot \cos\theta_P \cdot t_{prf}} = \frac{c \cdot f_d}{2 f_e \cdot \cos\theta_P} \tag{2.25}$$

with f_d the frequency of the shift frequency of ultrasound echo. In order to determine the frequency shift An autocorrelation technique is used to determine the frequency shift [123]. Since the algorithm is sampling discretized phase shift of a continuous wave, Nyquist limitation should be fulfilled. Therefore, the maximum velocity which could be measured is when $\phi_{t_{prf}} = \pi$. This dissertation uses an ultrasound multimeter from Signal Processing DOP3010 to allow a scan of maximum 10 UDV transducers in a defined sequence. The transducer, piezo diameter 10 mm with 8 MHz emission frequency, uses a deported matching impedance option. By departing the electrical matching component from the transducer main body, a direct operation and measurement of UDV transducer in magnetic field is possible.

2.1.4 Thermocouple temperature measurement system

Thermocouples are used in conjunction with interferometer for temperature measurement. A digital multimeter together with switching and scanning card from Keithley is used for switching between different channels sampling the electric potential and convert to temperature data. The system as used here is Keithley 2700/ 3706A which is an integration of a 6.5/ 7.5 digital resolution digital multimeter combined with a switching system providing a real time monitoring of point temperature measurements with thermocouple. Type E thermocouple is used due to its fine performance in a changing magnetic field. The system is controlled by a labview program developed. This configuration provides a fully automatic

measurement environment which allows an automatic sampling, visualization and storage of temperature data working together parallel with other systems used without any cross talk.

2.2 Theory and numerics

This section introduces the simulation frames which is used throughout this dissertation. Based on the two groups of governing equations relevant here, this section is divided into two parts. 1. magnetism and electricity simulation and 2. transport process of heat and mass.

2.2.1 Simulation of magnetic and electric field and the resulting force field in MHD and FHD

The AC/DC module in COMSOL solves magnetostatic equation to get the stray field of permanent magnet and demagnetization field inside it. It is derived from Ampere's law

$$\nabla \times \vec{B} = \mu \vec{J} \tag{2.26}$$

Since there's no external potential field applied, induced current in Faraday's law, see 1.13, the curl of $\vec{B}$ is nullified. Therefore, the constitutive equation, see 1.8, becomes $\vec{B} = \mu \vec{H} + \vec{B}_r$. With this, Ampere's law becomes

$$\nabla \times (\mu^{-1}(\vec{B} - \vec{B}_r)) = \nabla \times \vec{H} = 0 \tag{2.27}$$

where $\vec{B}_r$ is the remanent magnetic flux density of the permanent magnet taken from the manufacturer. Using the definitions of magnetic scalar potential, $\vec{H} = -\nabla\psi$, the non-solenoidal nature of $\vec{B}$ and the constitutive equation, the magnetic vector potential is obtained by solving $\nabla^2\psi = \nabla \cdot \vec{B}_r/\mu$. With the finite element solver in COMSOL, the stray field of the permanent magnet $\vec{B} = \mu\vec{H}$ is obtained for the area of interest.

In low conducting medium, an external potential is applied to generate electric current. The governing equation for low conducting media are Ohm's law neglecting electromotive force(EMF) since the fluid is at rest in simulation condition; and resulting electric potential equation from Ohm's law plus the divergence-free current density

$$J = -\sigma \nabla \phi \tag{2.28}$$

$$\nabla \cdot (\sigma \nabla \phi) = 0 \tag{2.29}$$

By using COMSOL EC module, electric potential and current density in the low conducting media is simulated. Parameters and results of this part of simulation are shown in Sec. 3.2. Taking a harmonic mean at interface of materials with different electric conductivity, governing equation of electric potention reduces to Laplace equation, see Eq. (2.29). This could also be solved by using FDM scheme which is to be presented in the following section.

Current density is simulated in flowing high conducting media at a static magnetic field to verify the simulation in a fully studied Hartmann flow. With the simulation scheme established, induced current in static conducting media with transverse moving magnet, cf. Sec. 3.3 is simulated to account the significance of this extra term.

Given a fully developed laminar flow inside the duct, Navier-Stokes equation neglecting gravity is reduced to 2D Poisson equation with a velocity field pointing to its flow direction (here along the x-direction)

$$\mu_f \nabla^2 v_f = \mu_f \left(\frac{\partial^2 v_x}{\partial y^2} + \frac{\partial^2 v_x}{\partial z^2}\right) = -\nabla P \tag{2.30}$$

Given no slip boundary condition and a mean flow velocity of 30 mm/s, velocity profile is obtained by solving Eq. (2.30) with the fast Poisson solver [124, 125], see Fig. 2.7. Cross section is a rectangular duct with 10 mm to each side. Eq. 2.30 is solved with a 9-point discretization scheme with an O (Δx^4) truncation error [125–127].

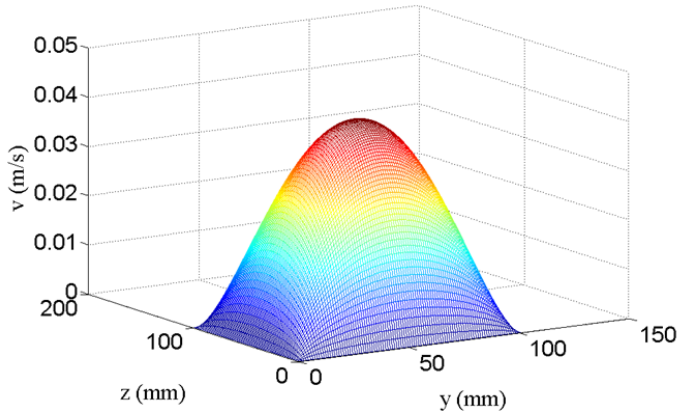

Fig. 2.7 Velocity profile in cross section perpendicular to flow direction of a 2D fully developed poisson flow.

As has been discussed briefly in Sec. 1.3.1, the magnetic field can influence the velocity distribution of the fluid with a high electric conductivity, e.g. Hartmann flow with sufficiently high Ha number. Current density is computed according to Ohm's law with relative moving

conducting material in magnetic field

$$\vec{J} = \sigma(-\nabla\phi + \vec{v} \times \vec{B}) \tag{2.31}$$

Since displacement current could be neglected, current density is hence divergence-free $\nabla \cdot \vec{J} = 0$. Therefore, the electric potential equation is rewritten as

$$\nabla^2\phi = \nabla \cdot (\vec{v} \times \vec{B}) \tag{2.32}$$

With Eq. (2.31 and 2.32), the induced current density is computed for a 2D fully developed Poiseuille flow, see Fig. 3.26a.

With induced current density of liquid metal flow in a static magnetic field, the velocity distribution at cross section perpendicular to flow direction is altered from 2D Poiseuille to 2D Hartmann. This is experimentally resolved in Sec. 3.3 with UDV technique measuring velocity distribution in between Shercliff walls, i.e. the counter walls which is parallel to magnetic field. With the same algorithm established and tested just now, current density induced by a periodically transverse moving magnet with speed of 30 mm/ s along transverse direction is simulated and presented in Fig. 3.26b. Impact on this secondary induced current will be addressed in Sec. 1.3.1.

2.2.2 Transport processes in liquid phase coupling MHD and FHD

Momentum equation of the liquid are modified by two extra body force, namely Lorentz force and Kelvin force, cf. Sec. 1.3. Generally, Navier-Stokes equation is rewritten as

$$\rho(\frac{\partial \vec{v}}{\partial t} + \vec{v} \cdot \nabla\vec{v} = -\nabla p + \mu\Delta\vec{v} + \vec{f_m} + \vec{f_L} + \vec{f_g} \tag{2.33}$$

where f_m, f_L and f_g are Kelvin force, Lorentz force and gravitational force density, respectively. Given a quasi static condition, body force f_m and f_L are readily obtained according to Eq. 1.12 and 1.21 with simulated current density and magnetic field. For the transport equation, the velocity and mass(c) or temperature(T) field steps in

$$\frac{\partial T}{\partial t} + \vec{v} \cdot \nabla T = \kappa \cdot \nabla^2 T + S_T \tag{2.34}$$

$$\frac{\partial c}{\partial t} + \vec{v} \cdot \nabla c = D \cdot \nabla^2 c + S_c \tag{2.35}$$

with heat diffusivity κ, mass diffusivity D and source term S_T for heat and S_c mass. Thermodynamic properties are regarded constant and given in the corresponding sections. Transport

processes to be simulated are fluid at rest, the convective-diffusion equation in Eq. (2.34 and 2.35) are simplified to diffusion case. A finite difference scheme is used to resolve this linear partial differential equation which general form in 2D is

$$\frac{\partial \Phi}{\partial t} = A(\frac{\partial^2 \Phi}{\partial x^2} + \frac{\partial^2 \Phi}{\partial y^2}) \tag{2.36}$$

with diffusivity A in unit $1\,\mathrm{m}^2/\mathrm{s}$ and source term is neglected. The thermal boundary of two phases, subscripted with 1 and 2, within the simulation area adopt a harmonic thermal boundary

$$k = \frac{k_1 k_2}{k_1 + k_2}. \tag{2.37}$$

For simplicity, an explicit discretization with a truncation error O(Δt) and O(Δx^2) for uniform grid in space and time, respectively, is used

$$\Phi_{i,j}^{n+1} = \Phi_{i,j}^{n} + \frac{A\Delta t}{\Delta x^2}(\Phi_{i-1,j}^{n} - 2\Phi_{i,j}^{n} + \Phi_{i+1,j}^{n}) + \frac{A\Delta t}{\Delta y^2}(\Phi_{i,j-1}^{n} - 2\Phi_{i,j}^{n} + \Phi_{i,j+1}^{n}). \tag{2.38}$$

Upon fulfilling stability condition $\frac{A\Delta t}{\Delta x^2} = \frac{A\Delta t}{\Delta y^2} \leq 0.5$, 2D Φ is obtained with given initial condition and boundary conditions which is declared in corresponding sections. This is done by iterating Eq. (2.38) along space with given Φ from last time step layer. Essentially, finite volume method is also used but due to the truncation error of the residual in finite difference method is ignorable, the two methods obtain roughly the same result. [128–130].

2.3 Chapter summary

This chapter presents the major measurement systems which are used in later parts of this dissertation. The theoretical background of the techniques are introduced with an emphasis on the development made here. Numerical schemes of physical fields, namely magnetic, electric, diffusion temperature and mass field, are introduced.

Chapter 3

Heat transfer in magnetic cooling

This chapter is dedicated to the investigation of heat transfer process in a simplified section of a parallel plate magnetic regenerator bed. A Mach-Zehnder interferometer is used to map the temperature field inside the transparent heat transfer fluid. First, a testing experiment for the validation of the measurement system is conducted. An organic fluid, n-decane, was selected as the heat transfer fluid. The reason was due to its low thermal diffusivity which makes the spatial temperature distribution better resolvable by interferometer, cf. Ref. [131]. After proving that a temperature difference to O(10 mK) is resolvable, n-decane was replaced by 0.5 M NaOH aqueous solution. This guarantees a corrosion free operation for Gd and a better heat transfer due to its similar thermodynamic property to that of water. Transparent ITO glasses are used as electrodes. When magnetic field is present, Lorentz force is formed forcing MHD convection and is quantified by PIV. By this means, heat exchange is faster between the fluid and solid Gd plate proving that MHD is a tool which has a potential on heat transfer enhancement, cf. Ref. [70]. Furthermore, a room temperature liquid metal GaInSn is tested as heat transfer fluid in magnetic cooling. This is primarily motivated by its small Prandtl number Pr=$\frac{C_p \mu}{k}$=0.029 [73–75] and high thermal diffusivity $\kappa_{GaInSn} = \frac{k}{C_p \rho} = 1.03 \times 10^{-5}$ m^2/ s. Thus, the fluid oscillating periodically between the hot and cold end of the regenerator is slow to save pump power. Given small Pr number, thermal boundary layer extend itself beyond the velocity boundary layer. Therefore, heat transfer is not minimized by conduction in laminar flow boundary layer. Besides, high thermal diffusivity ensures a faster releasing of energy in the regenerator. However, due to its rather high electric conductivity, even without external electric potential, considerable amount of current density would be generated with a relative motion of conducting fluid inside a magnetic field. This has an impact on velocity field which is studied by UDV, cf. Ref. [72].

3.1 Interferometer study of the thermal boundary layer at a periodically magnetized gadolinium plate

3.1.1 Experimental and numerical

Gadolinium (Gd) plates (99.5 % pure, Jiangxi South Rare Earth Hi-Tech Co., Ltd.) were used as the MCM. Each Gd plate has an area of 9.6×9.6 mm^2 and a thickness of 0.8 mm which results in a mass of 0.58 g. They were polished to a roughness of less than 0.01 mm. Two NdFeB permanent magnets ($50 \times 30 \times 12$ mm^3) generated a magnetic field of 350 mT inside a gap of 15 mm with an inhomogeneity of less than 3 mT. The pair of magnets is mounted on a 1-D motorized translation stage. It was moved with a speed of 3 mm/s toward and away from the Gd plates along the y-direction (cf. Fig. 3.1) to generate a periodic magnetic field which acts perpendicular to the Gd plates. In this orientation the impact of the demagnetization field, H_{dem}, is significant ([28, 64, 132]). At the given relatively low flux density of $B_{ext} = \mu_0 H_{ext} = 350$ mT the internal magnetic field $H_{int} = H_{ext} + H_{dem}$ amounts to only approx. 30% of $\mu_0 H_{ext}$ ([132]). As a result, ΔT_{ad} is considerably reduced compared to a magnetization parallel to the Gd plate. This disadvantage is balanced by the fact that the optics has free access along the z-axis of the cell and the available ΔT_{ad} can still be comfortably measured by the interferometer.

The comparatively low speed (3 mm/s) of the movement magnet was selected for two reasons. First, it guaranteed that only a low level of perturbing vibrations was transferred to the interferometer. Second, it enables to study the impact of a continuous instead of instantaneous magnetization and demagnetization, respectively, as also adopted in the source term formulation of the MCE in the energy equation of recent numerical models ([53, 59, 60]). The time span between applying and removing the magnet was deliberately chosen to be $\Delta t = 120$ s because it is of more importance in mapping the transient behavior until steady state is reached.

Initially the measurements of the temperature change of the Gd plates during these cycles were performed with 0.25 mm thick calibrated, ungrounded Type E thermocouples. For this purpose, two thermocouples were attached directly at the center of each of the Gd plates and immediately sandwiched by the other Gd plate without any notable air gap between thermocouples and Gd plates. Additionally, this setup, referred to as *Gd plates-thermocouple sandwich* in the following, was embedded into a thermal insulation. Finally, the thermocouples were connected to a digital multimeter (Keithley 2700 including switching model 7708). The temperature data gained by the thermocouples later served as calibration data for interferometric measurement. First, the magnetocaloric effect of Gd plate given

magnetic field shown in Fig. 3.1a is meassured by thermocouple. This data in conjunction with extrapolation algorithm presented later in 3.1.4 provide reconstructed temperature field in thermal boundary at the vicinity of Gd plate.

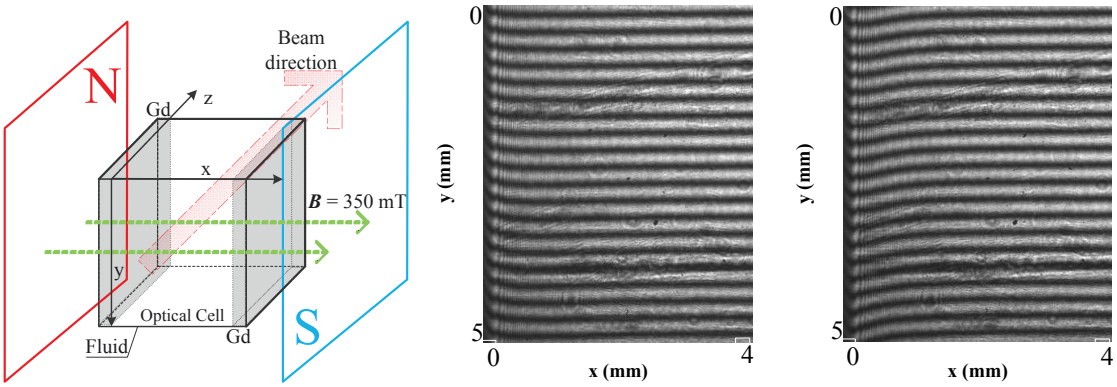

(a) (b) (c)

Fig. 3.1 Experimental setup (a) and the interferograms at 0 s (b) and after 4s of magnetization (c). The Gd plate is located at the left margin of (b) and (c).

In the next step, two nearly identical Gd plates were glued at the opposite side walls of an optical cuvette (Hellma) with an inner geometry of $10 \times 10 \times 10$ mm^3, see Fig. 3.1. The resulting space between the gadolinium plates is W=8.4 mm which was filled with n-decane as the heat transfer fluid. Each set of experiments was repeated at least 3 times and temperature data is extracted via a Interferogram processing algorithm described in sec 2.1. Though an optical table is used, there is still a low level of vibrations, e.g. arising from the motorized translation stage for mounting permanent magnets. These vibrations lead to a shift in $\phi_0(\mathbf{x},\mathbf{t})$ over time. To get rid of this shift, the temperature data measured needs to be calibrated using a fixed reference point with a known unwrapped phase. For this purpose, the point (x_c, y_c) in the center of the x-y plane of the optical cell is used because $\Delta T(x_c, y_c) = 0$ K for a timespan of several seconds before the thermal front from the magnetized Gd plates approaches this point has a predictable temperature. Obviously, after a certain critical time the assumption of $\Delta T(x_c, y_c) = 0$ K is no longer accurate and there is no longer a correct reference point. As a result, an artificial overall decrease in the temperature magnitude occurs and the interferometric method becomes inaccurate. Based on the data shown in Secs. 3.1.3 and 3.1.5 a critical time of 5 sec can be estimated.

Preliminary experiments with water as the heat transfer fluid, even with anti-corrosion additives, have shown a rapid corrosion of the gadolinium. The resulting gas bubbles at the Gd plates prevent the resolution of the thermal boundary layer by means of interferometry. To quantitatively support the selection of a heat transfer fluid, more suitable for temperature

measurements with the MZI, simulations were conducted using finite difference method described in sec 2.2.2.

For this purpose, it is sufficient to consider the one-dimensional unsteady heat conduction equation

$$\frac{\partial T}{\partial t} = \frac{k}{\rho C_p}\left(\frac{\partial^2 T}{\partial x^2}\right) \tag{3.1}$$

which is discretized according to Sec. 2.2.2. In Eq.(3.1), T, x, k, ρ and C_p refer to the temperature, the co-ordinate normal to the Gd plate, heat conductivity (0.1209 W/m·K), density (730 kg/ m^3) and specific heat capacity (2.22 J/(g·K)) of n-decane, respectively. Energy is conserved in Gd - n-decane system. Fluid is simulated using a semi-infinite model with x = 0 mm as n-decane Gd boundary with sufficient length in positive x direction. For fluid at x = 0 mm, a third-kind, mixed, boundary condition with a harmonic mean heat conductivity is used. This means heat flux from the Gd plate to the fluid is calculated with Fourier conduction law $Q = k\frac{T_{Gd}-T_1}{\Delta x}$. Gd temperature is upgraded in each time layer according to energy conservation given by $T_{Gd}^{t+\Delta t} = T_{Gd}^{t} - \frac{Q\cdot\Delta t}{C_{pGd}m_{Gd}}$. Note that although the heat conductivity of Gd is rather small, at $k_{Gd} = 10.6$ W/mK, it is still about ninety times larger than that of n-decane ($k_{fluid} = 0.1209$ W/mK). The Biot number, Bi, quantifying the ratio between conduction and advection of heat is estimated using

$$Bi = \frac{hd_c}{k_{Gd}} \tag{3.2}$$

where $d_c = 0.8$ mm represents the thickness of the Gd plates and $h = \frac{Q}{A\Delta T}$ is the heat transfer coefficient; A refers to the area of the Gd plates. Quantitative values for $\frac{\Delta Q_f}{\Delta Q_0}$ and ΔT shown in Sec. 3.1.3 lead to $O(Bi) \sim 0.01$. Hence, to estimate the performance of the heat transfer fluid in the present experiment, it is completely justified to neglect temperature inhomogeneities in the Gd plate related to the demagnetization field ([64]) and to regard the temperature distribution in Gd as homogeneous during the entire heat transfer process simulated. The initial condition was the same as in the experiment, i.e. a pulse-like temperature increase in Gd of the same magnitude as measured with the thermocouples. Natural convection during heat transfer can be neglected safely due to the small Biot number.

The time history of $T(x,t)$ was simulated for several heat transfer fluids, including water and several organic liquids. Fig. 3.2 shows the 1-D temperature profile $T(x)$ normal to the Gd plate as time progresses after applying $\Delta T_{ad} = 0.35$ K for water and n-decane, which turned out to be the best compromise. In the very beginning, both fluids show a measurable ΔT of about 0.3 K. However, by virtue of the rather high thermal diffusivity $\kappa = \frac{k}{\rho C_p}$ of water this ΔT is diminished to less than 0.1 K within about 5 seconds, see Fig. 3.2a. By

contrast, measurable values above the resolution limit of the MZI (0.007 K) can be obtained for considerably longer time for n-decane (Fig. 3.2b).

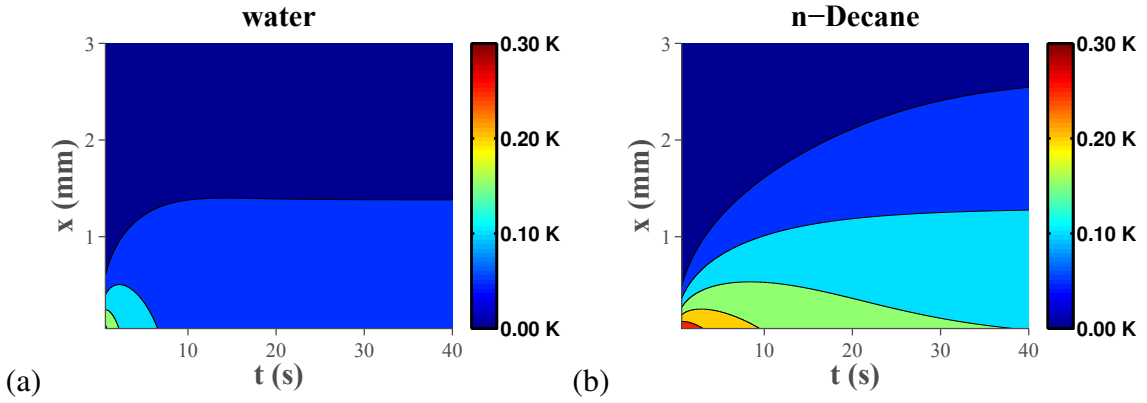

Fig. 3.2 Simulated 1-D temperature profile in water (a) and n-decane (b). The vertical axis refers to the distance normal to the Gd plate, the horizontal axis to time. The value of $T(x,t)$ is shown in the colorbar.

Another argument in favor of n-decane is the parameter $\frac{\partial n}{\partial T}|_{T=273\mathrm{K}}$. For water it amounts to $\frac{1}{10200}$ 1/K, while n-decane has $\frac{1}{2230}$ 1/K ([133]). Hence, for the same ΔT, the phase shift in water is only approximately $\frac{1}{5}$ of that in n-decane. In this case it is not resolvable because of the signal's same order of magnitude as the noise. Experimental tests with water support this finding. This does not imply that water is not a good candidate for a heat transfer fluid. It only shows that it is not of use for temperature measurements with a MZI. By contrast, aqueous solutions of NaOH are suited, as shown in Sec. 3.2.

3.1.2 Temperature measurements with thermocouples

Fig. 3.3 shows the temperature changes at the surface of the gadolinium plates during one complete cycle of magnetization and demagnetization, measured in the *Gd plates-thermocouple sandwich* by two thermocouples placed in the center of the surface of each plate at room temperature with $T_0 = 295.2 \pm 0.2$ K. Immediately after magnetization, the temperature rises by $\Delta T = 0.35 \pm 0.05$ K, to exponentially decrease later on to T_0. In the subsequent demagnetization phase, there is an increase of $\mid \Delta T \mid$ by 20 mK compared to the magnetization process. This is in line with the discussion by [134] on the reversibility of the MCE, requiring $\Delta T_{ad,mag}(T) = -\Delta T_{ad,demag}(T + \Delta T_{ad,mag})$. Because the operation frequency is very low in this case, leading to a relaxation of T to close to T_0, the ΔT_{ad} of both phases differ slightly. After the magnet is removed, the temperature rapidly drops by $\triangle T$ to approach T_0 again in an exponential manner.

Since care was taken to avoid heat losses from the *Gd plates-thermocouple sandwich*, the measured $\Delta T = 0.35$ K equals the adiabatic temperature difference ΔT_{ad}. This value is only approx. 30% of the value reported by [134] (Fig.3d) which was obtained for a $\vec{B}$ parallel to the Gd plate, i.e. perpendicular to this orientation. Thus, the reduced ΔT_{ad} reflects the influence of the larger H_{dem} as discussed above.

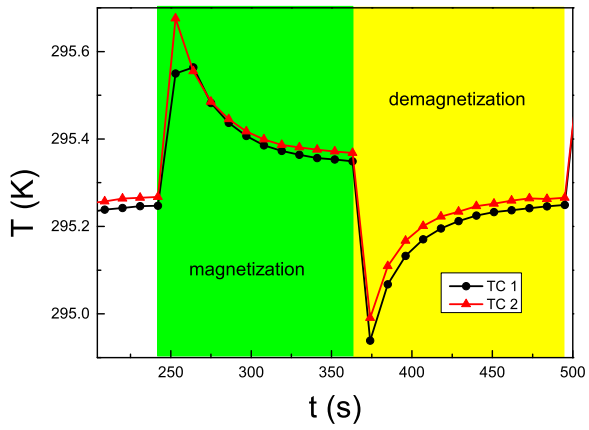

Fig. 3.3 Temperatures of the Gd plate surface measured by thermocouples (TC) during a full cycle of magnetization and demagnetization.

3.1.3 Space- and time-resolved temperature fields in n-decane

The results of the temperature measurements in n-decane by means of the MZI are shown in Fig. 3.4. The two Gd plates are placed vertically at both sides of the glass cell parallel to the measurement arm of the M-Z interferometer. In the following, focus is only on the behavior of the left Gd plate; that of the opposite plate is nearly mirror-symmetric. Fig. 3.4 offers a good view of the formation of the thermal boundary layers at the Gd plate during the first 5 seconds of magnetization (left column) and demagnetization (right column). The figure underlines that even small changes in the temperature field can be resolved well by means of the MZI. The spatially delayed release of the thermal energy generated by the MCE due to the finite speed of the magnet motion is clearly visible. During magnetization, the upper part of the Gd plate is first exposed to the magnetic field. By contrast, it is the lower part of the plate which first escapes from the magnetic field during demagnetization. As a result, the thermal front propagation at early time is most advanced in these parts as documented by Fig. 3.4(a-b). Thus, a temperature gradient in n-decane develops parallel to the Gd plate. Further magnet motion and heat conduction in the fluid reduces this effect until it nearly completely vanishes at around 5 seconds.

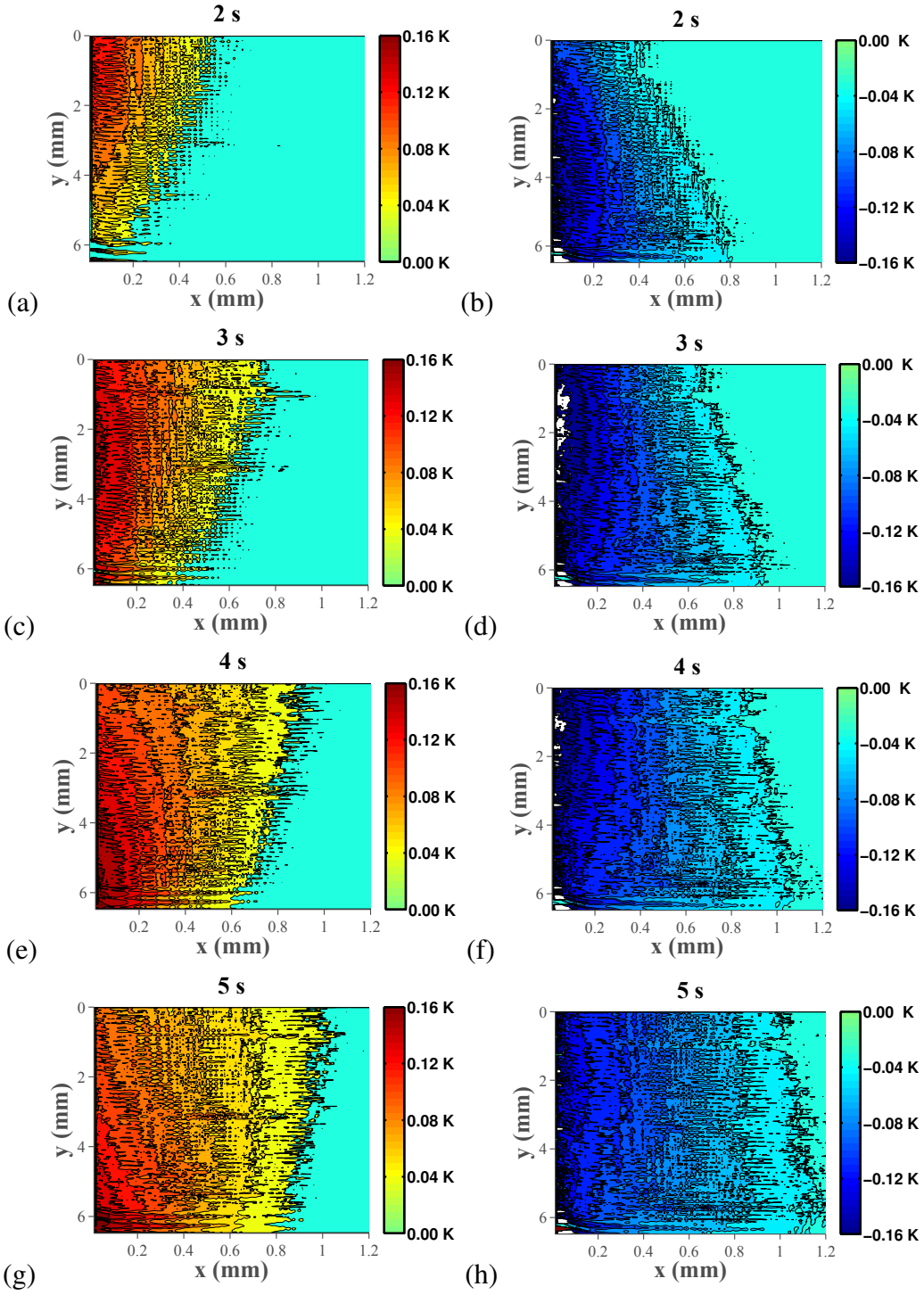

Fig. 3.4 Temperature field at different times during magnetization (a, c, e, g) and demagnetization (b, d, f, h) in the heat transfer fluid n-decane. The line $x = 0$ represents the interface between the Gd plate and n-decane, i.e. the Gd plate is placed immediately at the left vertical margin of each subfigure. Each picture maps a window of 6.5 mm in y-direction along the central part of the Gd plate times a distance of 1.2 mm in x-direction normal to the Gd plate.

Fig. 3.5 shows the propagation of the thermal front in more detail. For this purpose the x_f-position of the isotherm belonging to $\Delta T = 0.02$ K was tracked as time passed. In view of the curved shape of the ΔT isotherms, tracking was performed in the center of the Gd plate, where the influence of the finite magnet speed is minimal, and perpendicular to the Gd plate, i.e. along the y-direction. There are two main reasons for the minor differences

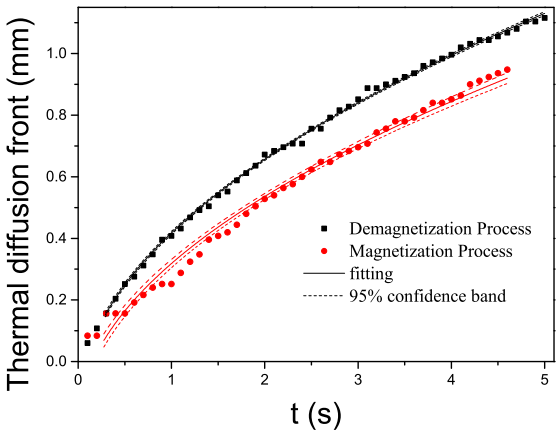

Fig. 3.5 Propagation of the thermal diffusion front, given via its x-position x_f belonging to the isotherm to $\Delta T = 0.02$ K, during magnetization and demagnetization. The fit (solid black line) during demagnetization is $x_f = \sqrt{4.45\kappa_f \cdot t} - 159\ \mu$m and during magnetization is $x_f = \sqrt{3.71\kappa_f \cdot t} - 208\ \mu$m (thermal diffusivity of n-decane: $\kappa_f = 7.46 \cdot 10^{-8}$ m^2/s)

between magnetization and demagnetization. First, due to the rather slow cycling, the Gd plates approach nearly the same initial temperature before the next magnetization or demagnetization. This leads to slightly different ΔT_{ad} for magnetization and demagnetization, respectively, as discussed before. The second reason is flaws in the extraction algorithm of the thermal front position and the resolution of the M-Z interferometer (about 0.007 K). For the demagnetization process, the position of the thermal front can be fitted according to $x_f = \sqrt{4.45\kappa_f \cdot t} - 159\,\mu$m where the thermal diffusivity of n-decane is given by $\kappa_f = 7.46 \cdot 10^{-8}$ m^2/s. A similar relation holds for the magnetization. Hence, both curves show the $\sqrt{\kappa_f \cdot t}$ behavior, as pertinent to diffusion processes. These insights into the dynamics of the thermal fronts might be of use for properly designing of the spacings of a flat-plate AMR for a given working frequency. An overly large distance between the plates wastes space while an overly small spacing can lead to a crossing of the fronts, i.e. to an overlap of the thermal boundary layers, thereby decreasing the gradient and the heat flux.

The temperature profiles normal to the Gd plates in the cell center, derived from the temperature field in Fig. 3.4, are plotted as time progresses during the magnetization and

demagnetization phase in Fig. 3.6. The horizontal coordinate is the distance normal to the surface of the Gd plate. The vertical coordinate is the temperature of the n-decane at the specified position. The development of the T(x) profiles over time is clearly visible. Since

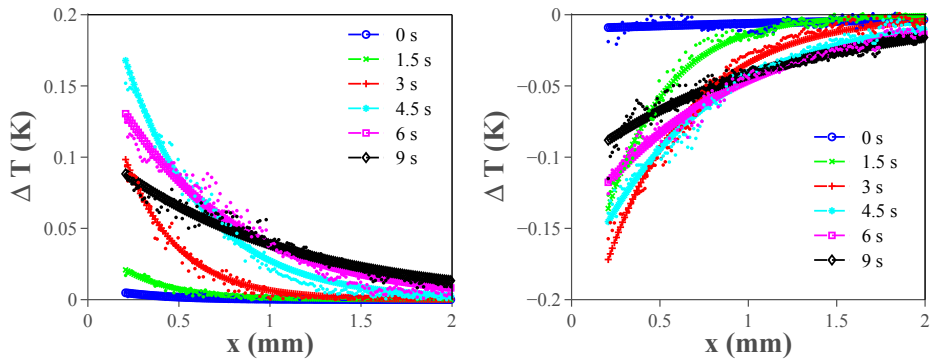

Fig. 3.6 Evolution of the temperature profiles in the heat transfer fluid n-decane next to the Gd plate with progressing time during magnetization (a) and demagnetization (b).

the data are blurred due to superposition with random noise of small magnitude, a fitting via

$$T(x) = A + Be^{-Cx} \tag{3.3}$$

was performed. The agreement between the discrete temperature data obtained after processing the interferometer data is good with a mean square error of 0.006 K. The reason why the maximum temperature rise remains below the $\Delta T = 0.35$ K, as detected by the thermocouples, is because of the fact that the region of the thermal boundary layer very close to the Gd plates is currently not visible for the interferometer. This problem is related to the

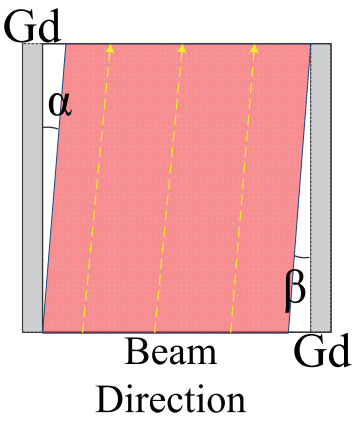

Fig. 3.7 Top view onto the optical cell which shows the area which is visible to the MZI in red color.

difficulties in the adjustment of both Gd plates parallel with the measurement arm of the M-Z interferometer. This leads to a small tilt between the Gd plates and the optic beam, see Figure 3.7. Although the tilt angles α and β are considerably less than 1°, the temperature data over an interval of $\delta x \approx 0.2$ mm near the Gd plate are not directly accessible. To reconstruct the whole temperature profile, a combination of both M-Z interferometer data and thermocouple data was used.

3.1.4 Reconstruction of the complete temperature profile

Due to imperfect parallelization between the Gd plate and the optical beam, a thin layer of the temperature profile near the solid-liquid boundary is not visible for the interferometer, as sketched in Fig. 3.7. To extrapolate T(x) into this region on the basis of the interferometer data fitted by Eq. (3.3), a third-order polynomial is used

$$T_{ex}(x) = ax^3 + bx^2 + cx + d. \tag{3.4}$$

At the borderline between the region visible for the MZI and that not visible, which we call the *fictitious* (fi) boundary in the following, identical temperatures is forced, i.e. $T_{ex}|_{fi} = T|_{fi}$, thus

$$ax^3 + bx^2 + cx + d|_{fi} = A + Be^{-Cx}|_{fi}. \tag{3.5}$$

Three further equations are necessary to determine the unknown coefficients a, b, c and d. The first two equations follow from imposing the differentiability of the function expressed via the identity of the first and second derivatives, i.e.

$$\begin{aligned} \frac{dT(x)}{dx}|_{fi} &= \frac{dT_{ex}(x)}{dx}|_{fi} \\ \frac{dT^2(x)}{dx^2}|_{fi} &= \frac{dT_{ex}^2(x)}{dx^2}|_{fi}. \end{aligned} \tag{3.6}$$

The fourth equation follows from the fact that the temperature extrapolated by eq. (3.4) at the place x=0, where the real physical boundary between the Gd plate and the fluid is located, should be equal to the temperature of the Gd plate T_{Gd}, i.e.

$$T_{Gd} = T_{ex}|_{x=0}. \tag{3.7}$$

T_{Gd} is a priori not known but can determined by means of the energy conservation equation

$$\Delta Q_0 = C_{p,Gd} m_{Gd} \Delta T_{ad} = \Delta Q_{Gd}(t) + \Delta Q_f(t) \tag{3.8}$$

neglecting heat losses from Gd to the air. For ΔT_{ad}, the value $\Delta T_{ad} = 0.35$ K is taken as measured by the thermoelements (Sec. 3.1.2). $C_{p,Gd}$ refers to the heat capacity of Gd which equals $C_{p,Gd} = 0.36$ J/(gK) around T=20°C ([135, 136]). $C_{p,Gd}$ is a function of B and T. Based on [137], it could be estimated the difference between $C_{p,Gd}(B = 350mT)$ and $C_{p,Gd}(B = 0)$ is approximately 1% of $C_{p,Gd}(B = 0)$ at T=20°C. Besides, $C_{p,Gd}$ varies significantly near the Curie temperature. However, admitting the largest $\frac{\partial C_{p,Gd}(T)}{\partial T} = 12$ J/(kgK^2) ([135, 136]), the relative uncertainty of $C_{p,Gd}$ is only about 2% due to the small $\Delta T_{ad} = 0.35$ K. These variations are of the same order as those caused by the extrapolation and therefore neglected.

The heat $\Delta Q_f(t)$ transferred into n-decane is obtained by integrating normal to the Gd plate

$$\Delta Q_f(t) = \int_{x=0}^{x=x_{max}} C_{p,f} m_f(x) T_f(x,t)) dx. \tag{3.9}$$

x_{max} was set to W/2 (W=8.4 mm) which safely captures the propagation distance of the thermal front. For the heat remaining in the Gd plate $\Delta Q_{Gd}|_t$ holds

$$\Delta Q_{Gd}(t) = C_{p,Gd} m_{Gd}(T_{Gd} - T_0) \tag{3.10}$$

with $T_0 = 295.2$ K. This is iterated until the calculated $T_{Gd}|_{x=0}$ is the same as that extrapolated $T_{ex}(x = 0)$, cf. eq. (3.7).

The reconstructed temperature profiles are presented in Fig. 3.8. They now provide a complete overview of the dynamic changes in the temperature field during the magnetization-demagnetization cycle. Also, notably, at nearly $\Delta T = 0.3$ K, the decane temperature at the Gd plate approaches the values measured by the thermocouples. Furthermore, the physical trend, meaning high gradient but small penetration depth at small times, moving toward a lower gradient but a larger penetration depth at the end, is correctly mapped.

3.1.5 Analysis of the heat transfer

To quantitatively evaluate the diffusive heat transfer into the heat transfer fluid n-decane, the temporal evolution of the temperature gradients from the T-profiles in Fig. 3.8 is firstly calculated. For that purpose, the profiles which are explicitly given via the functions $T(x)$ and $T_{ex}(x)$ in eqs.(3.3) and (3.4), respectively, are differentiated. The results are plotted in Fig. 3.9. A rapid decrease in the temperature gradient at the solid-liquid boundary is noted. For instance, in the demagnetization phase the highest gradient at t=0 s is 4.23 K/mm, leading to a heat flux $q = k_f \partial T/\partial x|_{x=0} = 0.51 \cdot 10^{-3}$ W/m^2, with the heat conductivity of n-decane equal to $k_f = 0.1209$ W/mK. After t=3 s the gradient decreases to 0.549 K/mm

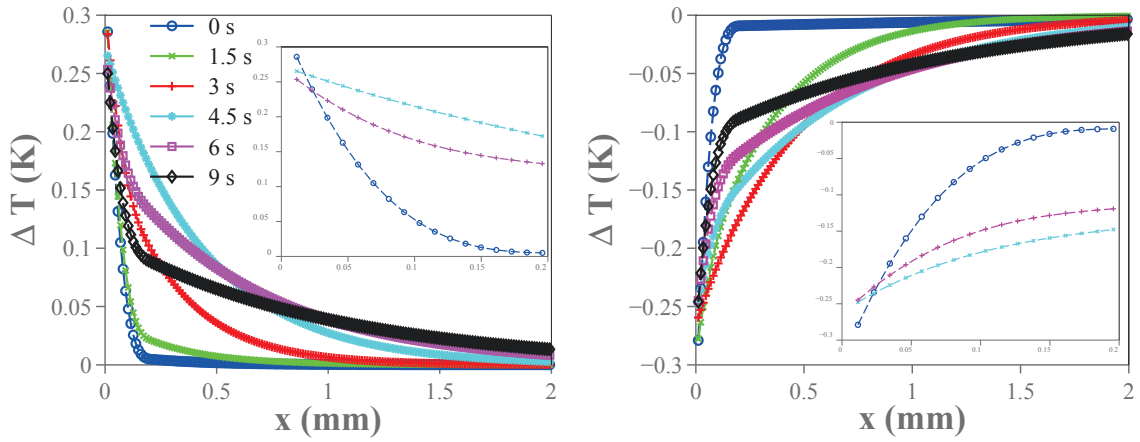

Fig. 3.8 The reconstructed, complete temperature profiles in the heat transfer fluid n-decane during magnetization (a) and demagnetization (b). The insets show a zoom into the first 200 μm of the thermal boundary layer.

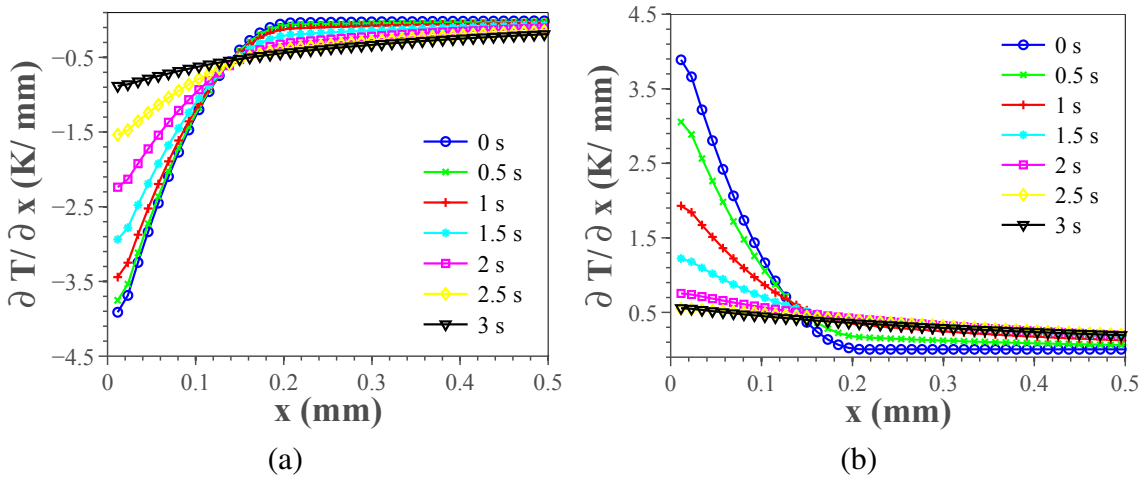

Fig. 3.9 Evolution of the temperature gradient, derived from the profiles in Fig. 3.8, close to the Gd-decane boundary.

with a consequently reduced heat flux of $q = 0.0667 \cdot 10^{-3}\mathrm{W/m^2}$. This implies a reduction of 87% in the first 3 seconds after the start of the heat exchange.

Second, it is useful to look at the thermal energy, ΔQ_f (eq.(3.9), transferred from the Gd plate into the heat transfer fluid. ΔQ_f is normalized with respect to the entire thermal energy ΔQ_0, cf. appendix, eq.(3.8 and 3.9), generated during mag- and demagnetization and plot it in Fig. 3.10 as a function of time. Taking the value $\Delta Q_f/\Delta Q_0 = 0.12$ at 3 s from Fig. 3.10 together with $\Delta T = 0.35$ K, the Biot number can be estimated, using eq.(3.2), as $Bi = 0.008$ justifying the assumption of Sec. 3.1.1.

$\Delta Q_f/\Delta Q_0$ in Fig. 3.10 increases rapidly during both the magnetization and demagnetization process. It reaches a maximum between 3 and 4 seconds, i.e. at a time when the heat flux has already dropped. The maximum is followed by a decrease which is caused only to a minor extent by the heat losses through the surrounding air. The major contribution stems from the loss of an accurate reference point of known unwrapped phase, hence known $\Delta T = 0$ K, beyond $t \geq 5$ s. As discussed in Sec. 2.1.1, a reference point of this kind is needed to calibrate the interferometry data in case of weak vibrations. Although there is only a minor overall decrease in the magnitude of T(x) if the data is not calibrated, this effect is raised by the integration and therefore the main cause for the decrease of $\Delta Q_f/\Delta Q_0$ in Fig. 3.10.

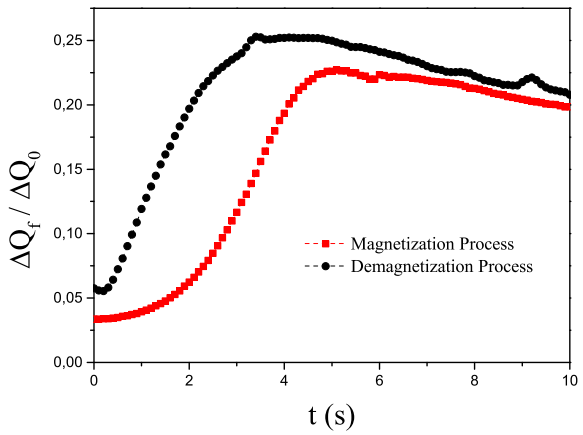

Fig. 3.10 The thermal energy, ΔQ_f, transferred into n-decane divided by the entire thermal energy ΔQ_0 generated in the Gd plate during magnetization and demagnetization, respectively.

3.1.6 Summary

The heat exchange between parallel gadolinium plates, with an 8.4 mm space in between, and n-decane in a 350 mT homogeneous magnetic field was monitored at the fluid side using a

Mach-Zehnder interferometer (MZI). The corresponding temperature measurements directly at the surfaces of the Gd plates were conducted using thermocouples. A simplified 1-D finite volume based simulation was used for selecting n-decane as heat transfer fluid which allows a sufficiently high temperature increase measurable for the MZI. Space- and time-resolved temperature data are obtained with this setup and algorithm for interferogram processing and extrapolation.

The effect of a finite time of mag- and demagnetization was clearly visible in the experiments. It results in a spatially delayed release of ΔQ_0 causing an additional and undesired temperature gradient inside the heat transfer fluid. Another important result is the overview over the complete temperature profiles during mag- and demagnetization along the centerline normal to the Gd plates which is largely unaffected by the finite speed of magnet motion. The temperature gradient derived at fluid side shows a significant drop down during the first three seconds. As a result, the heat flux is reduced by about 80% during de- and magnetization process in this time span. The energy exchange between Gd and n-decane reaches approx. 25% after 5 s.

An increase in the operating frequency is a crucial question in order to achieve acceptable cooling powers with limited (as expensive) MCM material quantities. One of the key points to be solved on this way is the minimization of losses due to the heat transfer between the refrigerant and heat transfer fluid. Although the present work focuses on stagnant fluid without natural or forced convection - in contrast to any beneficial machine - the visual insights into the dynamics of diffusive heat transfer are useful for a basic understanding of the heat transfer in an AMR.

3.2 Heat transfer enhancement in magnetic cooling using MHD convection

3.2.1 Experimental setup

Gd plate, same as what is used in Sec. 3.1, was glued to one side of a cuboid quartz glass cuvette with an inner side length of 10 mm as shown in Fig. 3.11b. Two NdFeB permanent magnets were combined to form an inhomogeneous magnetic field to generate the MHD flow and to trigger the magnetocaloric effect of the Gd plate. For this purpose, the two rectangular block magnets ($50 \times 30 \times 12$ mm^3) were juxtaposed with opposite magnetization directions so that their smallest sides touched at the outer side of the glass cell at the middle of the Gd plate, cf. Fig. 3.11a. A 3D finite element method, cf. Sec. 2.2.1, is used to simulate the magnetic field with Ampere's law. The relative permeability of the permanent magnets is 1.07

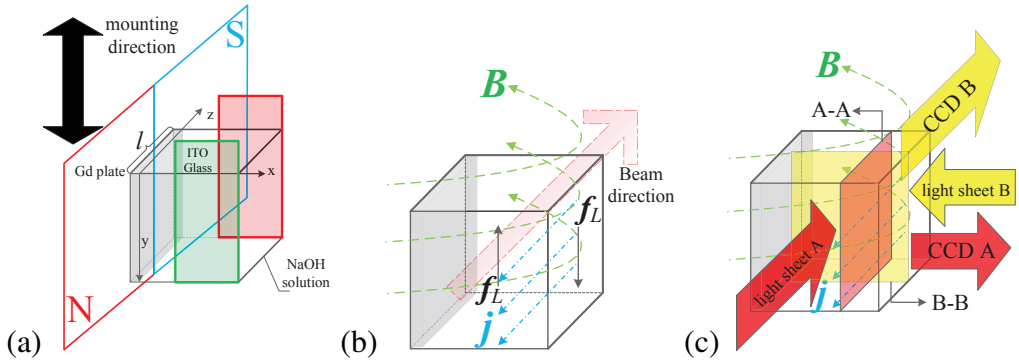

Fig. 3.11 (a) Schematic illustration of the experimental set-up and (b) of the position of the cell with respect to the laser beam of the Mach-Zehnder interferometer. Additionally, the orientation of magnetic induction, current and Lorentz force density is plotted in (b). In (c) the positions of the light sheets are shown to measure the primary flow in the A-A plane (light sheet A) and the secondary flow in the B-B-plane (light sheet B) by means of the particle image velocimetry.

and the remanence of the two magnets are regarded the same; both are B_r=0.7 T. Simulation results in Fig. 3.12 show the expected quasi 2D magnetic field distribution in the entire cell region. The simulated results are verified by directly measuring the magnetic flux density using a Gaussmeter (SYPRIS Test & Measurement Model 5180), cf. Fig. 3.12b. A fair agreement between the simulated and measured magnetic flux density is seen in Fig. 3.12c. The largest error, at around x=2 mm, is less than 20 %. It is mainly caused by the relatively large sensor size in comparison to the small cell size.

The magnet assembly just described was mounted on a 1D motorized linear translation stage which was moved with a speed of 10 mm/ s during the magnetization and demagnetization phases. In the present $\vec{B}$ setup the magnetization of the Gd plate, nearly parallel in the center of the cell while perpendicular in the outer parts, is not optimum from the viewpoint of the magnetocaloric effect, see [28, 65] and Sec. 1.1.1. However, for the present purpose, it is an acceptable compromise since this measurements with MHD convection can be referred to a reference case without MHD convection, which is also exposed to exactly the same $\vec{B}$ configuration. To inject the electric current required to generate the MHD convection, two transparent electrodes, made of indium-tin oxide (ITO) glass, are placed on opposite sides of the cell along the beam direction, cf. Fig. 3.11a-b. As an electrolyte, which also acts as a heat transfer fluid, a 0.5 M NaOH solution is chosen. The electrodes are connected to an electrochemical workstation (CHI 660C) by means of which a fixed direct current I into the solution for 5 s after the magnetization is charged. The potential and current distribution inside this setup are simulated using COMSOL fed with values of the electric conductivity of the three materials. All other walls are considered to be electric insulating. The electric

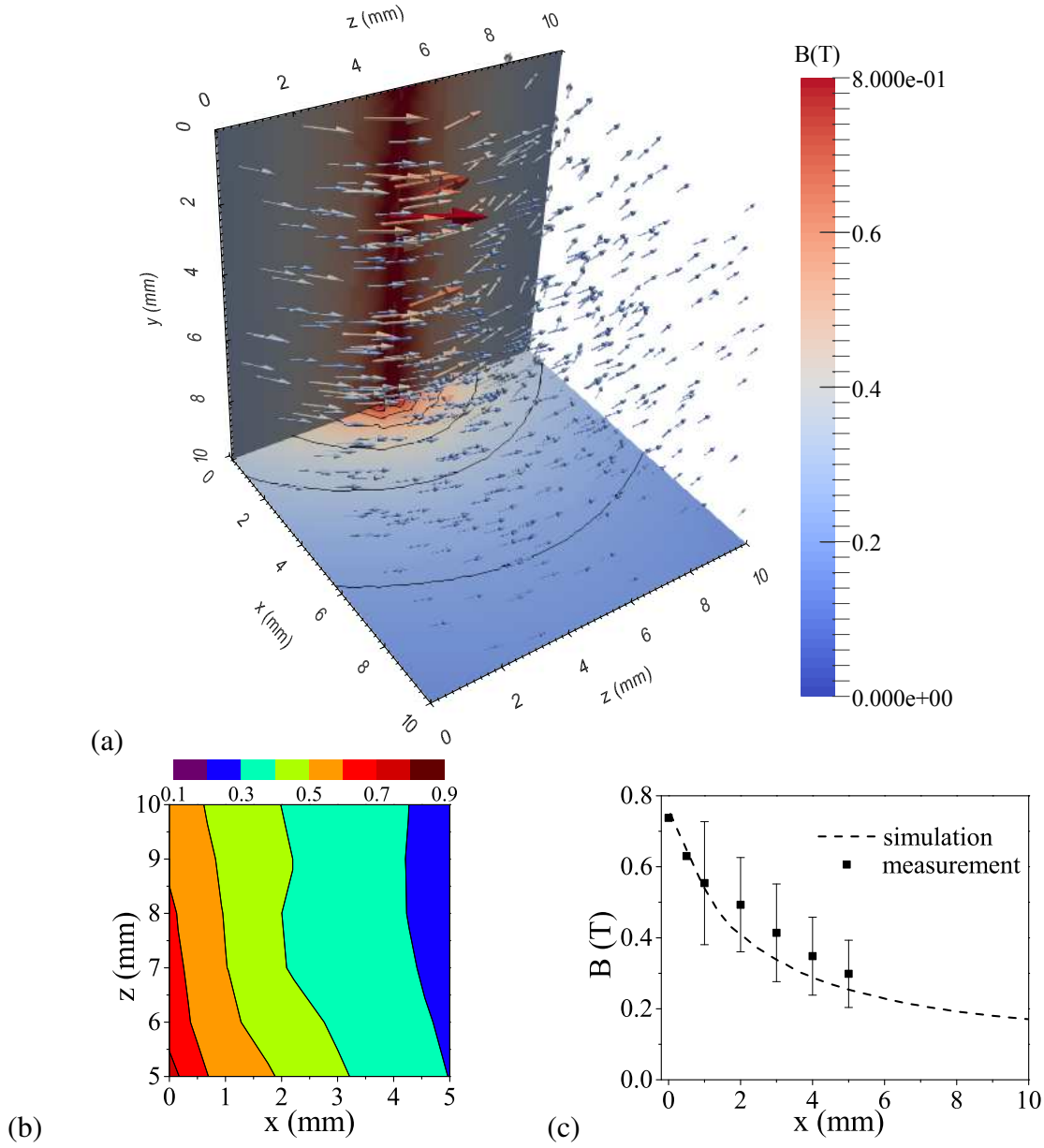

Fig. 3.12 Magnetic flux density distribution of the NdFeB magnet ensemble shown in Fig. 3.11: (a) simulation and (b) measurement with a spatial resolution of 1 mm. In the interval $0 \leq x \leq 1$, the resolution was increased to 0.5 mm. The arrows in (a) refer to the vector of magnetic induction and indicate a 2D distribution in the area of the glass cell. The contour line in the x-z plane in (b) shows the measured magnetic flux density from 0 to 0.8 T with a step of 0.1 T. This subfigure maps a topview of (a) which validates the numerically determined $\vec{B}$ in the front part of the cell where $z \leq \frac{l}{2}$, cf. Fig. 3.11b. (c) Comparison between (a) and (b) along the centerline at $y = z = 5$ mm.

potential and current distribution is plotted non-dimensionlized form in see. Fig. 3.13. As

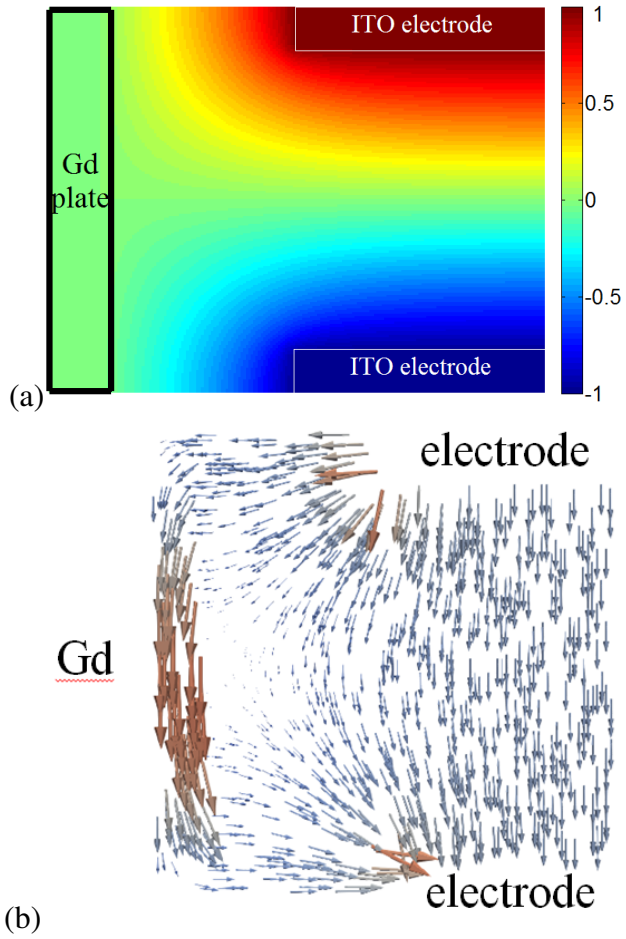

Fig. 3.13 (a) Non-dimensional potential distribution with external applied potential drop between two ITO electrode and (b) non-dimensional electric current distribution inside the setup shown in Fig. 3.11.

has been mentioned already in Sec. 3.1, this alkaline solution, turned out to be the optimum liquid for this purpose. It is nearly corrosion-free and possesses a sufficiently high electric conductivity (approx. 9.3 S/ m) to accommodate magnetohydrodynamic convection([131]). The velocity field of the MHD convection inside the heat transfer fluid is measured by means of particle image velocimetry (PIV), as illustrated in Fig. 3.11c and Sec. 2.1.2.

The analysis of the heat transfer with and without convection is based on the temperature field measured by the Mach-Zehnder interferometer in which the cuboid glass cell was placed ([65]), see Fig. 3.11b. Great care was taken to avoid any superposition between heat and mass transfer resulting from a weak dissolution of the tin-oxide layer at the ITO electrode, which occurs at higher currents $I \geq 5$ mA and longer operation times $t > 5$ s. In the latter case, a concentration perturbation is slowly advected by the MHD flow from the electrodes

towards the Gd plate. This perturbation is clearly identifiable in the refractive index field. Thus, calibration experiments were carried out in the same configuration as illustrated in Fig. 3.11 but without the Gd plate. From these experiments without the magnetocaloric effect, for each current a threshold value of the time was derived below which no observable effect of a mass transfer perturbation onto the temperature field exists. For the maximum electric current studied (9 mA), this time is 3.5 s. Based on this clear identification, the operation condition of the experiments can be adjusted such that any interference between heat and mass transfer is completely prevented. To guarantee this, only small currents, $I < 4$ mA, were used for quantitative energy evolution analysis, which will be shown in Sec. 3.2.3, although higher currents (e.g. 9 mA) were also studied. Furthermore, a delay of $\Delta t = 1.5 \pm 0.3$ s between magnetization and switching on the electric current was applied. Given the known MHD velocities, even tiny concentration perturbations have no chance to approach the Gd plate in the time window of interest.

3.2.2 Velocity field of the MHD convection

The MHD convection is driven by the Lorentz force density, $\vec{f}_L = \vec{j} \times \vec{B}$. The magnitude of the electric current density, $\vec{j}(\vec{r})$, is given by $|\vec{j}| = I/A_{ITO}$ where A_{ITO} refers to the area of the ITO glass. In the present configuration, $\vec{f}_L$ is mainly caused by the interaction of the z component of $\vec{j}$ and the x component of $\vec{B}$. In the rear part of the cell, for $l/2 < z \leq l$, $\vec{B}_x < 0$ while $\vec{B}_x > 0$ in the front part for $0 \leq z < l/2$, cf. Fig. 3.11b. Therefore, $\vec{f}_L$ points upwards in the front part and downwards, i.e. parallel to the positive y direction in the rear part (Fig. 3.11b). The resulting torques in the A-A plane in Fig. 3.11c set the fluid into a swirling motion between the ITO electrodes. In a meantime, the center of the A-A plane is imagined as the origin of a cylindrical coordinate system. If the swirling flow now circulates around this center, it causes a radial pressure gradient. As a result, a secondary flow sets in. Under ideal conditions and the presence of a cylindrical geometry this secondary flow would have the shape of a torus, the axis of which emerges in the center of the A-A plane, parallel to the x-axis. At this center axis, the secondary flow is directed away from the Gd plate. By contrast, in the outer parts of the toroidal-like vortex, the flow is towards the Gd plate. Since the engine of the primary flow is between the ITO electrodes, shear forces, together with the secondary flow, are responsible for setting the remaining electrolyte volume between the ITO electrodes and the Gd plate into motion.

To measure the velocity field of the primary flow by PIV, a light sheet is placed in the A-A plane between the two ITO glasses, see Fig. 3.11c. Fig. 3.14a clearly shows the swirling motion discussed before. To determine the secondary flow, PIV experiments are also conducted by placing the light sheet in the B-B plane. Fig. 3.14b shows a double vortex

structure which is the expression of the toroidal-like secondary flow anticipated above. The reasons for the non-perfect symmetry are seen in the difference of the velocity boundary condition at the solid bottom (no-slip) and the free surface (free slip) as well as in the cuboid geometry of the cell. Since the secondary flow is typically by a factor of 5...10 smaller than the primary flow ([138]), the experiments of Fig. 3.14b required a higher current (I=5 mA). This fact is also resolved in Fig. 3.14c, which shows the flow in a plane parallel to the B-B plane but shifted by $\Delta z = 2$ mm. Due to this shift, the superposition of the primary and secondary flow becomes visible. At the outer parts, the flow towards the Gd place is visible. However, in the central parts, the downflow dominates, which results from the stronger primary flow.

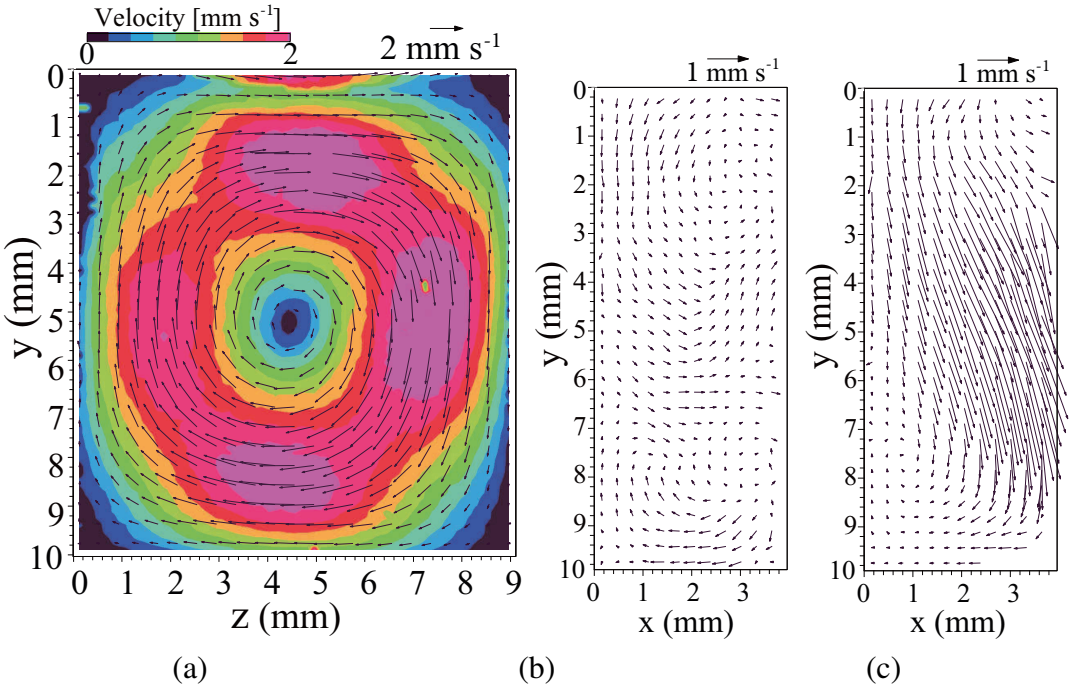

Fig. 3.14 PIV measurements of velocity field: fully developed primary flow in the A-A plane (I= 2 mA) (a) and secondary flow in the B-B plane at 9 mA (b) and at 5 mA in a plane parallel to the B-B plane but shifted by 2 mm along z direction in (c). The location of the planes is explained in Fig. 3.11c. For better visibility of the small secondary flow in (b-c) only the arrows without color map as in (a) are given.

After the global structure of the model flow used to demonstrate the heat transfer enhancement is clarified, we next take a closer look at the primary flow in Fig. 3.14a. Due to the no-slip boundary condition at the sidewalls of the cell, the velocity is zero in this region. In the center, the fluid is stagnant since the Lorentz force is zero there. Between the center of the A-A plane and the glass walls the velocity magnitude reaches a maximum. As a characteristic velocity of the primary flow, the area-averaged velocity $v_c(I)$ is taken([139]).

For the latter, $v_c\,(I = 1\text{mA})$ = (0.48 ± 0.02) mm/ s and $v_c\,(I = 2\text{mA})$ =(1 ± 0.02) mm/ s are obtained. Based on this, the Reynolds number is calculated via $Re(I) = \rho v_c L_c/\mu$ where the density $\rho = 1.019$ g/cm^3 and viscocity $\mu = 0.9715$ mPa$\cdot$s is taken from [117] and the characteristic length L_c is chosen as 10 mm, which is the inner geometry of the cell. For I=2 mA, $Re\,(I = 2mA)$ = 10.5, it clearly indicate a laminar flow. Because of a nearly linear relationship between the average velocity and the electric current ([68]), the v_c's obtained for lower currents could be used to extrapolate to those at higher I. According to that, the characteristic velocity at I=9 mA is estimated as $v_c(I = 9\text{ mA})$ = 4.5 mm/ s.

3.2.3 Temperature field and heat transfer

Magnetization stage

The 2D space resolved temperature field of the thermal boundary layer within 3 mm to Gd plate, measured by the MZI, is plotted in Figs. 3.15 and 3.17 with and without current injection, respectively. The isotherms, ranging from 0 K to 0.3 K with a step of 0.03 K, map the temperature field in the aqueous solution due to the magnetization of the Gd plate. The field of view comprises the region $(0 \leq x \leq 3$ mm$) \times (3 \leq y \leq 7$ mm). It is the roughly central band perpendicular to the Gd plate in the thermal boundary layer of the liquid phase. For the pure heat conduction, i.e. I=0 mA, shown in Fig. 3.15, the heat transfer is more or less 1D. Compared to Sec. 3.1, this was achieved by raising the speed of the magnets (10 mm/ s). Natural convection is negligible as proved by the minor distortion of the isotherms, i.e. the thermal propagation is indeed iso-conduction. The propagation speed of thermal front slows down with progressing time, e.g. compare the images at 3.5 s and 4.5 s, as there is less heat flux into the liquid. In parallel, the temperature gradient becomes flatter; refer to Sec. 3.1 for details .

By computing the entire interferogram stack belonging to Fig. 3.15, using the algorithm in Sec. 2.1.1 and 2.1.1, space- and time- resolved temperature profiles are obtained, see Fig. 3.16. These profiles were obtained by averaging temperature profiles in a narrow band between 4.95 mm $< y <$ 5.05 mm along the y coordinate, followed by an arithmetic mean of three independent experiments. Growth in the thermal boundary layer in the alkaline solution accompanied by a decrease in the temperature gradient is clearly visible.

By contrast, in the presence of the MHD convection the heat transfer process is clearly altered, see Fig. 3.17. Before detailing the changes, it is important to recall a delay of around 1.5 $\pm$ 0.3 s after magnetizing the Gd plate and injecting the electric current have been incorporated for reasons explained in Sec. 3.2.1. Accordingly, the thermal front can already propagate into the NaOH solution by approx. 1 mm, cf. Fig. 3.16, before the MHD

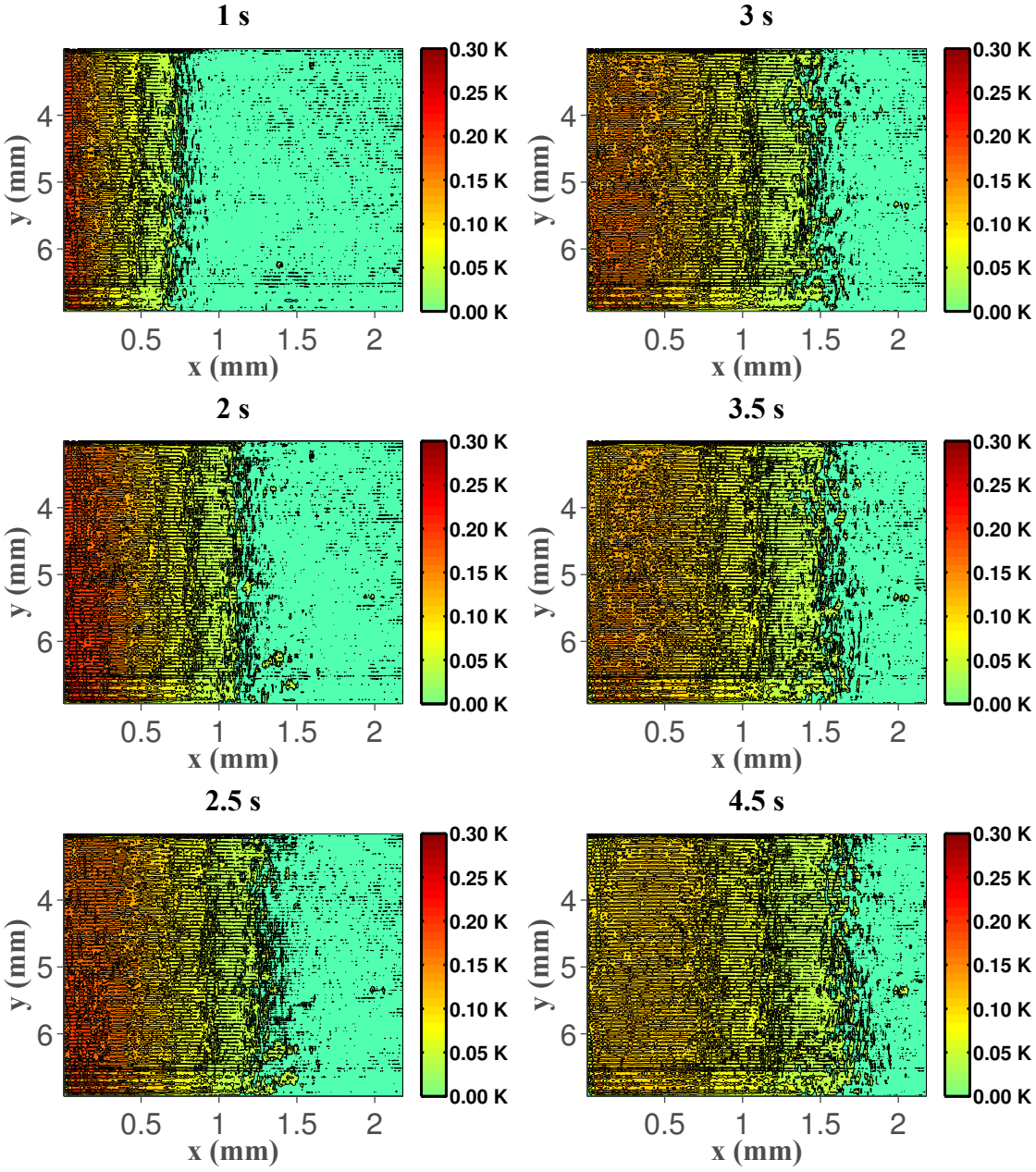

Fig. 3.15 2D space- and time-resolved temperature field in 0.5 M NaOH solution during magnetization of Gd plate with a vanishing electric current $I = 0$ mA, i.e. pure heat conduction which constitutes the reference case. The vertical boundary $x = 0$ along the y axis represents the solid-liquid interface, i.e. the Gd plate is placed immediately at the left vertical margin of each subfigure.

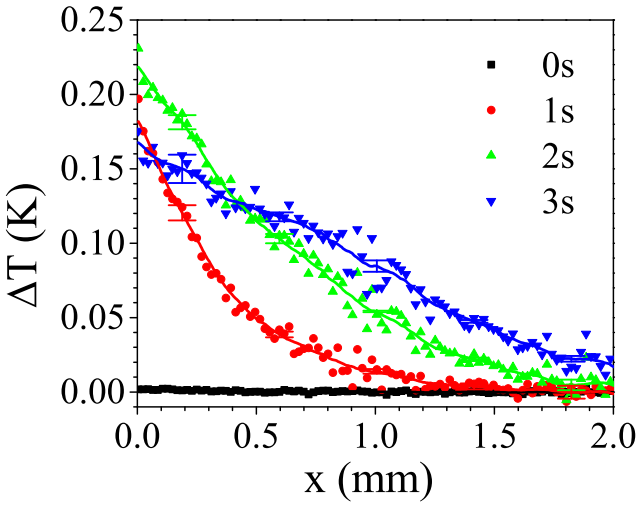

Fig. 3.16 Temperature profiles obtained from the temperature field of Fig. 3.15. They map the evolution of the thermal boundary layer in a 0.5 M NaOH solution during the magnetization stage. Discrete points are the raw data directly gained after interferogram processing. For better visibility, only every fifth point is plotted. The solid lines are obtained after applying the postprocessing algorithm, described in Sec. 2.1.1, to the raw data.

convection starts. Depending on the velocity amplitude, determined by the magnitude of the electric current injected, it takes a further 1 s to 2.5 s before the MHD convection becomes visible in the field of view of the interferometer. Note, however, that this timespan is caused by the specific conditions of this setup used to demonstrate the proof-of-principle. In a practical application, the delay time can be set to zero, resulting in the MHD flow having a more intense impact. The shape of the deformation of the isotherms in Fig. 3.17 is correlated with the shape of the secondary flow as shown in Fig. 3.14b. The region (3 mm $\leq y \leq$ 7 mm) x (1.5 mm $\leq x \leq$ 3 mm), where the bending of the isotherms is most pronounced, is dominated by a flow away from the Gd plate which turns upwards for larger x-values under the influence of the upper secondary vortex in Fig. 3.14b. The degree of the deformation becomes stronger the higher the current, in parallel with an earlier onset. As a result of this heat advection, the temperature gradient along x direction becomes smaller when convective heat transfer takes place.

Since the behavior in Fig. 3.17 is no longer 1D as in Fig. 3.15, the evolution of the temperature field in terms of the thermal energy transferred into the 0.5 M NaOH solution for different electric currents during the magnetization process is then analyzed. The thermal energy is obtained by integrating over the temperature field $\Delta T_f(x,y,t,I)$, measured by the

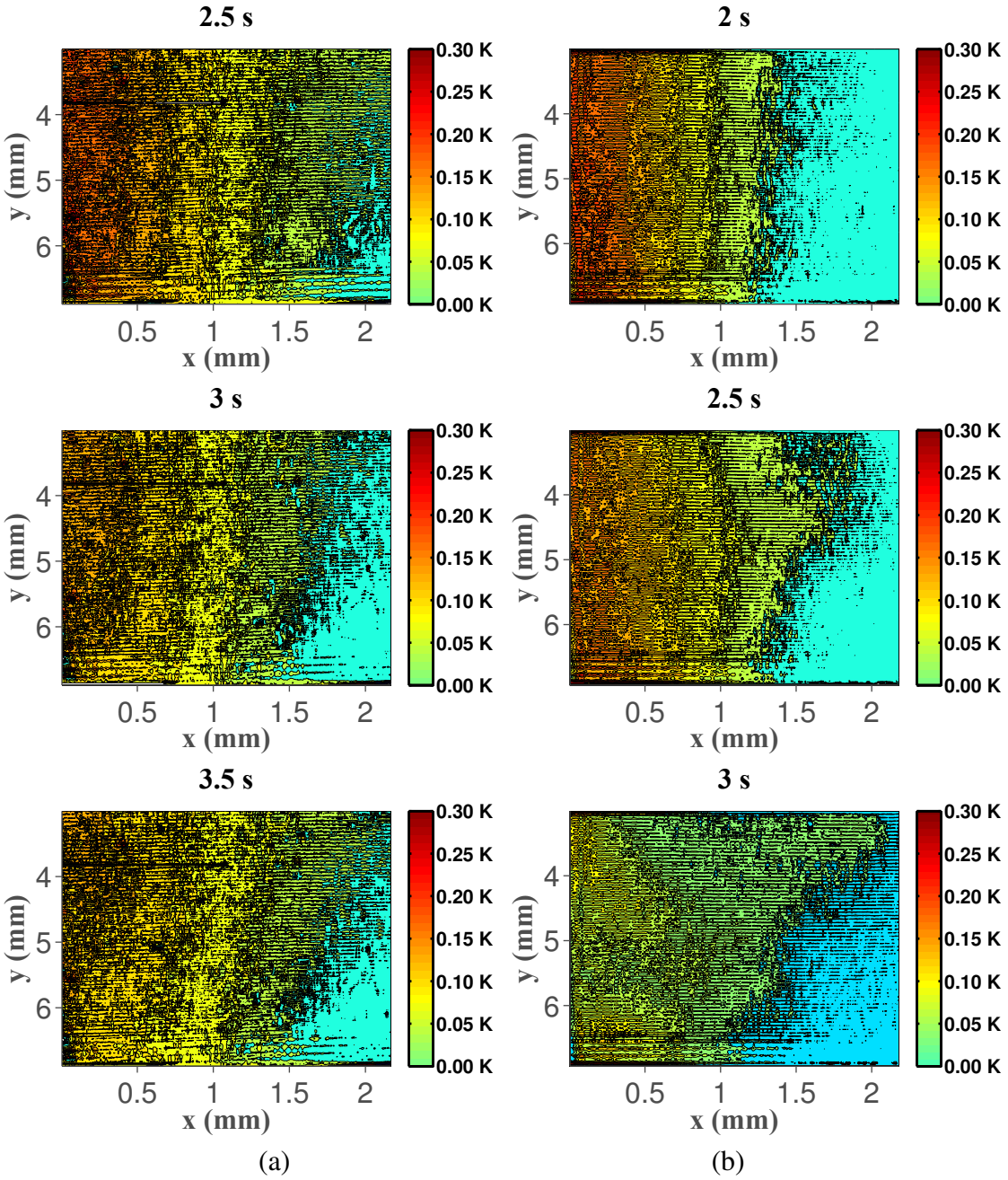

Fig. 3.17 2D temperature field at 2 s, 2.5 s and 3 s after magnetization of Gd plate in the presence of MHD convection with $I = 3$ mA (a) and $I = 9$ mA (b) in the heat transfer fluid 0.5 M NaOH. The vertical boundary $x = 0$ along the y axis represents the solid-liquid interface, i.e. the Gd plate is placed immediately at the left vertical margin of each subfigure.

MZI

$$\Delta Q_f(t,I) = \int_{y=min}^{y=y_{max}} \int_{x=0}^{x=x_{max}} C_{p,f}\rho_f V_f(x,y)\Delta T_f(x,y,t,I)dxdy, \tag{3.11}$$

where $C_{p,f} = 4.023 \times 10^3J/kg\cdot$K ([118]) is the specific heat capacity and $\rho_f = 1.019 \times 10^3$kg/m^3 of the 0.5 M NaOH. Each curve in Fig. 3.18 is calculated with a time step of 0.1 s as the arithmetic mean of three independent experiments. For the latter, only electric currents between 0 mA to 3 mA as explained before are included. It is reasonable to restrict the energy analysis to the time window of 5 sec to prevent the thermal front from propagating over the measurement boundary of the interferometer. For the purely diffusive case, I=0 mA, ΔQ_f increases from zero at 0 s due to the temperature rise in the solid and the transient heat transfer into the liquid phase. The small slope at the very beginning is due to the imperfect parallelization of the Gd plate with the measurement beam of the MZI, see Sec. 3.1; an effect which becomes soon negligible. After this short interval, the energy exchange speed is maximum during 0.2 s ... 1.5 s. Then, the slope decreases and the thermal energy approaches a plateau. ΔQ_f remains on the plateau as long as the thermal front remains in the field of view of the interferometer, i.e. until about $t \sim 5$ s.

In the presence of the MHD convection, a higher ΔQ_f transferred into the alkaline solution is resulted in a higher the electric current. Also, the transfer proceeds more quickly, as seen in particular for the 3 mA curve. The reason for the higher standard deviation in the case of MHD convection is the averaging over three independent experiments which slightly differ in the velocity field, e.g. due to small differences in the delay time.

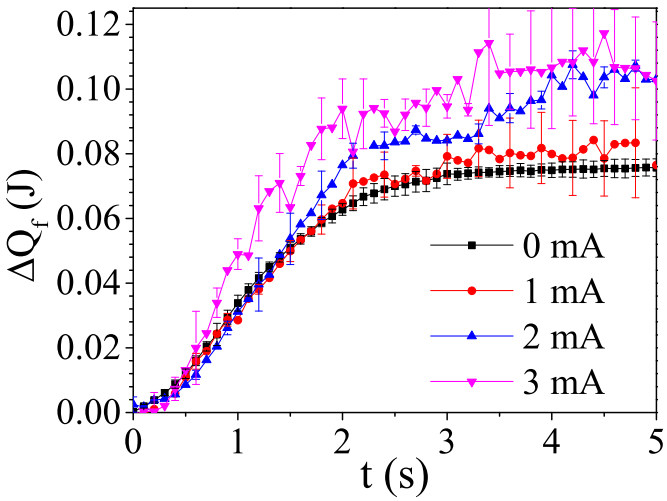

Fig. 3.18 Measured evolution of thermal energy, ΔQ_f, transferred into the 0.5 M NaOH solution versus time during the magnetization phase at different levels of MHD convection expressed by the electric current I.

To quantify the increased heat transfer, the enhancement factor is defined

$$E_{enh}(t,I) = \frac{\Delta Q_f(t,I) - \Delta Q_f(t,I = 0\ \text{mA})}{\Delta Q_f(t,I = 0\ \text{mA})} \tag{3.12}$$

which is the difference between the thermal energy transferred into the aqueous phase between nonzero current and I=0 mA, referred to the case of pure heat conduction (I=0 mA). $E_{enh}(t,I)$ is plotted versus time in Fig. 3.19a. A notable increase with increasing current is clearly visible. By averaging $E_{enh}(t,I)$ in 2 s $\leq t \leq$ 5 s, a more or less linear relationship for

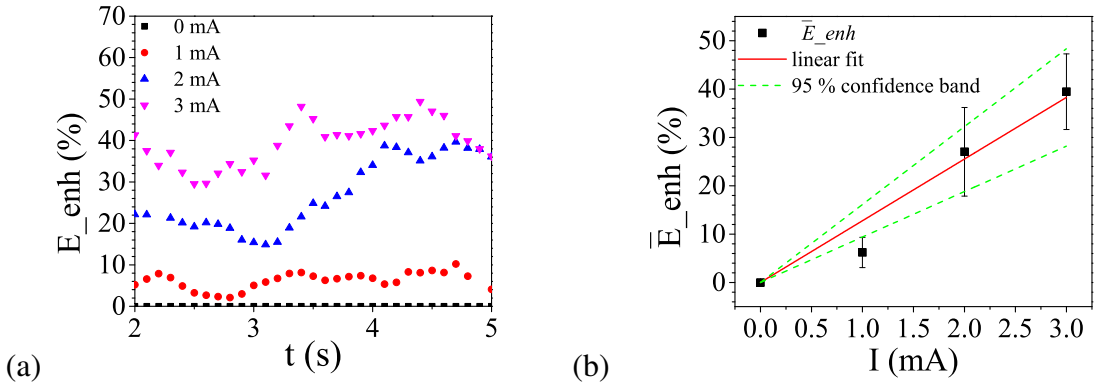

Fig. 3.19 (a) Enhancement factor E_{enh} versus time for different currents. (b) Averaged enhancement factor $\overline{E}_{enh}$ as a function of the electric current together with the linear fit, $\overline{E}_{enh} = 12.76\ mA^{-1} \cdot I$.

the mean enhancement factor, $\overline{E}_{enh}$, as a function of the electric current, see Fig. 3.19b is obtained. It shows that an enhancement of the heat transfer by about 40 % can be achieved even with a small current of 3 mA.

Demagnetization stage

Generally, the demagnetization stage is less suitable to achieve an enhancement of the heat transfer by the MHD flow compared to the magnetization stage. The reason is the following. While the MCE is triggered by a decreasing magnetic field, the MHD flow gradually loses momentum due to the exclusion of the magnetic field. Nevertheless, even pulse-like MHD convection, triggered in the 1s removal time of the magnet in the demagnetization stage, is sufficient to provide a visible impact on the temperature field. The left column in Fig. 3.20 shows the reference case, pure conductive heat transfer, I=0 mA. Note that the Gd plate is demagnetized from bottom to top since the magnets move upwards in this configuration. This is the reason why the isotherms are slightly more advanced at the bottom. The impact of the

MHD convection follows a similar pattern compared to the magnetization process, but there are three differences. (i) The temperature change is now negative. (ii) The delay time is set to zero, i.e. when the magnet start to move, the electric current is injected, leading the MHD flow to start at 0 s. (iii) Due to the progressive exclusion of the magnetic field from the lower to the top parts of the heat transfer fluid, the region of MHD convection is vertically narrowed by dynamically lifting the lower boundary upwards. As a result, the "pivot" of secondary flow is also lifted upwards. This continuous process induces a sequential enhancement of heat transfer from the bottom up. For the sake of demonstration a higher current of I= 9 mA was chosen. The contour line of the thermal front in Fig. 3.20b is propagated further in the lower part. Later, the heat transfer is followed by what is more or less heat conduction due to the exclusion of the magnetic field.

3.2.4 Summary

As the magnetic field $\vec{B}$ is an intrinsic component in any magnetic cooling device, magneto-hydrodynamic (MHD) convection appears an interesting concept to enhance heat transfer. To create MHD convection in the aqueous-based electrically conducting heat transfer fluid, an electric current has to be injected. This current interacts with $\vec{B}$ to give rise to a Lorentz force which stirs the fluid, thereby enabling a higher heat transfer.

To deliver a proof-of-principle for the MHD convection concept, a thin gadolinium plate was placed in a transparent cuboid glass cell filled with the heat transfer fluid. For the latter an alkaline solution (0.5 M NaOH) was used which provides sufficient electric conductivity with vanishing corrosion of MCM. Two permanent magnets were combined to form a more or less 2D magnetic field to trigger both the MCE and the MHD convection. The resulting magnetic field was simulated by means of a 3D finite element solver and compared with measurements using a Gaussmeter. Electric currents ranging from 1 mA to 9 mA were injected into the NaOH solution using transparent ITO glass electrodes. In this particular electrode-magnet arrangement, a primary swirling flow sets in, rotating in planes parallel to the gadolinium plate. It is accompanied by a weaker secondary flow which is directed toward the Gd plate at the rim and away from the Gd plate at its center. The MHD convection was measured by means of PIV. The characteristic velocity has an order of magnitude of 1 mm/ s and increases linearly with the electric current. By applying a Mach-Zehnder interferometer, space- and time-resolved temperature data were obtained during the magnetization and demagnetization of Gd. To quantify the differences in the heat transfer with and without MHD convection, an enhancement factor, E_{enh}, cf. Eq.(3.12), was calculated. This factor, which reflects the difference in thermal energy transferred into the heat transfer fluid with and without MHD convection, was found to increase more or less linearly with the electric current. Even small

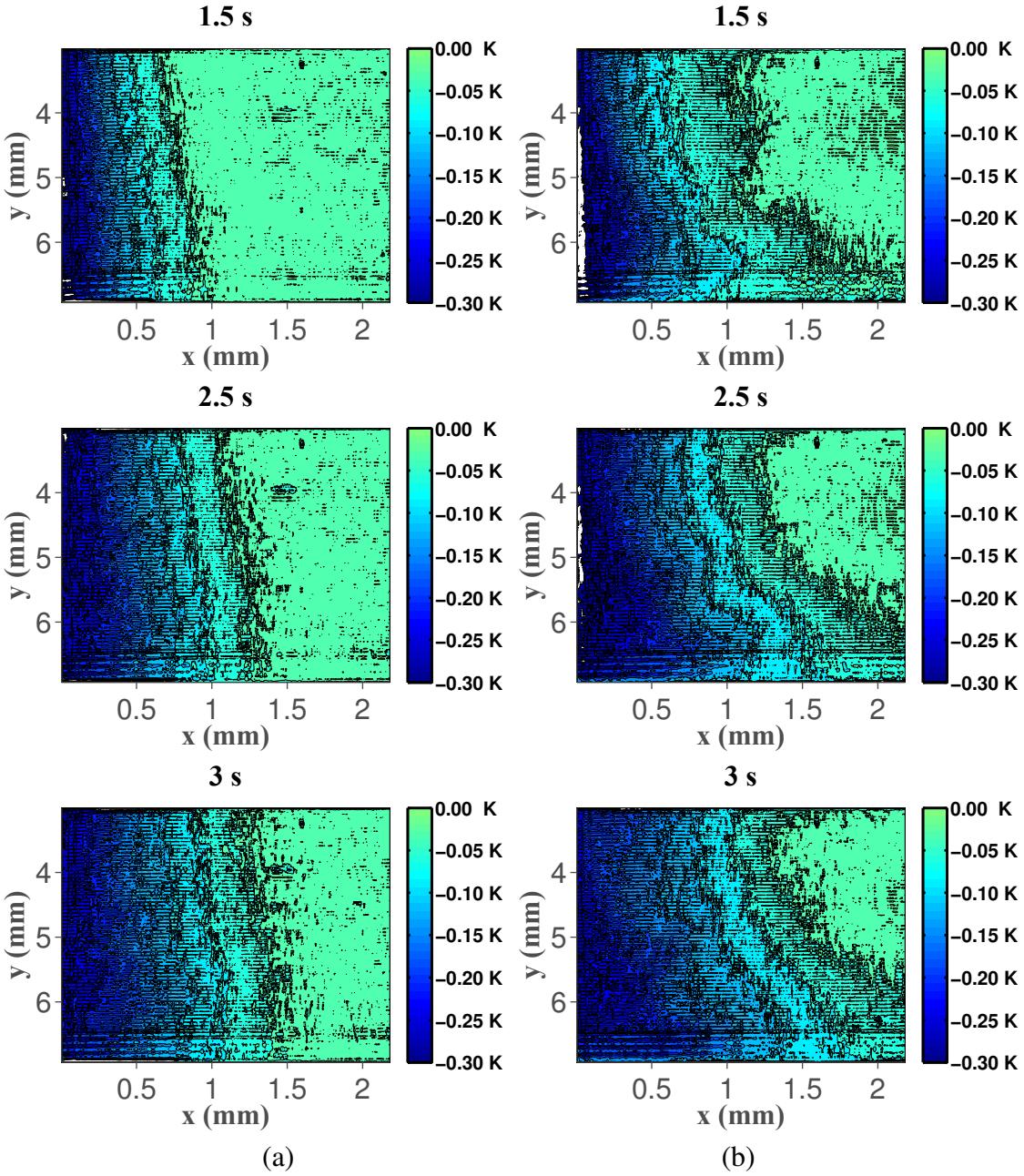

Fig. 3.20 2-D temperature field at 1.5 s, 2.5 s and 3 s after demagnetization of the Gd plate with $I = 0$ mA (a) and $I = 9$ mA (b) in the heat transfer fluid 0.5 M NaOH. The vertical boundary $x = 0$ along y axis represents the solid-liquid interface, i.e. the Gd plate is placed immediately at the left vertical margin of each subfigure.

currents of 3 mA give rise to a significant heat transfer enhancement of about 40 % by means of a MHD flow. Furthermore, the results demonstrate that it is feasible to enhance the heat transfer with MHD convection even in the demagnetization phase although to a weaker extent compared to the magnetization stage.

Based on these encouraging results, the MHD convective heat transfer concept appears to be worth testing further in real AMRs. To create efficient MHD convection, the Lorentz force density $\vec{f}_L$ should be rotational, i.e. $\nabla \times \vec{f}_L \neq 0$. This can be achieved e.g. by imposing an inhomogeneous current density $\vec{j}$ in the presence of a homogeneous $\vec{B}$. Let us consider for a moment a Halbach cylinder used to generate the favorable in-plane magnetization of the MC plate material. One option to incorporate the required electric field could consist in integrating pairs of small copper electrodes of a similar height as the MCM plate at different places in the AMR stack. If the opposing electrodes have a different cross section, an inhomogeneous current density is assured. As a result, a Lorentz force perpendicular to the direction of the forced flow through the AMR appears; this is stronger at the electrode with a smaller cross section, thereby stirring the alkaline fluid additionally in a spanwise direction.

3.3 Liquid metal based magnetic cooling

Gadolinium of the same supplier was machined after the same polishing procedure to a flat plate with an area of 50×10 mm^2 and a thickness of 0.8 mm. Two plates was embedded inside a plexiglass channel parallel to x-y plane. They locate in the middle of the channel as the upper and lower boundary. The remaining parts are plexiglass and with careful machining, a homogeneous cross section is guaranteed inside the channel with a total length of 110 mm, as shown in Fig. 3.21.

Instead of an aqueous based heat transfer fluid, the plexiglass channel is now filled with a liquid metal for which Galinstan (GaInSn) is used. Material properties of GaInSn are collected in Table 2.2. Galinstan is pumped through the channel by means of a peristaltic pump, see Fig.3.22. The components crossed by the green dashed line illustrate the mode for injecting the fluid into the system. By opening the valve 1 and 5 and turning on injection pump, the GaInSn is safely filled into the system without threat to leak outside the fluid tank. Then, by closing the valve 1 and 5 while the others left open, an internal flow system is formed by turning on the pump circled by black dashed line. The channel is made of plexiglass with a refined machining to guarantee acoustic quality and geometric accuracy. The geometry is designed with a supporting numerical simulation by means of COMSOL, see Sec. 2.2.1. A homogeneous flow of 50 mm/s is given as boundary condition at inlet

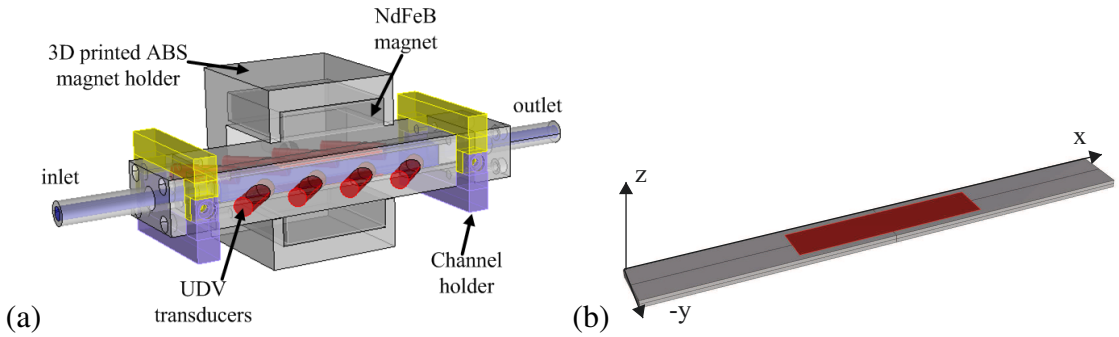

Fig. 3.21 (a) Schematic illustration of the experimental channel with a cross sectional area of 10 $\times$ 10 mm. The red cylinder represent the positions where the UDV transducer are mounted with an angle of 45 degree with respect to x direction. 8 UDV transducers can be used in total where the remaining 4 are located at the back side of the channel. (b) Position of the Gd plate in the top wall.

and outlet with uniform background pressure. The inlet and outlet has a diameter of 6 mm with a diffuser uniformly expanded to 8 mm over a length of 20 mm making an expansion angle around 3^o. Length of the measurement channel is chosen so that the measurement region is located in a quasi-developed flow region. Small expanding and converging angle, $\approx 10^o$, for diffusor is maintained. Nevertheless, recirculating vortex due to sudden change in cross section at the entrance and exit part of the main channel connecting diffusor is formed. Although it is not fully developed 2D Poisson flow, region where Gd plates is located and main measurement is conducted is free of such vortex.

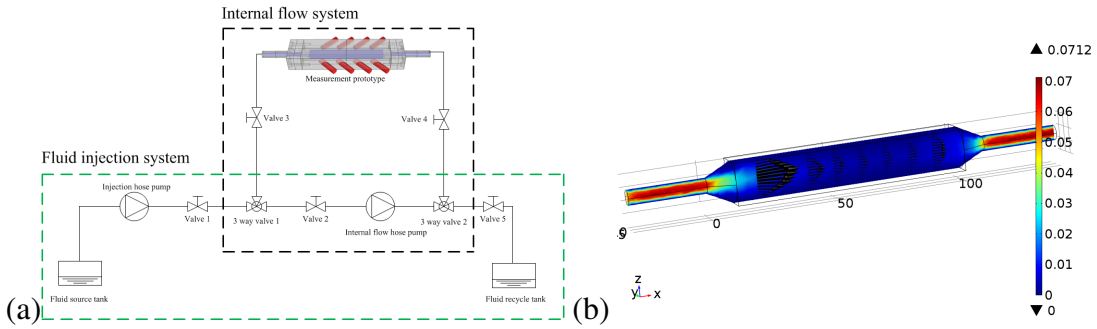

Fig. 3.22 (a) Schematic illustration of the components for injection mode (crossed in green) and experiment mode of the internal flow system(crossed in black) (b) 3D flow field simulated with COMSOL inside the duct as Fig. 3.21a.

Ultrasound doppler velocimetry (UDV) [140, 141] is used to measure the velocity distribution in the channel by means of ultrasound transducers. The transducers are attached to the channel under an angle of 45 degree with respect to x direction, see Fig. 3.21.

Two permanent magnetic (supermagnete) ($50 \times 50 \times 12.5$ mm^3) with N35 magnetization are arranged such that the biggest side faces each other with a gap of 30 mm in between. The two magnets were embedded into a 3D printed acrylonitrile butadiene styrene plastics holder; integrated with a computer programmed electric mounting stage moving with a speed of 30 mm/s along y direction, see Fig. 3.21 b. The magnetic field was simulated using a 3D finite element method together with Ampere's law, see Sec. 2.2.1. The simulation shows the expected quasi 2D magnetic field distribution in the entire flow region inside the duct, sketched by the blue volume in Fig. 3.23. A 220 mT quasi 1D homogeneous magnetic field anti-parallel to z direction is formed to trigger the magnetocaloric effect in the solid phase, and to generate the MHD flow at the adjacent liquid phase.

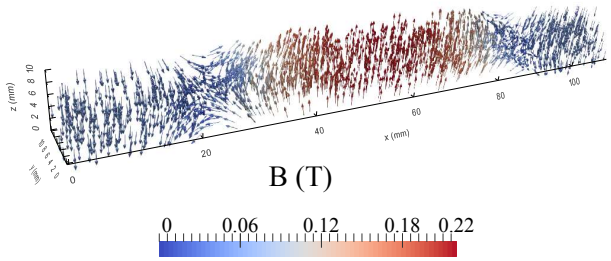

Fig. 3.23 Magnetic flux density distribution simulation of the NdFeB magnet ensemble used in Galinstan channel flow: Colorbar shows the magnitude and the arrows refer to the vector of magnetic flux density indicating a 3D distribution in the area of the main channel (cross section 10×10 mm^2) shown in Fig. 3.21a.

3.3.1 UDV result on velocity distribution with space- and time- inhomogeneous magnetic field

First result of the flow without a magnetic field are shown in Fig. 3.24a. The figure displays the profile of the x-component of the velocity, processed with two transducers located at opposite sides of the channel. The transducers used for this reconstruction are marked by A and B in Fig. 3.21a. The 45 degree orientation of the transducers with respect to the flow direction, preventing the echoes from the Galinstan-plexiglass boundary, is already taken into account. The data of the measurement region which is closer to the respective transducer, i.e. $y < 5$ mm for the transducer on the front side and $y > 5$ mm for the transducer on the back side of the channel (Fig. 3.21a), enter with a higher weight due to a higher signal to noise ratio in Fig. 3.24a.

For the case of vanishing magnetic field (Ha=0), Fig. 3.24a, the expected Poiseuille profile is recovered in analogy to the measurements conducted with NaOH solution, see Ref. [142]. Based on the mean velocity component in x direction (Fig. 3.24a), $Re = \frac{\rho v l}{\mu} \approx 1007$

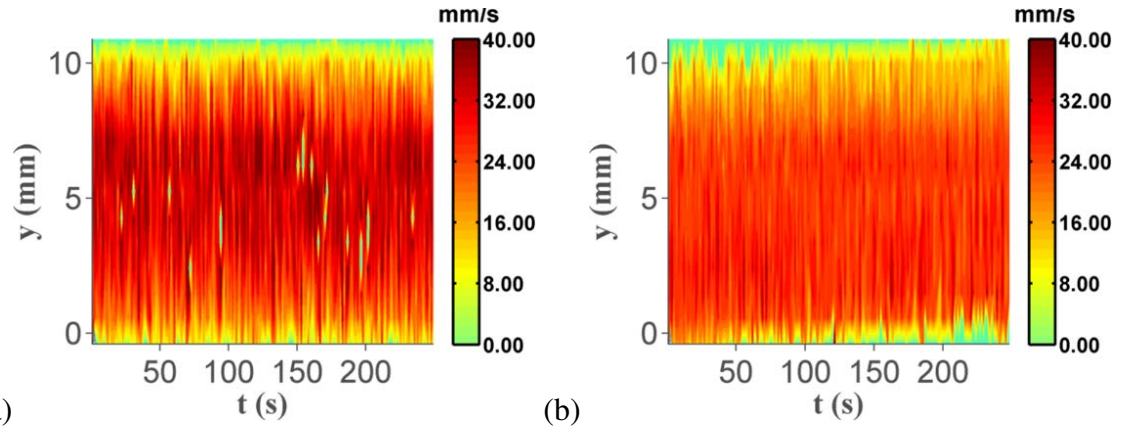

Fig. 3.24 Combined reconstructed velocity profile, measured with UDV transducers: (a) without magnetic field and (b) with a static magnetic field of approximately 220 mT shown in Fig. 3.12.

is obtained where $l = 0.01$ m is the characteristic length of the flow. Resulting Re with parameter concluded in Table. 2.2, a laminar flow regime is clearly indicated. In presence of the magnetic field, plotted in Fig. 3.12, the Hartmann number is $Ha = BL\sqrt{\frac{\sigma}{\rho\nu}} \approx 89$ where $L = l/2$ is the characteristic length and $\sigma = 3.1 \times 10^6$ S/m is the electric conductivity of Galinstan. The velocity distribution is more smooth compared to Ha=0 and shows a decrease in the maximum velocity. The velocity distribution agrees to the theoretical analyses and numerical simulations [143] of the flow between Shercliff walls, i.e. the walls parallel to magnetic field.

By averaging the velocity data over 250 s, the resulting mean velocity profile is plotted in Fig. 3.25. A good reproducibility between independent experiments exist and the no-slip boundary condition is clearly mapped by the UDV transducers. The decrease in maximum velocity magnitude for Ha=89 compared to the Poiseuille flow at Ha=0 amounts to about 20 %.

In comparison to conventional Hartmann flow which was comprehensively studied in the past, the present channel configuration presents several interesting features. It possesses a transitional region in which the liquid metal both enter the magnetic field and meets a boundary condition which changes from an electrically non-conducting wall to a wall of finite conductivity. Further experimental investigation on the velocity measurement and temperature measurement are needed.

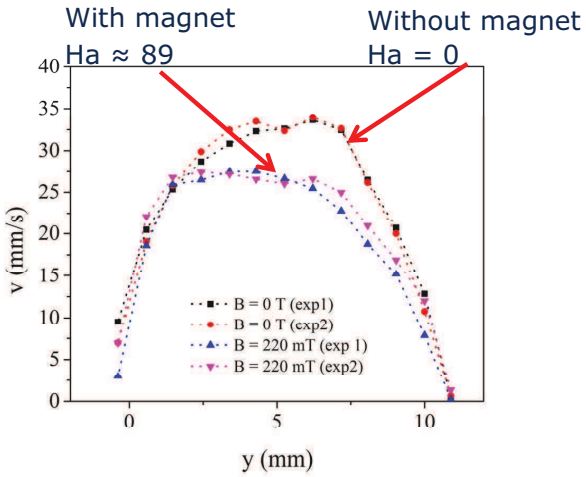

Fig. 3.25 Mean velocity profile obtained by averaging the velocity data over 250 s.

To give a brief account, the flow field which is altered by an static spatially inhomogeneous magnetic field is experimentally resolved. On the other hand, the periodically moving magnet introduces an another relative movement of liquid metal in magnetic field. Thus, the moving velocity is the same order of magnitude as the mean velocity of the GaInSn flow. This means the electric current generated by moving magnet should in principle comparable in its magnitude to the primary flow induced electric current. Taking a quasi-static condition, induced electric current density is simulated with algorithm presented in Sec. 2.2.1. The electric current field is presented in Fig. 3.26a with static magnetic field, cf. Fig. 3.23, and a fully developed poiseuille flow, cf. Fig. 2.7. While the second induced current is simulated when the magnet stray field is fully brought to the flow chamber with a transverse moving velocity 30 mm/ s, Fig 3.26b. We note that the induced current with a moving magnetic and static liquid metal is much bigger than the Hartmann flow case. Therefore, it is of importance to study also the influence of the moving magnet on the velocity profile of the liquid metal flow.

3.4 Chapter summary

This chapter reports results on a heat transfer process in a static heat transfer fluid. Interferometer is proved to be an accurate and powerful tool to resolve temperature field at the heat transfer fluid side. Then, a proof of principle is delivered on magnetohydrodynamic convection to enhancement heat transfer in a simplified regenerator bed without forced convection driven by pressure drop. Finally, a room temperature liquid metal GaInSn as alternative candidate as heat transfer fluid is tested. Ultrasound doppler velocimetry is

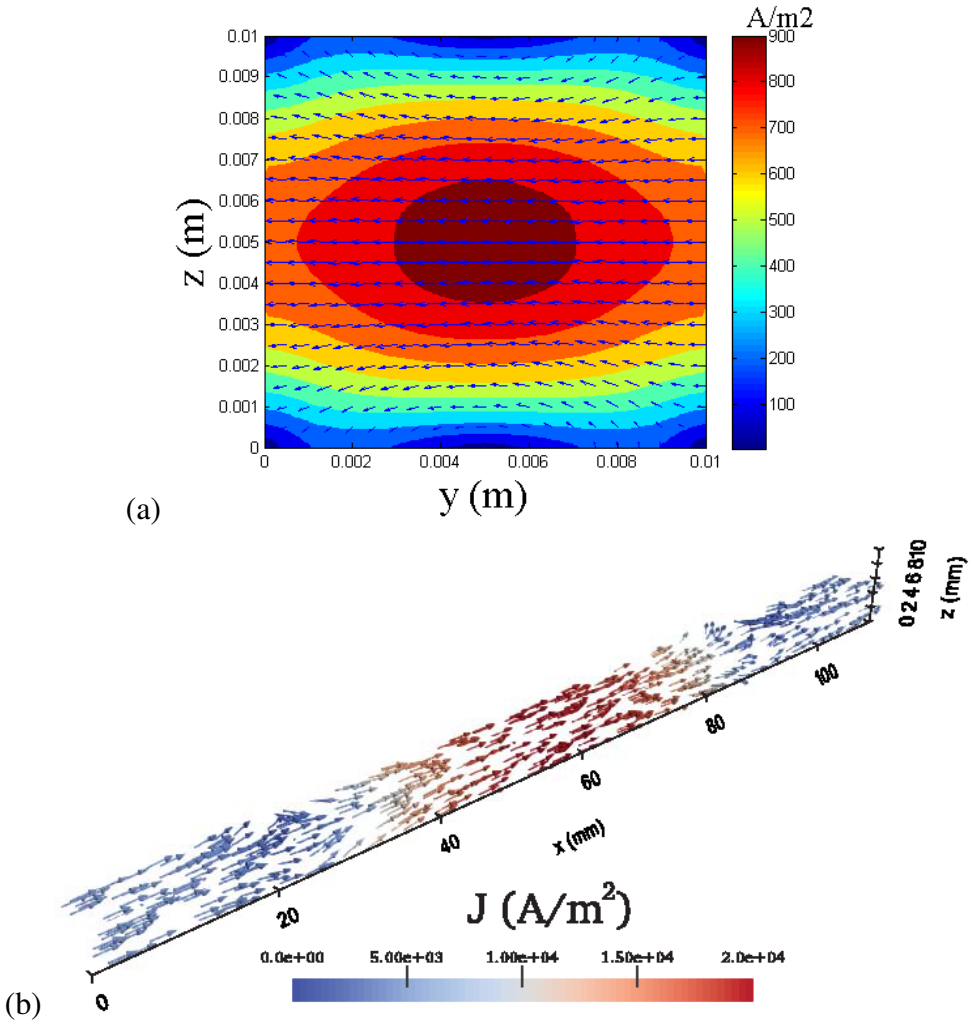

Fig. 3.26 (a) Current density simulation at cross section, y-z plane, with given fully developed 2D Poiseuille velocity distribution a static magnet field. (b) 3D current density simulation with a transverse, i.e. y direction, continuous moving magnet with speed 30 mm/s when the magnet is at the vicinity of fully magnetizing the duct channel. Magnetic field is with a quasi static approximation of magnetic field shown in Fig. 3.23.

validated in a narrow channel Hartmann flow superposing a transverse static magnetic field provided by permanent magnet.

Chapter 4

Evaporation-assisted magnetic separation of rare earth ions in aqueous solutions

REE plays an essential role in the energy sector. It is especially true for green technologies like magnetic cooling which was discussed in Chapter 3. This motivates exploration of efficient but low cost and environmentally friendly process technique. As already introduced in Sec. 1.2.1, separation of REE from each other in the dissolved state is a nontrivial task. The different magnetic susceptibilities of the paramagnetic REE offers a new possibility [116], see Fig. 4.1.

To realize this possibility, the present chapter reports works devoted to an understanding of the mechanism underlying REE separation with permanent magnet from an initially homogeneous dissolved state in water solution. An experimental setup (Sec. 4.1) is developed in which a weak evaporation rate can be adjusted. Sec. 4.2 explains the physical processes in the cell and quantifies the resulting heat and mass transfer fluxes. To discriminate between the temperature and concentration contributions in the refractive index field, measured by Mach-Zehnder interferometry, a new algorithm is presented in Sec. 2.1.1. Transport of concentration and temperature fields are simulated to better understand their dynamics and respective impact in the refractive index field, see Sec. 4.4. Both works gives the basis to extract the evolution of the concentration field of the rare earth ions in the cell as shown in Sec. 4.5. The discussion of the results including the hydrodynamic stability of the system in Sec. 4.6 leads to the concrete conclusion that a synergy between evaporation and field gradient force is the mechanism underlying the separation results discussed above.

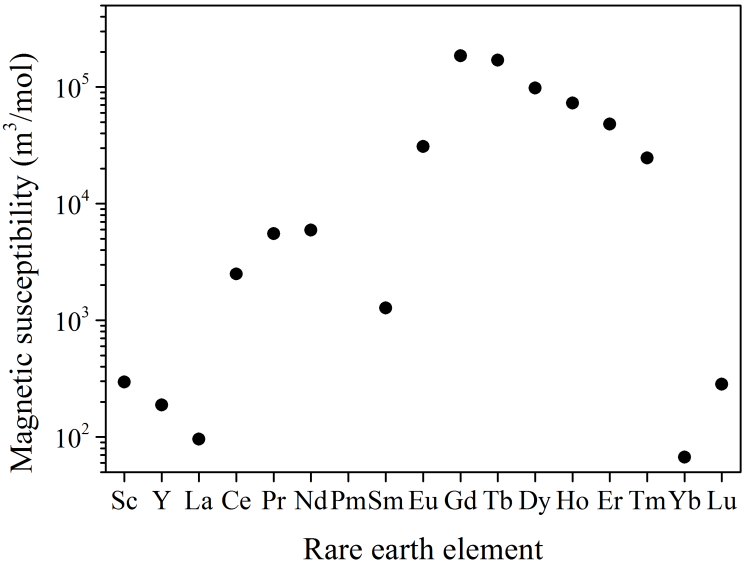

Fig. 4.1 Magnetic susceptibility of 16 REE, without Pm, of its stable isotope.

4.1 Experimental setup

The experimental container shown in Fig. 4.2 consists of three cells: the central measurement cell ($10\times10\times10$ mm^3), made of quartz glass in optical quality(1.25 mm thickness) which is surrounded by two identical seed cells, made of PTFE. All three cells are placed inside a base frame, manufactured from plexiglass. The measurement cell is completely filled with rare earth solution under study at a concentration of c_0 until a flat free interface is established. A rare earth solution of the same type but of a different concentration c is injected into the two neighboring cells. Then, the plexiglass base is closed with a lid using non-magnetic screws and a soft plastic pad to seal it. By this means, a closed system with good optical quality is constructed, which is placed into a Mach-Zehnder interferometer, see Section 2.1.1. The volume ratio of the solutions in the optical and seed cells and the vapor phase is close to 1:1:1.

Three rare earth salt solutions with different concentrations (0, 0.5 and 1 M) are prepared using $DyCl_3$ hexahydrate (99.9 %, abcr GmbH & Co. KG) dissolved in deionized water. The pH is adjusted with hydrochloric acid. Given the equilibrium constant of Dy^{3+}, $\log K_{s10} = 15.9$ at 25°C [144], a pH value of 5.3 results. Above this pH, precipitation and sedimentation starts. Below this value, the solution is free of precipitated clusters, a fact which was verified by dynamic light scattering at pH=5. To completely rule out the formation of $Dy(OH)_3$

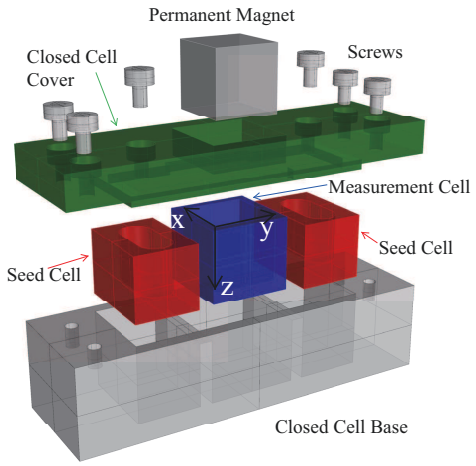

Fig. 4.2 Schematic diagram of the setup consisting of an outer plexiglass cell(gray and green parts) which provides a closed system for mass, a high-quality optical quartz glass measurement cell, two seed cells made of Teflon and the NdFeB permanent magnet.

precipitates, pH=1 was chosen in the experiments and a Millex-LCR millipore 0.45 μm filter was used before filling the cell with the solution.

The molar susceptibility of the solution in the cell is the sum of the susceptibility of the aqueous solution, $\chi_{sol,0}$, at Dy(III) concentration c_0 and pH=1 and a variation, resulting from a change in concentration $\Delta c = c - c_0$ due to solvent evaporation, multiplied by the molar susceptibility of dysprosium ($\chi_{Dy} = 5.5 \times 10^{-7} \mathrm{m}^3/\mathrm{mol}$):

$$\chi_{sol} = \chi_{sol,0} + \chi_{Dy} \Delta c. \tag{4.1}$$

A permanent magnet of size $10 \times 10 \times 10$ mm^3 (Webcraft GmbH, remanence B_r =1280 mT, magnetization of N42) is used to provide a static inhomogeneous magnetic field. The magnet is placed on top of the closed cell at the center of a machined groove inside the lid. Its magnetization direction is oriented along the z direction. The vertical distance between the magnet and the free interface amounts to 3 mm.

The experiments were run at room temperature $(20 \pm 1)^\circ$C and atmospheric pressure. The majority of the experiments lasts approx. 140 min, added by a few number of long-time experiments for up to seven days. The resulting volume loss due to evaporation was measured by analyzing shadowgraphs of the surface profile of the solution remaining in the measurement cells and is discussed later on.

The magnetic field is simulated using Ampere's law based on the same procedure as explained in Sec. 2.2.1 and shown in Fig. 4.3a for a quarter of the cells both as a 3D vector plot and as a contour plot. The resulting 3D magnetic field gradient force within the optical

cell, calculated with Eq. (1.11), is plotted in the same manner in Fig. 4.3b. The dominant

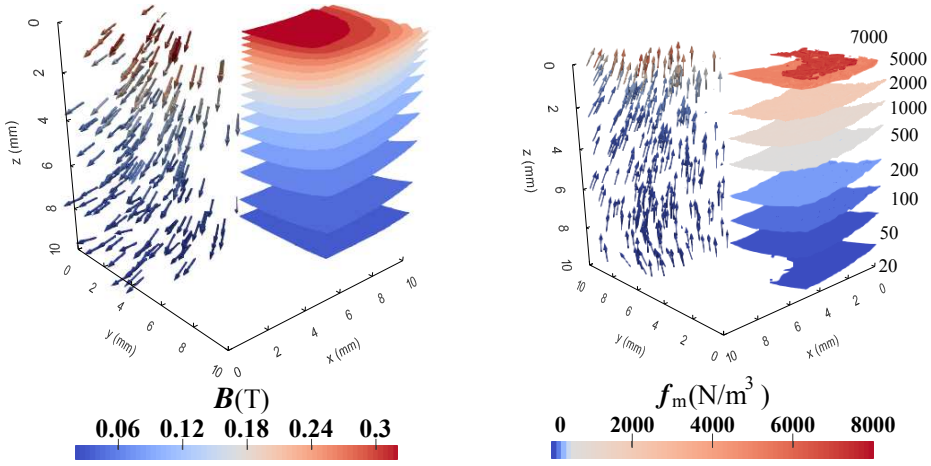

(a) (b)

Fig. 4.3 Simulated 3D (a) magnetic field and (b) field gradient force, $\Delta c = 0$ & $c_0 = 0.5$ M, within the whole inner region of the plexiglass cell and measurement cell, respectively. Iso contour lines and vector field for two sub-figures are scaled with same colorbar provided below, respectively.

force component is that along z direction. In the cell, it reaches its highest value at the liquid-air interface and decreases rapidly along z. The force components in the x-y plane are not negligible, in particular at the interface. They are oriented from the margin of the cell towards the center of the cell.

4.2 Thermodynamics in magnetic separation of rare earth ions in aqueous solutions

For the moment let us leave the magnetic field aside and consider the physical processes which take place at the liquid-gas interface of the dysprosium solution, see Fig. 4.4. While $DyCl_3$ salt is non-volatile, the water molecules evaporate in each of the three cells of Fig. 4.2 until the saturation partial pressure of the respective water solution, corresponding to the ambient temperature, is established. Consider the solution as an ideal one; its saturation pressures obey Raoult's law:

$$p_w = p_v(T)x_w, \tag{4.2}$$

i.e., the partial pressure of the water vapor above the solution depends not only on the saturation vapor pressure $p_v(T)$ of pure water but also on the mole fraction of water, x_w. Since the dysprosium concentration of the seed cell is twice as high as that of the measurement

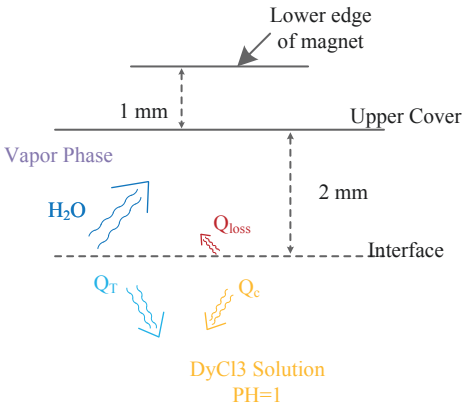

Fig. 4.4 Illustration of physics corresponding to evaporation of water molecules and a zoom into the interface

cell, the mole fraction $x_w = n_w/(n_w + 2c_0V)$ in the seed cell is slightly lower than that in the measurement cell ($x_w = n_w/(n_w + c_0V)$), where n_w stands for the moles of water. As a result, the equilibrium vapor pressure is a bit lower there compared to the measurement cell. By means of this technique, the evaporation rate can be adjusted via the concentration difference between the seed and measurement cells. The resulting vapor pressure gradient in the gas phase forces further evaporation of water molecules from the solution with a lower concentration due to gas molecules in the vapor phase diffusing toward the cell with higher salt concentration. There, water molecules condense at the interface. Thus, the more concentrated solution experiences a slight dilution, while a concentration increase occurs in the less concentrated solution. In the course of this process, the driving pressure gradient in the vapor atmosphere of the cell is gradually diminished over a long period of time.

Evaporation is coupled with fluxes across the interface, where now the focus is entirely on the measurement cell. First, there is a flux of solvent molecules into the gas phase. Hence, the mass of the solutions is not conserved only in its solute content. As a result, the volume of the solution decreases slightly. Correspondingly, a local concentration increase occurs near the interface. Thus, a source term for the concentration field appears. Second, a flux in terms of thermal energy occurs, since the latent heat for evaporation has to be provided. As a result, the local temperature below the interface decreases. This heat flux $Q(t)$ from the boundary into the system is given by

$$\frac{\partial Q(t)}{\partial t} = -\Delta H_{vap} \cdot c_{water} \frac{\partial \delta V(t)}{\partial t} \tag{4.3}$$

where $\Delta H_{vap} = 44kJ/mol$ and $c_{water} = 55.56$ M refer to the molar latent heat and molar concentration of water, respectively. Eq. (4.3) shows that the heat flux is a function of the

evaporation rate, i.e. the volume loss $\delta V(t)$ of water per time unit. To obtain $\partial_t \delta V(t)$, the fact is invoked that the moles of solute ($DyCl_3$) dissolved in water, $n_0 = c_0 V_0$, is a conserved quantity during evaporation, where c_0 and V_0 refer to the initial concentration and volume of the solution. Hence

$$n_0 = c_0 V_0 = const = \bar{c}(t)(V_0 - \delta V(t)), \tag{4.4}$$

i.e., a volume reduction forces the volume-averaged concentration of Dy(III), $\bar{c}(t)$, given by $\bar{c}(t) = \frac{1}{V} \iiint_V c(x,y,z,t)dxdydz$, to increase. Extracting δV from Eq.(4.4) and putting its partial derivative with respect to time into Eq.(4.3),

$$\frac{\partial Q(t)}{\partial t} = -\Delta H_{vap} \cdot c_{water} \cdot V_0 \cdot c_0 \cdot \bar{c}(t)^{-2} \cdot \frac{\partial \bar{c}(t)}{\partial t} \tag{4.5}$$

is obtained. This equation indicates that the heat flux across the surface during evaporation is a function of the initial concentration, initial volume and mean concentration change, and depends nonlinearly on the mean concentration. $\partial \bar{c}(t)/\partial t$ is assumed to be constant over the interface of the solution. This is justified by the fact that the weak evaporation, acting over times less than 140 min, leads to only marginal changes of the initially perfectly flat interface in the cell.

Once the source terms for the concentrations and temperature field have been specified, their transport inside the solution is governed by

$$\frac{\partial T}{\partial t} = \kappa \cdot (\frac{\partial^2 T}{\partial x^2} + \frac{\partial^2 T}{\partial y^2}) \tag{4.6}$$

and

$$\frac{\partial c}{\partial t} = D \cdot \frac{\partial^2 c}{\partial x^2} \tag{4.7}$$

respectively, with a mass diffusivity of $D = 1 \times 10^{-9}$ m^2/ s and a thermal diffusivity of water given by $\kappa = 1.38 \times 10^{-7}$ m^2/ s. Since volume loss can be neglected for experiments shorter than 140 min, see Section 4.4), it is justified to approximate heat and mass transport as 2D and 1D processes, respectively. The transport proceeds by diffusion since the field-gradient force effectively suppresses any evaporation-driven convection, as will be shown later on.

Eqs.(4.6-4.7) are solved by methods described in Sec. 2.2.2. The boundary condition for heat transfer is a Neumann boundary condition at the free interface of the solution and a mixed boundary condition for the heat losses at all other boundaries, i.e. $\frac{\partial q(t)}{\partial t}|_{z=0mm} = \frac{\partial Q(t)}{\partial t}/A_{interface} + S_{loss}$ where S_{loss} refers to the heat losses via the quartz walls of the cell. Since the dominant heat transfer takes place at the interface, it is legitimate to neglect S_{loss}. Harmonic conductivity, i.e. $k = \frac{k_{quartz} k_{fluid}}{k_{quartz} + k_{fluid}}$ is used at the boundary between the quartz and

the solution. The initial conditions for the temperature and concentration are $T_0 = 20.0°\mathrm{C}$ and $c_0 = 0.5$ M, respectively, depending on the experimental conditions. The boundary flux value for mass and heat at the free interface is discussed in Section 4.3.

The target quantity which is used to describe the dynamics in a rare earth solution is the change in the refractive index, $\Delta n(\vec{r},t)$, with respect to the reference field $n_0(c_0,T_0)$. This change, $\Delta n(\vec{r},t)$, can be written as

$$\Delta n(\vec{r},t) = \Delta n[T(\vec{r},t), c(\vec{r},t)] = \Delta n_T(\vec{r},t) + \Delta n_c(\vec{r},t) \tag{4.8}$$

where Δn_T and Δn_c refer to changes in Δn due to changes in temperature and concentration. The refractive index as a function of temperature changes as $\frac{\partial n}{\partial T} = -\frac{1}{10200}\ \mathrm{K}^{-1}$, see [65] while $\frac{\partial n}{\partial c} = \frac{1}{23.31002}\ (\mathrm{M})^{-1}$ holds for that with the concentration of $DyCl_3$ [102]. Thus it is obvious that a change in concentration has a greater weight than a change in temperature. This fact, together with the different transport dynamics of $\Delta T(\vec{r},t)$ and $\Delta c(\vec{r},t))$ due to their different diffusivities, forms the basis for discriminating between $\Delta n_c(\vec{r},t)$ and $\Delta n_T(\vec{r},t)$.

Algorithm developed in Sec. 2.1.1 and 2.1.1 is applied to analyze the dynamics of the refractive index field Δn_m, Eq.(2.13), in the $DyCl_3$ solution, where the following strategy is pursued: the transfer part Δn_t by fitting the experimental data is determined first. Using $\partial_t \Delta c = \frac{1}{\partial n/\partial c}\partial_t \Delta n_t$ it is able to specify the boundary mass flux $\frac{\partial \bar{c}(t)}{\partial t}$ needed to obtain the boundary heat flux, Eq. (4.5). This allows the temperature and concentration field to be simulated by means of which the respective contributions can be studied, Δn_T and Δn_c, in the two-stage evolution found for Δn_t. Finally, this information is used to convert the computed Δn_{cons}, calculated in the second step of the algorithm via Eq.(2.20), into the concentration field of the $\mathrm{Dy}(III)$ ions.

4.3 Dynamics of the refractive index field component Δn_t

First, the evolution of Δn_t for both evaporation and condensation in the measurement cell is studied. It starts with evaporation, as presented in Fig. 4.5a. This figure contains the raw data of one measurement (red triangles) together with the error band obtained from the standard deviation of three independent measurements. Each measurement i can be fitted using the logarithmic function $\Delta n_t = a_i + b_i ln(t + c_i)$. On averaging the fits of three independent experiments (solid curve in Fig. 4.5a), $\bar{a} = -2.8608 \times 10^{-4}$, $\bar{b} = 0.55765 \times 10^{-4}$ and $\bar{c} = 169$ are obtained. Characteristic changes in Δn_t occur in the order of 10^{-4}.

The origin of this variation of Δn_t is the transfer of water molecules and the resulting concentration increase accompanied by a temperature decrease. Given the opposite signs of

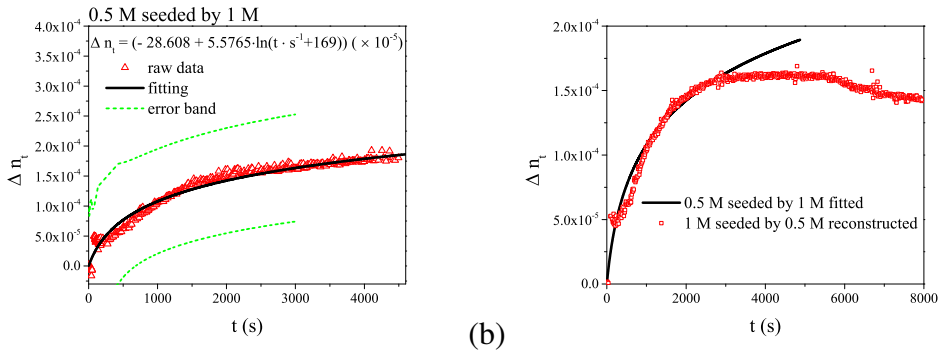

Fig. 4.5 Change of the refractive index component Δn_t, eq.(2.17), as a function of time: (a) evaporation case (0.5 M seeded by 1 M). The error band is a obtained via the standard deviation of fitting curve of 3 independent repeating experiments. (b) Condensation case (1 M seeded by 0.5 M) in comparison with the evaporation case (solid line).

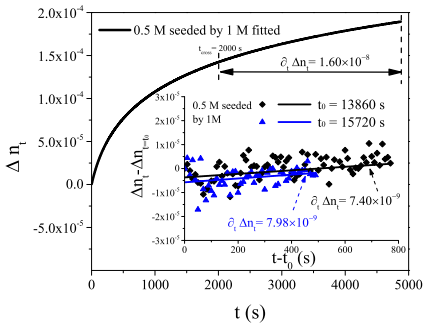

Fig. 4.6 Δn_t as a function of time (0.5 M seeded by 1 M) ranging from 0 s to 4500 s. The inserted figure includes two independent long-term measurements of Δn_t in the case of continuous evaporation shown starting from $t_0 = 13860$ and 15720 s, respectively.

$\frac{\partial n}{\partial T}$ and $\frac{\partial n}{\partial c}$, an increasing Δn_t indicates that water is evaporating from the measurement cell, i.e. as represented by Fig. 4.5. A two-stage evolution with a larger $\partial_t \Delta n_t$ in the first phase and a smaller one in the second phase is noted. Before interpreting this behavior, Fig. 4.5b is compared with that found in the case of condensation when water vapor condenses in the measurement cell. Remarkably, the evolution of $\partial_t \Delta n_t$ in the first phase is identical with that in the case of evaporation. A divergence in the evolution of Δn_t occurs beyond $t_{cross} \approx 2000$ s. From that moment on, Δn_t decreases in the case of condensation while further increasing in the case of evaporation. From the identical evolution in the first phase, I can conclude that the same process obviously take place first, irrespectively of whether the system is prone to condensation or evaporation due to the concentration differences imposed. This process is the evaporation of water molecules until the saturation vapor pressure is achieved as shown in Eq.(4.2). The subsequent second phase is then governed by the diffusion of water vapor

molecules between the measurement and seed cells depending on the differences in the vapor pressure adjusted by the respective concentrations.

Thus, it can be concluded that in the first phase, due to the higher evaporation, both temperature and concentration changes contribute to Δn_t, as also proved in Section 4.4. The second stage, characterized by a weaker slope of Δn_t, is dominated by the concentration contribution due to the decay in the temperature effect. The cross-over time between the two phases, $t_{cross} \approx 2000$ s, marks the moment at which $p_v \approx p_v^{sat}$. Similar t_{cross} for 0.5 M and the 1 M solution, despite their differences in thermodynamic properties is found. Hence, the second phase enables us to estimate the rate of the concentration change,

$$\frac{\partial c(t)}{\partial t} = \frac{\partial c}{\partial n} \cdot \frac{\partial \Delta n_t}{\partial t}, \tag{4.9}$$

due to solvent evaporation since the temperature contribution is now negligible. The required $\partial_t \Delta n(t)$ is plotted for three different experiments in Fig. 4.6. First, it is given as a fit of the data in Fig. 4.5a from $t_{cross} \leq t \leq 5000$ s leading to $\partial_t \Delta n_t = 1.60 \times 10^{-8}$, or $\partial_t c(t) \approx 3 \times 10^{-7}$ mol/(L $\cdot$ s). Second, two long-term experiments were performed, see inset, which lead to nearly identical results. On fitting the data in the intervals $t_0 \leq t \leq t_0 + 800$ s with $t_0 = 13860$ s and $t_0 \leq t \leq t_0 + 450$ s with $t_0 = 15720$, $\partial_t \Delta n_t \approx 7 \times 10^{-9}$, or $\partial_t c(t) \approx 2 \times 10^{-7}$ M/s are obtained. This is finally compared with a 7-day experiment in which a volume loss of 5.4% was detected, which is equivalent to $\partial_t \Delta n_t \approx 3.9 \times 10^{-10}$ s^{-1}. As expected, on the way to thermodynamic equilibrium, hence vanishing vapor pressure differences between measurement and seed cells, a slowly declining evaporation rate which simultaneously decreases $\partial_t \Delta n_t$ and correspondingly $\partial_t c(t)$ is observed. As a conservative estimation for the latter, $\partial_t c(t) = 3 \times 10^{-7}$ mol/(L $\cdot$ s) is taken.

4.4 Supporting heat and mass transfer analysis

Before presenting results on spatially conserved concentration field, it is necessary to identify the concentration and temperature contribution in Δn_{cons}. With the given $\frac{\partial c(t)}{\partial t}$, the heat flux, $\partial Q(t)/\partial t$ (Eq. 4.5) can be calculated and shown in Fig. 4.7a as a function of $\bar{c}(t)$ and $\frac{\partial \bar{c}(t)}{\partial t}$. It is obvious that $\partial Q(t)/\partial t$ is much more sensitive with respect to $\partial \bar{c}(t)/\partial t$ than to $\bar{c}(t)$. Since the time span which is relevant to the measurements consists in the initial 2 hours of magnetization, $\bar{c}(t) \approx 0.5$ M can be therefore safely set. This now allows for an explicit calculation of the heat flux $\partial Q(t)/\partial t$ as a function of $\partial \bar{c}(t)/\partial t$ as shown in Fig. 4.7b. For the concentration under study ($c_0 = 0.5$ M), $\frac{1}{A_0}\frac{\partial Q_{heat}}{\partial t} = -4.89 \times 10^3 \frac{J}{M}\frac{1}{A_0}\frac{\partial c(t)}{\partial t} = -14.67$ W/ m^2 is obtained, which is the corresponding heat flux due to the evaporation of water molecules.

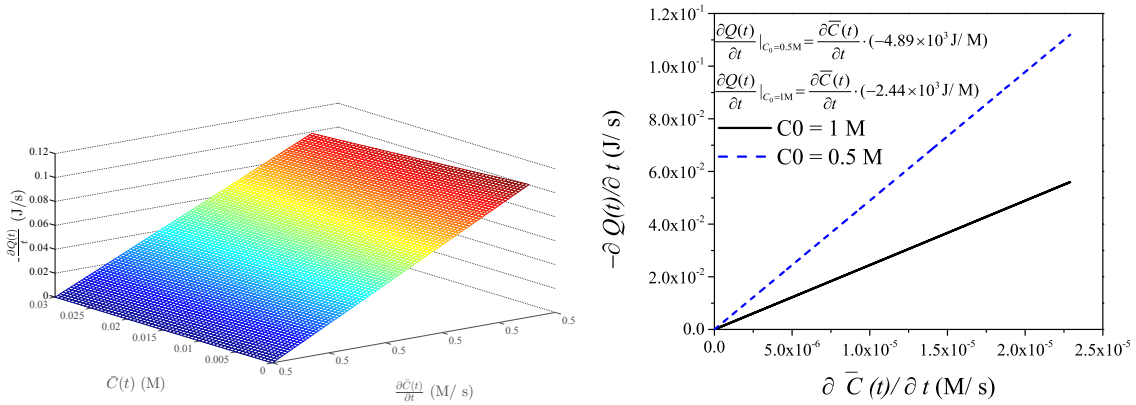

(a) (b)

Fig. 4.7 (a)Heat flux as a function of mean field concentration and the rate of concentration change ($c_0 = 0.5$ M) and (b) Heat flux as a function of the rate of concentration change.

This value is then used as the boundary condition for the simulation of the temperature field inside the cell, solve Eq. (4.6) with simulation scheme in Section 2.2.2, which is plotted in Fig. 4.8. Three important facts are noted here:

1. As expected, the temperature field has a 2D behavior due to heat exchange between the fluid and the quartz glass.

2. The temperature of the solution decreases due to the evaporation. Given the rather high diffusivity of the solution, the temperature inhomogeneity is more significant along time than space and the average temperature decreases by about -0.35 K after 1000 sec.

3. At the same time the temperature difference between the interface and the bottom of the cell does not exceed 0.1 K. The spatial gradient of temperature does not change dramatically after 500 s.

The temperature field gives rise to a corresponding refractive index field via $n(y,z) = T(y,z)\partial n/\partial T$. The latter can be translated into a fictitious concentration field using $c(y,z) = n(y,z)/\partial n/\partial c$. This fictitious concentration field, mimicked by temperature changes, is plotted in Fig. 4.8b.

As it can be seen from Fig. 4.8b, the temperature field is responsible for a spatial concentration difference of approximately 0.15 mM at a representative time t=500 s. On comparing this with the concentration change of 2 mM, cf. Sec. 4.5, the temperature contribution, although present, amounts to less than 10% of the concentration change derived from the measured refractive index.

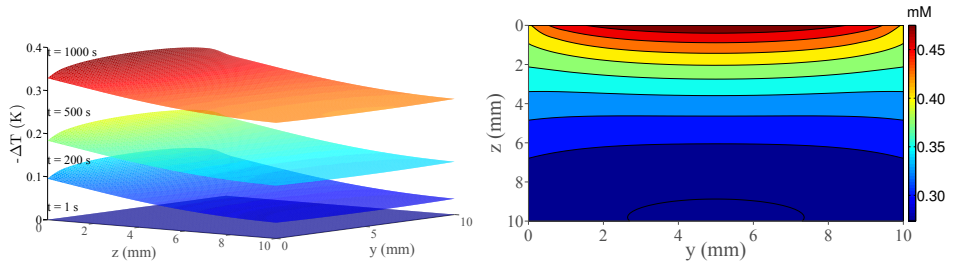

(a) (b)

Fig. 4.8 (a)2D simulation result of temperature field at t= 1, 200, 500 and 2000 s after evaporation has started at the liquid-gas interface and (b) fictitious concentration field due to a change in the temperature field at t = 500 s.

To further support the validity of a discrimination between Δn_T and Δn_c, Eq. (4.8), dynamics of the temperature field is then compared with that of the concentration field. For this purpose, in Fig. 4.9 one-dimensional plots of T(z,t) and c(z,t) along the center of the x-y plane (x= 5 mm, y= 5mm) is shown. It can clearly be seen that the heat transfer reaches a

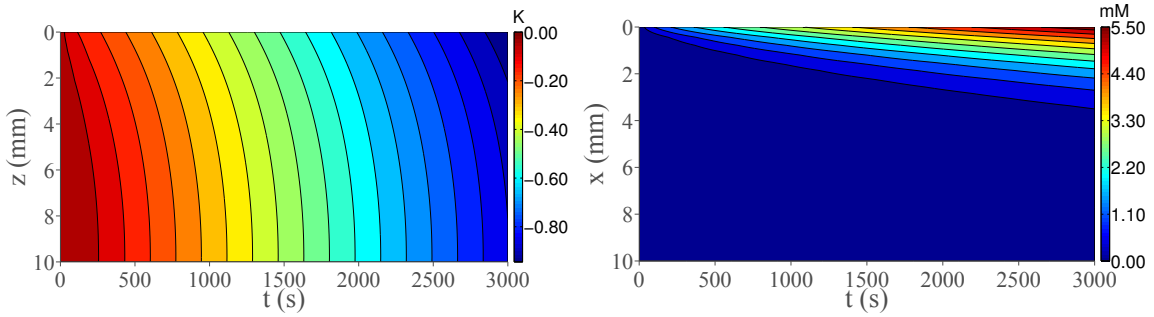

(a) (b)

Fig. 4.9 1D plots of temperature (a) and concentration (b) as function of t and z at the center of the plane (x=5 mm; y=5 mm) as obtained by simulation.

stationary state in which the gradient of temperature along the z direction is constant. By contrast, due to the low diffusivity of the solute compared to that of heat, the diffusion process of the concentration field (Fig. 4.9) is still in a developing stage after 3000 s. Both facts about the temperature field, namely that it (i) falsifies the concentration field, derived from $n(\vec{r})$, by not more than 10% and (ii) already approaches a steady state while the concentration field is still developing, justify the validity of the translation into concentration units in Fig. 4.10.

4.5 Dynamics of an evaporation-induced concentration increase with the presence of the magnetic field gradient force

The second step of the compensation algorithm is performed by applying Eq. (2.20) to determine Δn_{cons}. The analyses in Sections 4.3 and 4.4 have provided the necessary information for this purpose: (i) The overall time-dependence in the initial phase is mainly caused by the temperature decrease due to evaporation. (ii) The concentration and temperature field decouple on a longer time scale due to their different diffusivities and (iii) the temperature contribution is marginal after t_{cross}. These considerations clearly justify the conversion of conserved part, Δn_{cons}, into the concentration field, which is done via a division by $\frac{\partial n}{\partial c} = \frac{1}{23.31002}$ $(\mathrm{M})^{-1}$ and shown in Fig. 4.10. The most important issue visible in Fig. 4.10 is the formation of an oval region of elevated Dy(III) enrichment below the interface. This region continues to expand slowly between 60 s and 2000 s. The concentration iso-contour line resembles that of the magnetic field gradient force, cf. Fig. 4.3b. This process is entirely governed by diffusion. There is no convective contribution detectable.

Another prominent feature of Fig. 4.10 is the formation of boundary layers at the vertical and horizontal quartz glass walls of the cell. Actually, these are fictitious concentration boundary layers caused by a small heat transfer across the quartz walls which was not taken into account in the simulations. As expected, this transfer is weaker at the sidewalls, due to the isolating effect of the surrounding air, and stronger at the bottom because of the higher heat conductivity of plexiglass (0.2 W/ m·K). They slowly expand until the temperature field reaches a steady state.

It is useful at this stage to recall again the essence of the two-step compensation algorithm. In the first step, $\Delta n_t(t)$ was determined. Analyzing this enabled the temperature and concentration field to be decoupled over time and showed that in the second phase the temperature contribution vanished. In the second step, Δn_{cons} was obtained, showing the decoupling of the temperature and concentration field in space. As a result, it was possible to unambiguously correlate the computed concentration field at the oval part shown at the top of each subfigure of Fig. 4.10 with the enrichment of Dy(III) ions in this region. However, the total concentration enrichment is given by the sum of Δn_{cons} (Fig. 4.10) and Δn_t (Fig. 4.5a), divided by $\frac{\partial n}{\partial c}$. Taking into account the temperature contribution to Δn_t in the first phase, a conservative estimation of the maximum enrichment amounts to 2 mM, cf. Fig. 4.10.

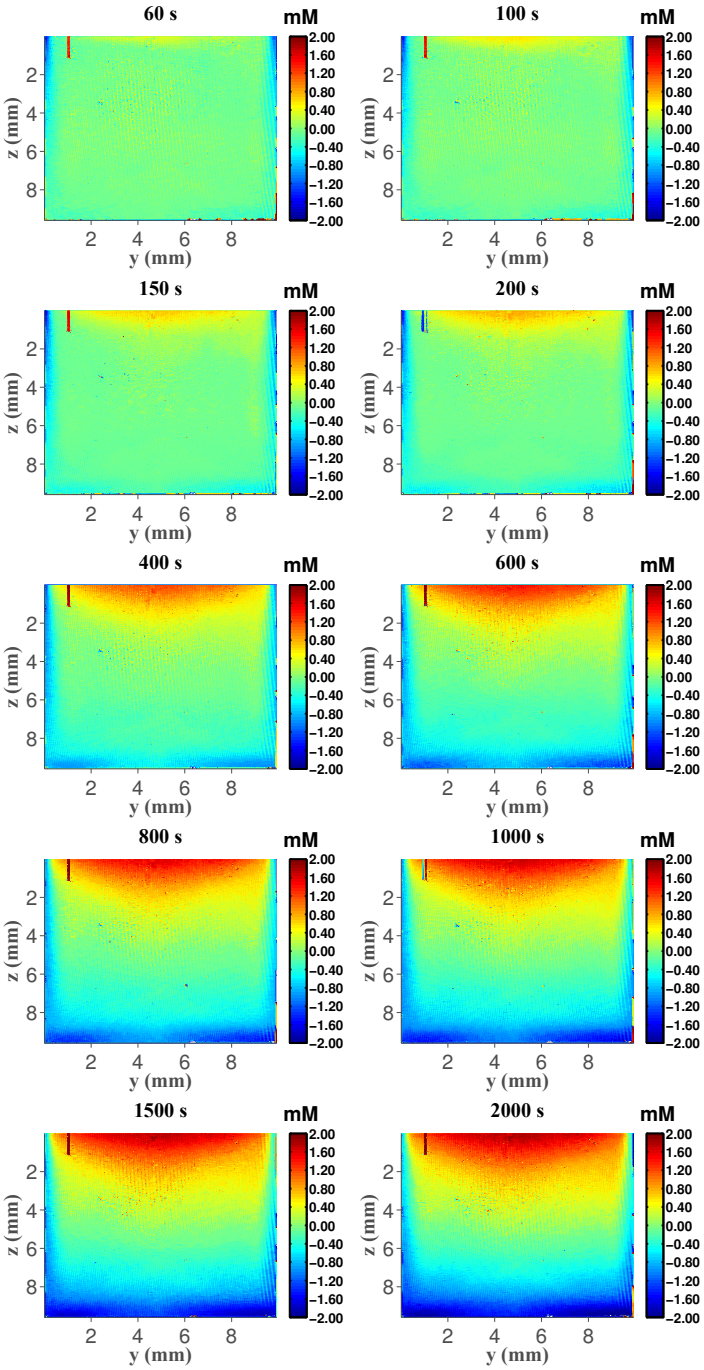

Fig. 4.10 2D concentration field in 0.5 M $DyCl_3$ solution measured with inteferometer seeded by 1 M $DyCl_3$ solution between 60 s and 2000 s after magnetic field is applied and vaporization starts; with a spontaneous fictitious concentration field contributed by a temperature field.

4.6 Hydrostatic analysis and instability analysis with FHD

The experimental results in Fig. 4.10 show the transport of both Dy(III) ions and heat in the presence of the magnetic field gradient force under the condition of a continuous weak evaporation. With the two-step compensation algorithm which was developed, it was able to "decouple" the concentration field from the temperature field in the sense of their spatial distribution and its variation in time. In conjunction with simulations of the development of both fields under experimentally specified boundary conditions (Section 4.4), it is clear that more than 90% of the measured change in the refractive index of the weakly evaporating $DyCl_3$ solution is caused by the local increase in the Dy(III) concentration in the field gradient (Fig. 4.10).

The experimental setup in the present work was designed similarly to that of former works carried by my colleagues [99, 102]. The marked difference is that a free interface is admitted here at which weak evaporation is forced in terms of a vapor diffusion in a closed system. The similarity of the results obtained strongly suggest that evaporation is the missing puzzle piece necessary to understand the physics behind the enrichment of RE ions in the field gradient.

Evaporation proceeds in two phases inside the experimental cell. First, depending on the concentration, the respective saturation pressure in each cell is approached in the comparatively rapid first phase. Second, the vapor pressure differences due to the different concentrations sustain a diffusional vapor flux between the cells, giving rise to a lower evaporation rate in the second phase. These assertions were proved by a condensation experiment in Section 4.3.

To further understand the resulting transport process with the presence of magnetic field in the present configuration, an analysis on Kelvin force altered momentum equation is needed here. Generally, the evaporation of water molecules leads to the formation of a boundary layer of higher Dy(III) concentration at the surface. This concentration increase, $\Delta c = c - c_0$, has two consequences. First, it increases the magnetic susceptibility in this zone by $\Delta\chi_{sol} = \chi_{Dy}\Delta c$ due to Eq.(4.1). Second, the density is elevated by $\Delta\rho = \rho - \rho_0 = \rho_0\alpha\Delta c$, resulting from a positive densification coefficient $\alpha = 0.243\ \mathrm{M}^{-1}$ [102]. As a result, a heavier enrichment layer overlies a less dense bulk solution. Without a magnetic field, this boundary layer is hydrodynamically unstable, as discussed below. However, in the presence of the field gradient force no instability is observed. Analysis starts with the hydrostatic equation

$$\nabla p = \vec{f}_g + \vec{f}_m = g(\rho_f + \frac{\chi_{sol}}{2\mu_0 g}\frac{\partial B^2}{\partial z})\vec{e}_z + \frac{\chi_{sol}}{2\mu_0}\nabla B^2\ |_{xy} \tag{4.10}$$

where $\vec{f}_g$ and $\vec{f}_m$ represent the densities of the gravitational and magnetic field gradient force and $\nabla B^2 \,|_{xy} = \frac{\partial B^2}{\partial x} \cdot \vec{e}_x + \frac{\partial B^2}{\partial y} \cdot \vec{e}_y$. Eq. (4.10) contains two vertical force components: gravity, pointing downwards, and the z-component of $\vec{f}_m$, pointing upwards, as well as the radial component of $\vec{f}_m$, acting in the horizontal plane. Note that the first term on the right-hand side suggests that an apparent density $\rho_{app} = \rho_f + \frac{\chi_{sol}}{2\mu_0 g}\frac{\partial B^2}{\partial z}$ could be introduced. This expresses the fact that the fluid density ρ_f is slightly tuned by the magnetic field gradient, which forms the basis of ferrohydrostatic separation[88]. The dependence of ρ_f and χ_{sol} on the concentration change Δc is invoked to write

$$\nabla p = g(\rho_0 + \frac{\chi_{sol,0}}{2\mu_0 g}\frac{\partial B^2}{\partial z})\vec{e}_z + \frac{\chi_{sol,0}}{2\mu_0}\nabla B^2 \,|_{xy} + (\rho_0 \alpha g \Delta c + \frac{\chi_{Dy}\Delta c}{2\mu_0}\frac{\partial B^2}{\partial z})\vec{e}_z + \frac{\chi_{Dy}\Delta c}{2\mu_0}\nabla B^2 \,|_{xy} \tag{4.11}$$

where $\chi_{sol,0}$ refers to the susceptibility at c_0. In the absence of evaporation, i.e. $\Delta c = 0$, only the first two terms of Eq. (4.11) are different from zero. In a closed cell, the system is completely stable, since there are no unbalanced force components because the concentration and susceptibility are spatially uniform. The action of $\vec{f}_g$ and $\vec{f}_m$ is now compensated for by the normal reaction from the walls. This is in agreement with other works[109, 110] according to which fluids can only be manipulated based on the magnetic field gradient in the case of non-homogeneous liquid media, i.e. differences in susceptibility. Strictly speaking, the presence of the free surface at $\Delta c = 0$ additionally requires the Moses effect to be taken into account [97]. It describes the elevation of the free surface of an otherwise homogeneous fluid, i.e. $\Delta c = 0$, to become an isoline of the magnetic pressure. However, this effect is very small here and can be neglected.

If $\Delta c \neq 0$, the situation becomes more involved. Eq. (4.11) shows that in the horizontal plane there is an unbalanced component of $\vec{f}_m$, as $\vec{f}_g$ acts only in the vertical direction. Fig. 4.11a plots this radial component of f_m inside the solution at different heights below the interface. Note that the vertical distance between magnet and interface is 3 mm. $\vec{f}_m(r)$ is the largest at the rim of the cell and vanishes at the center of the cell. With increasing distance from the magnet, the magnitude of the force components is drastically reduced. Generally, $\vec{f}_m(r)$ points inwards towards the center of the cell.

Hence, fluid elements in the boundary layer are pushed horizontally from the rim of the cell towards the center. This is the mechanism by which the originally planar Dy(III) ion boundary layer, established by evaporation at the interface, is transformed into the concave region visible in Fig. 4.10.

Actually, in the presence of a concentration gradient, and hence a susceptibility gradient, the rotation of the field gradient force, $\nabla \times \vec{f}_m$, no longer vanishes [97, 145]. Thus, there must be a microconvection beyond the resolution of the measurements, driving the transformation

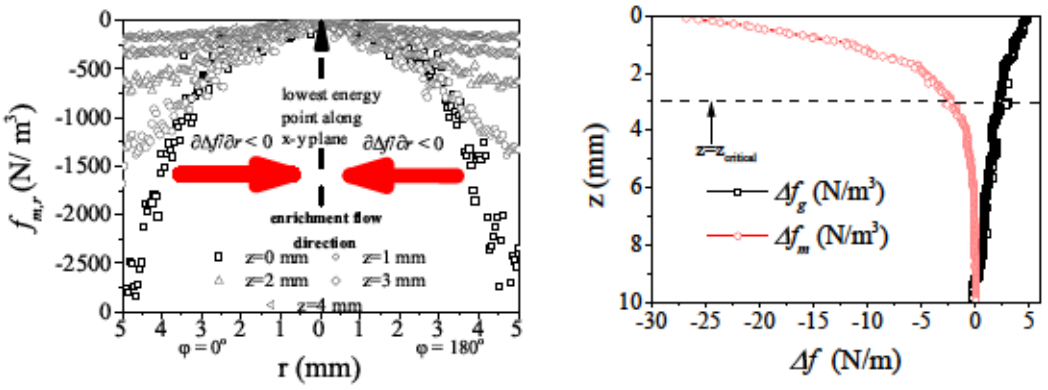

(a) (b)

Fig. 4.11 (a) Radial component of the magnetic field gradient force at different heights below the interface ($c_0 = 0.5$ M). A cylindrical coordinate system is used with the polar plane center at x = y = 5 mm. A positive azimuthal direction for ϕ is therefore anti-clockwise. (b) Vertical force components Δf_m and Δf_g, referring to the terms in Eq. (4.10) containing a Δc. Δf_g is computed at t = 600 s with a concentration processed by two-step compensation along z at y = 5 mm, averaged along x.

in the boundary layer from its initially planar shape towards a concave shape. However, in the absence of a macroscopically detectable velocity, hydrostatic Eq.(4.10) is approximately valid for a semi-quantitative explanation of the magnetic separation process.

To answer the question of why the concave enrichment boundary layer is levitated by the vertical force components in Eq.(4.11) instead of falling, the corresponding Rayleigh number of the boundary layer is inspected. The Rayleigh number quantifies the ratio of buoyancy and viscosity force times competition between momentum and thermal diffusivity. $Ra = -\frac{g\alpha \frac{\partial c}{\partial z} l_c^4}{D\nu} = -\frac{l_c^4}{D\mu} \frac{\partial \vec{f}_g \cdot \vec{e}_z}{\partial z}$, where the minus was introduced because $\partial f_g / \partial z < 0$ and $\vec{f}_g \cdot \vec{e}_z > 0$. Taking the values in Fig. 4.10, $Ra \approx 3 \times 10^4$ is obtained. This value considerably exceeds the critical Rayleigh number $\mathrm{Ra}_{critical} = \mathrm{O}(10^3)$ [146]. Thus, this configuration is prone to a Rayleigh-Taylor (RT) instability, frequently also termed "density fingering" when it occurs in miscible liquids. However, no RT instability is observed in the presence of $\vec{f}_m$, as already stated above.

The reason for this is that the stability is modified by $\vec{f}_m$. The impact of $\vec{f}_m$ could be theoretically quantified by introducing a magnetic Rayleigh number similar to the case thermomagnetic convection [147–150]. Let us consider a layer of ferrofluid exposed to both a vertical magnetic field gradient and to a stabilizing temperature gradient due to heating from above.

Since the magnetization is a function of temperature, a fluid element undergoing a small adiabatic upward motion exhibits a higher magnetization than its surroundings. As

a result, it experiences a magnetic force in the direction of the field gradient. Hence the perturbation reinforced and the originally quiescent ferrofluid layer is destabilized by the onset of convection, provided the critical magnetic Rayleigh number is exceeded. Despite some similarities, the present problem differs from thermomagnetic convection with regard to several issues, such as much lower susceptibility and a susceptibility gradient generated dynamically by a concentration gradient instead of a temperature gradient. Furthermore, no theory has been developed for this case, and hence there are no defined critical Rayleigh numbers.

For that reason, qualitative explanation on how the gravitational force, acting downwards parallel to $\vec{e}_z$ ($\vec{f}_g \cdot \vec{e}_z > 0$), is reduced by the field gradient force ($\vec{f}_m \cdot \vec{e}_z < 0$) acting in the opposite direction is presented. Attampt is sought to mimic the stabilization provoked by the field gradient using a modified Rayleigh number Ra*

$$\mathrm{Ra}^* = -\frac{l_c^4}{D\mu}\frac{\partial \vec{f}\cdot\vec{e}_z}{\partial z} = -\frac{l_c^4}{D\mu}\frac{\partial(\vec{f}_g+\vec{f}_m)\cdot\vec{e}_z}{\partial z} \tag{4.12}$$

Forcing enters the Rayleigh number via the derivative with respect to z. Upon comparing the respective derivatives of $\vec{f}_g$ and $\vec{f}_m$ in Fig. 4.11b it becomes obvious that $\partial f_g/\partial z$ is approximately five times smaller than $\partial f_m/\partial z$. That is, the latter overcompensates for the gravitational force and modifies the Rayleigh number of the layer, hence Ra* becomes subcritical, i.e. Ra$^* << Ra_{crit}$. This is the physical mechanism of the levitation of the Dy(III)-ion enrichment layer observed. It finally manifests in the fact that the iso-concentration lines follow the contour lines of the magnetic pressure, as becomes obvious when Fig. 4.12a is compared with Fig. 4.10.

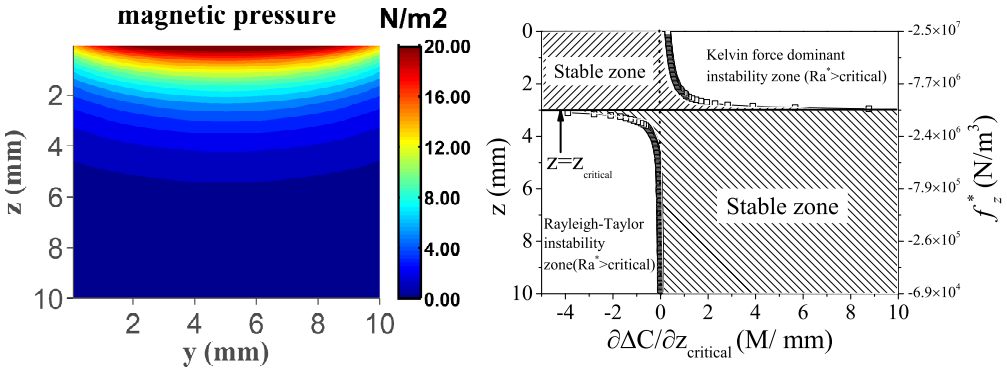

(a) (b)

Fig. 4.12 (a) Magnetic pressure isolines and (b) stability diagram, $\frac{\partial \Delta c}{\partial z}\,|_{Ra^\star=0}$ vs. z-coordinate at $c_0 = 0.5$ M.

Having clarified the mechanism of paramagnetic levitation, attempt to specify the critical concentration gradient of the paramagnetic ions which can be kept stable by the magnetic field gradient is presented. A very conservative estimation is made by taking $\mathrm{Ra}^* = 0$ as the respective condition. That is, the gradient $\frac{\partial \Delta c}{\partial z} \mid_{Ra^\star=0}$ at which the field gradient force nullifies the force by gravity is determined:

$$Ra^* = 0 = \frac{\partial(\vec{f}_g + \vec{f}_m) \cdot \vec{e}_z}{\partial z} = \frac{\partial(\rho_0 g(1+\alpha\Delta c) + \frac{(\chi_{sol,0}+\chi_{Dy}\Delta c)}{2\mu_0}\frac{\partial B^2}{\partial z})}{\partial z} \tag{4.13}$$

With $\vec{f}_{z0} = f_{z0} \cdot \vec{e}_z = \frac{1}{2\mu_0}\frac{\partial B^2}{\partial z} \cdot \vec{e}_z$ obtains

$$\frac{\partial \Delta c}{\partial z} \mid_{Ra^\star=0} = -\chi_{sol,0} \cdot \frac{\frac{\partial f_{z0}}{\partial z}}{\rho g \alpha + \chi_{Dy} f_{z0}} \tag{4.14}$$

$\partial\Delta c/\partial z \mid_{Ra^*=0}$ depends on two variables: on the c_0 which enters $\chi_{sol,0}$, and on the distribution of the magnetic field, determining f_{z0} and its derivative. Since the influence of c_0 is very weak and can be neglected, the main impact results from f_{z0}. Due to its negative sign, Eq. (4.14) possesses a singularity at $f_{z0} = -\frac{\rho g \alpha}{\chi_{DyCl_3}} \approx -4.32 \times 10^6$ N/m^3. This value can be converted into the corresponding z coordinate. For the magnetic field used in this setup, $z_{crit} \approx$ 3 mm is obtained. Actually, the lines $z = z_{crit}$ and $\partial\Delta c/\partial z \mid_{Ra^*=0} = 0$ divide the stability behavior of the system into 4 quadrants, see Fig. 4.12b. In two of them, the upper left quadrant and the lower right one, the system is stable. Our system, characterized by $\partial\Delta C/\partial z < 0$, falls into the upper left quadrant, which is bounded by $z < z_{crit}$ and $\partial\Delta c/\partial z \mid_{Ra^*} \leq 0$. Our concave boundary layer, enriched in Dy(III) ions, is unconditionally stable, irrespectively of the magnitude of the negative concentration gradient established. This is due to the dominance of the field gradient force over the gravitational force for $z < z_{crit}$ and the linear dependence of both the density and susceptibility on the concentration, which keeps the force ratio unchanged. A second stable quadrant is the lower right one, encompassed by $z > z_{crit}$ and $\partial\Delta c/\partial z \mid_{Ra^*=0} \geq 0$. Since the density decreases along with the concentration, this quadrant is characterized by a stable density stratification not perturbed by the weak field gradient.

By contrast, the system can become unstable in the non-shaded regions. Although these two types of instability are both directly related to the concentration distribution, they differ from each other intrinsically, see Fig. 4.13. The instability in the lower left quadrant is caused by the density gradient, while that in the upper right quadrant has its origin in the susceptibility gradient. At the lower left quadrant, bounded by $z > z_{crit}$ and $\partial\Delta c/\partial z \mid_{Ra^*=0} \leq 0$. In this zone, the field gradient force is weak and of the same order as the gravitational one. Hence, for $Ra > Ra^\star = 0$, an existing unstable density stratification can give rise to the

onset of Rayleigh Taylor instability, forming a downward flow parallel to the gravitational direction.

The second instability type can occur in the upper right quadrant, $0 < z < z_{crit}$, if $\frac{\partial \Delta c}{\partial z} > \partial \Delta c / \partial z \,|_{Ra^*=0} \geq 0$. It bears a certain similarity to the Rosensweig instability in a ferrofluid [151]. Due to its high initial susceptibility, even small magnetic fields are sufficient to lift the ferrofluid against gravity and /or to form characteristic spikes at their interface. Keeping in mind that the magnetic susceptibility of the $DyCl_3$ solution is smaller than that of a ferrofluid by a factor of more than 1000, the effects to be expected by the predicted susceptibility-driven instability will be significantly smaller.

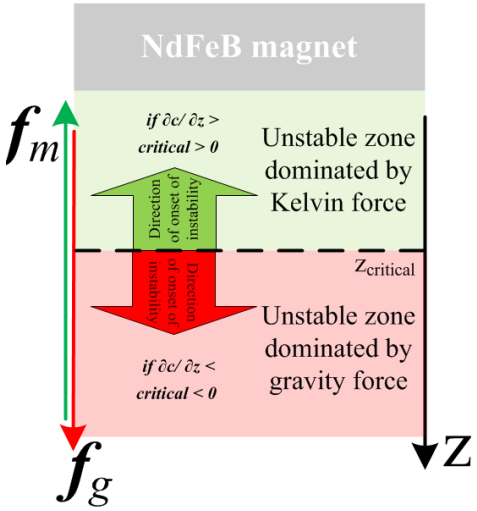

Fig. 4.13 Illustration of instability zone and its onset direction under the present experimental configuration

4.7 Chapter summary

A dedicated experimental setup was developed to understand why previous experiments in rare earth solutions show an enrichment of paramagnetic ions in a magnetic field gradient contrary to the expected delocalization by Brownian motion. The key element is the adjustment of an evaporative flux at the free surface of the $DyCl_3$ solution to prove that evaporation triggers this magnetic separation process.

Evaporation gives rise to fluxes of both heat and water molecules across the interface. Therefore, the resulting change in the refractive index of the $DyCl_3$ solution is affected by both the concentration and the temperature. To discriminate between the two contributions in the Mach-Zehnder interferometry approach, a new two-step compensation algorithm

was developed and applied together with numerical simulations of the concentration and temperature fields. By these means, I could clearly show that more than 90% of the refractive index increase in the boundary layer at the free surface most exposed to the field gradient is caused by the increase in the Dy(III) concentration. The close similarity of the present results to those obtained in seemingly closed cells furthermore conclusively proves the initial hypothesis that evaporation is the supporting process for the magnetic separation of RE ions.

To understand the underlying mechanism, I started out by analyzing the hydrostatics of the solution. It has been shown that the unbalanced radial component of the field gradient force is responsible for shaping the evaporation-driven concentration boundary layer into the observed concave shape. Generally, the evaporation-driven concentration boundary layer is hydrodynamically unstable, because it is heavier than the underlying bulk fluid. It is the field gradient force, acting in the opposite direction to gravity, which suppresses the resulting Rayleigh-Taylor instability. It was shown that the gravitational force acting on the boundary layer, expressed in a non-dimensional manner by the Rayleigh number, is drastically diminished by the approximately five times larger magnetic field gradient force. As a result, the supercritical value of the Rayleigh number is reduced to a subcritical one at which the Rayleigh-Taylor instability cannot set in. This is the origin of the observed levitation of the Dy(III) boundary layer in the magnetic field gradient.

Competition between a change in the gravitational force and a change in the vertical magnetic field gradient force given a local concentration gradient is then considered. A conservatively approximated stability criterion is calculated using a resulting Rayleigh number equivalent to 0. Thus, $\partial \Delta C/\partial z\,|_{Ra^*=0}$ as a function on the $f_{m,z}$ shows a singularity at $z = z_{crit} \approx 3$ mm. Both lines, $\partial \Delta C/\partial z = 0$ and $z = z_{crit}$, divide the stability behavior of the system into two regions of instability and two regions of stability, see Fig. 4.12. According to this stability diagram, the evaporation-driven enrichment layer is found above $z > z_{crit}$, i.e. in the zone where $f_{m,z}$ greatly dominates f_g and is therefore unconditionally stable in the present magnetic field. As a side product, a new susceptibility-driven instability is predicted provided $\partial \Delta C/\partial z > 0$ and $z < z_{crit}$, which should lead the solution to flow upwards.

Beside answering the important question of what mechanism underlies the observed magnetic separation of rare earth ions, the present study points to a series of issues in this process which have neither been addressed nor fully understood. As discussed above, a microconvection has to be responsible for the reshaping of the originally planar evaporation-driven boundary layer. There is a total lack of experimental insights into this type of convection. As a consequence, a more detailed stability analysis of the linearized Navier-Stokes equation [146] is desirable for a better understanding. This also holds for the predicted susceptibility-gradient-driven instability.

Chapter 5

Conclusions and future works

5.1 Conclusions

5.1.1 Heat transfer in magnetic cooling

Transport process manipulation by means of magnetohydrodynamics (MHD) in magnetic cooling and ferrohydrodynamics (FHD) in magnetic separation of rare earth ions from a salt solution is studied in this dissertation.

The primary aim for the first part of work is to enhance heat exchange between solid state refrigerant, acting also as regenerator and heat exchanger, and the heat transfer fluid pumped periodically between the hot and cold end with MHD convection. While due to the nature of separation, mixing of the enriched rare earth salt has to be minimized by means of FHD. This is especially true since FHD does not directly contribute to an enrichment or dilution of rare earth solution. In fact, it influences directly the velocity field and hence transport process of rare earth salt. Consequently, separation efficiency could be enhanced with a suppressed convection.

The investigation of heat transfer in magnetic cooling started with two simplified active magnetic regenerator model for measurement technique validation. The heat exchange between parallel gadolinium plates, with an 8.4 mm space in between, and n-decane in a 350 mT homogeneous magnetic field was monitored at the fluid side using a Mach-Zehnder interferometer (MZI). The corresponding temperature measurements directly at the surfaces of the Gd plates were conducted using thermocouples. A simplified 1-D finite volume based simulation was used for selecting n-decane as heat transfer fluid which allows a sufficiently high temperature increase measurable for the MZI. Space- and time-resolved temperature data are obtained with the setup and algorithm for interferogram processing and extrapolation.

The effect of a finite time of mag- and demagnetization was clearly visible in the experiments. It results in a spatially delayed release of ΔQ_0 causing an additional and undesired temperature gradient inside the heat transfer fluid. Another important result is the overview over the complete temperature profiles during mag- and demagnetization along the centerline normal to the Gd plates which is largely unaffected by the finite speed of magnet motion. The temperature gradient derived at fluid side shows a significant drop down during the first three seconds. As a result, the heat flux is reduced by about 80% during de- and magnetization process in this time span. The energy exchange between Gd and n-decane reaches approx. 25% after 5 s.

An increase in the operating frequency is a crucial question in order to achieve acceptable cooling powers with limited (as expensive) MCM material quantities. One of the key points to be solved on this way is the minimization of losses due to the heat transfer between the refrigerant and heat transfer fluid. Although the present work focuses on stagnant fluid without natural or forced convection - in contrast to any beneficial machine - the visual insights into the dynamics of diffusive heat transfer are useful for a basic understanding of the heat transfer in an AMR.

As the magnetic field $\vec{B}$ is an intrinsic component in any magnetic cooling device, magnetohydrodynamic (MHD) convection appears an interesting concept to enhance heat transfer. To create MHD convection in the aqueous-based electrically conducting heat transfer fluid, an electric current has to be injected. This current interacts with $\vec{B}$ to give rise to a Lorentz force which stirs the fluid, thereby enabling a higher heat transfer.

To deliver a proof-of-principle for the MHD convection concept, a thin gadolinium plate was placed in a transparent cuboid glass cell filled with the heat transfer fluid. For the latter an alkaline solution (0.5 M NaOH) was used which provides sufficient electric conductivity with vanishing corrosion of MCM. Two permanent magnets were combined to form a more or less 2D magnetic field to trigger both the MCE and the MHD convection. The resulting magnetic field was simulated by means of a 3D finite element solver and compared with measurements using a Gaussmeter. Electric currents ranging from 1 mA to 9 mA were injected into the NaOH solution using transparent ITO glass electrodes. In this particular electrode-magnet arrangement, a primary swirling flow sets in, rotating in planes parallel to the gadolinium plate. It is accompanied by a weaker secondary flow which is directed toward the Gd plate at the rim and away from the Gd plate at its center. The MHD convection was measured by means of PIV. The characteristic velocity has an order of magnitude of 1 mm s-1 and increases linearly with the electric current. By applying a Mach-Zehnder interferometer, space- and time-resolved temperature data were obtained during the magnetization and demagnetization of Gd. To quantify the differences in the heat transfer with and without

MHD convection, an enhancement factor, E_{enh}, cf. eq.(3.12), was calculated. This factor, which reflects the difference in thermal energy transferred into the heat transfer fluid with and without MHD convection, was found to increase more or less linearly with the electric current. Even small currents of 3 mA give rise to a significant heat transfer enhancement of about 40 % by means of a MHD flow. Furthermore, the results demonstrate that it is feasible to enhance the heat transfer with MHD convection even in the demagnetization phase although to a weaker extent compared to the magnetization stage.

Based on these encouraging results, the MHD convective heat transfer concept is worth testing further in real AMRs. To create efficient MHD convection, the Lorentz force density $\vec{f}_L$ should be rotational, i.e. $\nabla \times \vec{f}_L \neq 0$. This can be achieved e.g. by imposing an inhomogeneous current density $\vec{j}$ in the presence of a homogeneous $\vec{B}$. Let us consider for a moment a Halbach cylinder used to generate the favorable in-plane magnetization of the MC plate material. One option to incorporate the required electric field could consist in integrating pairs of small copper electrodes of a similar height as the MCM plate at different places in the AMR stack. If the opposing electrodes have a different cross section, an inhomogeneous current density is assured. As a result, a Lorentz force perpendicular to the direction of the forced flow through the AMR appears; this is stronger at the electrode with a smaller cross section, thereby stirring the alkaline fluid additionally in a spanwise direction.

Replacement of water as heat transfer fluid with GaInSn, a liquid metal, is tested in a section of a simplified AMR between two parallel plates made of the MCM. The velocity field in a static magnetic field with an inhomogeneous flux density distribution is measured in between two Shercliff walls by ultrasound Doppler technique. The experimental results on velocity distribution between Shercliff walls agree well with the theories. This is visible in an obvious change in velocity profile with and without static magnetic field.

5.1.2 Magnetic separation of REE

Results are obtained for magnetic separation of REE from initially homogeneous solution. A dedicated experimental setup was developed to understand why rare earth solutions demonstrate a robust but not entirely repeatable enrichment when superposed with a magnetic field gradient. The key element is the adjustment of an evaporative flux at the free surface of the $DyCl_3$ solution. Evaporation gives rise to fluxes of both heat and water molecules across the interface. Therefore, the resulting change in the refractive index of the $DyCl_3$ solution is affected by both the concentration and the temperature. To discriminate between the two contributions in the Mach-Zehnder interferometry approach, a new two-step compensation algorithm was developed and applied together with numerical simulations of the concentration and temperature fields. By these means, it could be clearly shown that more than 90% of the

refractive index increase in the boundary layer at the free surface most exposed to the field gradient is caused by the increase in the Dy(III) concentration. The close similarity of the present results to those obtained in seemingly closed cells furthermore conclusively proves the initial hypothesis that evaporation is the supporting process for the magnetic separation of RE ions.

To understand the mechanism of transport process with presence of FHD, the hydrostatics of the solution was analyzed. It is shown that the unbalanced radial component of the field gradient force is responsible for shaping the evaporation-driven concentration boundary layer into the observed concave shape. Generally, the evaporation-driven concentration boundary layer is hydrodynamically unstable, because it is heavier than the underlying bulk fluid. It is the field gradient force, acting in the opposite direction to gravity, which suppresses the resulting Rayleigh-Taylor instability. It was shown that the gravitational force acting on the boundary layer, expressed in a non-dimensional manner by the Rayleigh number, is drastically diminished by the approximately five times larger magnetic field gradient force. As a result, the supercritical value of the Rayleigh number is reduced to a subcritical one at which the Rayleigh-Taylor instability cannot set in. This is the origin of the observed levitation of the Dy(III) boundary layer in the magnetic field gradient.

Then, the competition between a change in the gravitational force and a change in the vertical magnetic field gradient force given a local concentration gradient is considered. A conservatively approximated stability criterion is calculated using a resulting Rayleigh number equivalent to 0. Thus, $\partial \Delta C/\partial z \,|_{Ra^*=0}$ as a function on the $f_{m,z}$ shows a singularity at $z = z_{crit} \approx 3$ mm. Both lines, $\partial \Delta C/\partial z = 0$ and $z = z_{crit}$, divide the stability behavior of the system into two regions of instability and two regions of stability, see Fig. 4.12. According to this stability diagram, the evaporation-driven enrichment layer is found above $z > z_{crit}$, i.e. in the zone where $f_{m,z}$ greatly dominates f_g and is therefore unconditionally stable in the present magnetic field. As a side product, a new susceptibility-driven instability is predicted provided $\partial \Delta C/\partial z > 0$ and $z < z_{crit}$, which should lead the solution to flow upwards.

Beside answering the important question of what mechanism underlies the observed magnetic separation of rare earth ions, the present study points to a series of issues in this process which have neither been addressed nor fully understood. As discussed above, a microconvection has to be responsible for the reshaping of the originally planar evaporation-driven boundary layer. There is a total lack of experimental insights into this type of convection. As a consequence, a more detailed stability analysis of the linearized Navier-Stokes equation [146] is desirable for a better understanding. This also holds for the predicted susceptibility-gradient-driven instability.

5.2 Future works

5.2.1 Validation of MHD convective heat transfer enhancement in MC

Works presented in Chapter 3 delivers a powerful measurement system for resolving heat transfer process between the solid state refrigerant and heat transfer fluid at the fluid side in magnetic cooling. Besides, a proof of principle is conveyed that MHD is potentially an effective way to enhance the heat transfer between the solid-state refrigerant and the heat transfer fluid. A further field validation of this method in sections of fluid which is driven by a hydraulic pressure drop is therefore demanding. The primary challenge evolves naturally which is to create a measurement chamber with adequate mechanical strength and sealing grade allowing force convection while guaranteeing a window of sufficient optical quality for the laser beam to enter. Therefore, a testing prototype made of plexiglass is designed and built.

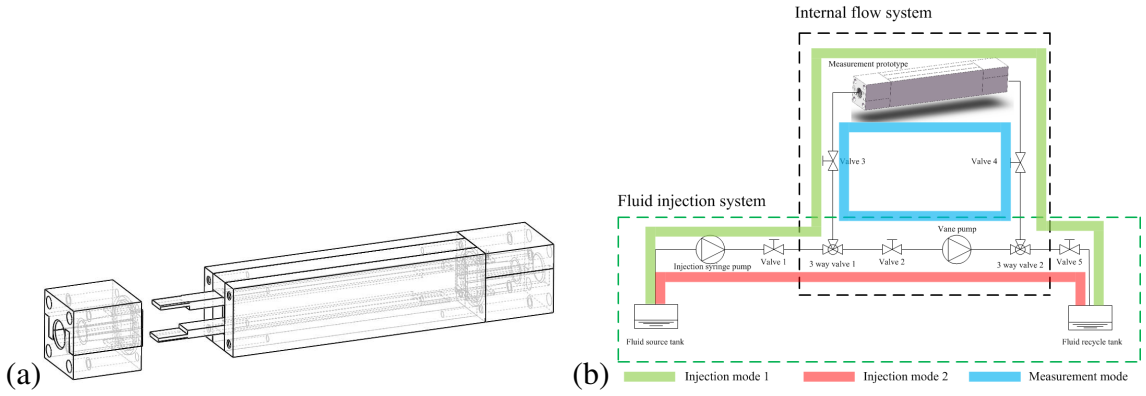

Fig. 5.1 High optical quality channel for interferometer measurement at hydraulic pressure drop-driven convection coupled to MHD convection: (a) Measurement channel mimicking an AMR regenerator bed, (b) internal flow system principle driven by vane pump with 3 modes.

The measurement section is allowed between two interferometer tested plexiglass wall with a fine surface roughness and optical transparency. The flow channel mimics a section of an active magnetic regenerator with a single flat MCM. The horizontal walls of the channel are replaceable by Gadolinium, from Goodfellow Corporation 99% pure, plates with dimension $50\times10\times l$ mm3 with l represent the thickness of the foils which are 0.5 mm, 1 mm and 2 mm, respectively. The internal flow is driven by a vane pump with a maximum flow rate of 100 l/h corresponding to Re = O(3000). Heat transfer investigations are done by placing this setup in a Mach-Zehnder interferometer in conjunction with thermocouples for the temperature distribution inside heat transfer fluid and MCM, respectively. Besides, a long term stable

operation of MHD in MC has to be ensured. This is especially important that a depletion of MCM has to be prevented in case of electrochemical reaction. A possible solution is an AC field with protect coating covering MCM plates. Therefore, a periodical sedimentation and dissolving of coated layer due to an alternating electrode takes place with a minimum lost of MCM material. Furthermore, velocity field of GaInSn flow under a periodically moving magnet needs to be resolved. The corresponding heat transfer investigation by means of conventional thermocouple needs to be carried under different flow fields.

5.2.2 Batch and continuous magnetic separation of REE with varying physical field

On the other hand, this dissertation clarifies a mechanism for a magnetic separation and its dynamics in transport process of mass. To proceed further, a batch or continuous separation technique needs to be developed for magnet assisted rare earth separation from solution. This could be either in a form of continuous separation channel or a batch processing comprising of multiple small chambers. Indeed, with the current separation speed and grade, a cascading principle is useful for a better separation. Besides, separation has to be tested in two rare earth salt solution system with a contrast in the resulting magnetic susceptibility, respectively.

Besides, stability analysis based on full Navier-Stokes equation, which is already mentioned in Sec. 4.6, is a pending research topic for a better defined stability diagram. The Kelvin force-induced instability which is predicted in the stability diagram, see Fig. 4.12b, needs to be experimentally verified.

Furthermore, this dissertation presents magnetic separation of paramagnetic rare earth ions from initially homogeneous solution with normal gravity and static magnetic field gradient force. The pressure field inside the solution is constituted of both the osmotic pressure and magnetic pressure. Essentially, the stability diagram is different when either physical field changes, see Fig. 4.12b. This motivates a magnetic separation experiment done under varying physical fields. Micro gravity, 0 g, and hypergravity, 1.8 g, are options for the varying gravitational field. Such conditions are provided by a parabolic flight experiment platform of a airplane which undergoes a number of repeating processes consisting of climbing, 1.8 g for approx. 22 s; an injection, 0 g for approx. 22 s; and a pull up, 1.8 g for approx. 22 s. The magnetic field, on the other hand, was provided by permanent magnets confined in a 3D printed non-magnetic structure. This was then integrated on a programmable electric mounting stage ensuring a varying magnetic field. During such a period, the double interferometer, see Fig. 2.4, is used to provide a real time concentration measurement. To allow for different conditions measurable in a single trial, a high precision

double containment measurement cell was designed and fabricated. Three of such cells are fixed on a 3D printed supporting structure connecting to a large seed cell. The whole setup was then integrated with a mounting stage controlled by computer which moves 3 cells into fixed interferometer measurement beam. This offers automatic batch measurement with different solution concentrations, cf. Fig. 5.2.

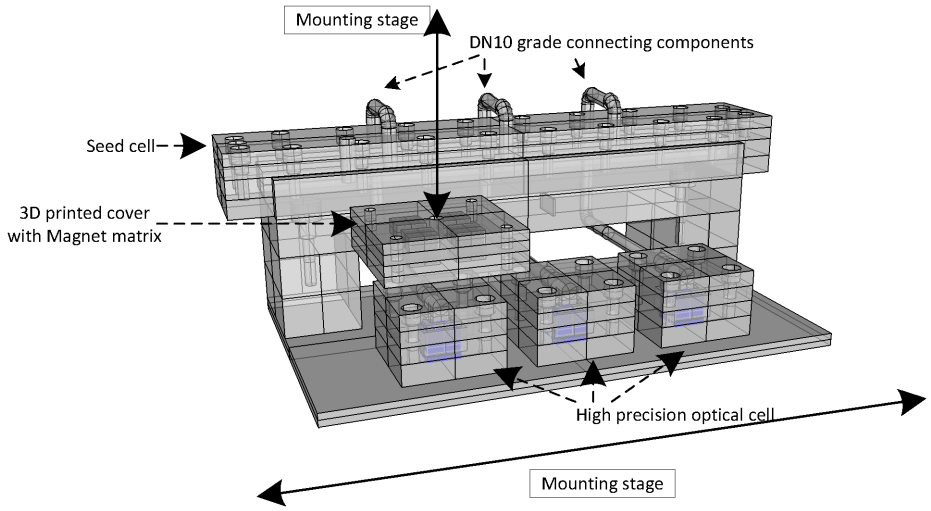

Fig. 5.2 High precision optical interferometry setup with combined automatic magnet matrix relocalization and relative position change inside the system.

The system robustness was tested and majority of the planned experiments were carried smoothly in 29th parabolic campaign of DLR (Deutsches Zentrum fuer Luft und Raumfahrt). A vibration of the laser beam turned out to be the last remaining issue to be resolved. The beam quality, without vibration compensation, was not ideal. This was induced by a vibration of relative movement of highly correlated pin hole and the convex lens in the spatial filter. This brings drastic amount of complexity in interferogram processing. Nonetheless, remaining hardware system and setup, software operation for automation and data sampling have robust operation under such extreme condition.

References

[1] U. G. S. U.S. Department of the Interior, Usgs mineral commodity summaries 2015, Tech. rep., U.S. Department of the Interior, U.S. Geological Survey (2015).

[2] U. G. S. U.S. Department of the Interior, U.s. geological survey-rare earth, Tech. rep., U.S. Department of the Interior, U.S. Geological Survey (2008).

[3] U. G. S. U.S. Department of the Interior, Usgs mineral commodity summaries 2016, Tech. rep., U.S. Department of the Interior, U.S. Geological Survey (2016).

[4] L. L. Rokhlin, Magnesium alloys containing rare earth metals: structure and properties, Crc Press, 2003.

[5] S. Kobayashi, M. Sugiura, H. Kitagawa, W. W.-L. Lam, Rare-earth metal triflates in organic synthesis, Chemical reviews 102 (6) (2002) 2227–2302.

[6] J. Du, Z. Li, Z. Da, M. He, Rare earth y-zeolite catalyst for cracking hydrocarbons and a method for preparing same, uS Patent 7,514, 385 (Apr. 7 2009).

[7] C. Ronda, T. Jüstel, H. Nikol, Rare earth phosphors: fundamentals and applications, Journal of Alloys and Compounds 275 (1998) 669–676.

[8] U. Nations, Paris agreement, Tech. rep., United Nations (2016).

[9] J. F. Gieras, Permanent magnet motor technology: design and applications, CRC press, 2002.

[10] H. Kirchmayr, Permanent magnets and hard magnetic materials, Journal of Physics D: Applied Physics 29 (11) (1996) 2763.

[11] J. Coey, Permanent magnet applications, J. Magn. Magn. Mater. 248 (3) (2002) 441–456.

[12] K. A. GschneidnerJr, V. Pecharsky, A. Tsokol, Recent developments in magnetocaloric materials, Reports on Progress in Physics 68 (6) (2005) 1479.

[13] K. Gschneidner Jr, V. Pecharsky, Thirty years of near room temperature magnetic cooling: Where we are today and future prospects, International Journal of Refrigeration 31 (6) (2008) 945–961.

[14] B. Yu, Q. Gao, B. Zhang, X. Meng, Z. Chen, Review on research of room temperature magnetic refrigeration, International Journal of Refrigeration 26 (6) (2003) 622–636.

[15] M. Isshiki, Purification of rare earth metals, Vacuum 47 (6) (1996) 885–887.

[16] J. S. Brown, P. A. Domanski, Review of alternative cooling technologies, Applied Thermal Engineering 64 (1) (2014) 252–262.

[17] A. Tishin, Y. Spichkin, Recent progress in magnetocaloric effect: Mechanisms and potential applications, International Journal of Refrigeration 37 (2014) 223–229.

[18] B. Yu, M. Liu, P. W. Egolf, A. Kitanovski, A review of magnetic refrigerator and heat pump prototypes built before the year 2010, International Journal of Refrigeration 33 (6) (2010) 1029–1060.

[19] E. Warburg, The thermodynamics of phase equilibrium, Ann. Phys 13 (1881) 1.

[20] V. Pecharsky, K. Gschneidner Jr, A. Pecharsky, A. Tishin, Thermodynamics of the magnetocaloric effect, Physical review B 64 (14) (2001) 144406.

[21] N. De Oliveira, P. Von Ranke, Theoretical aspects of the magnetocaloric effect, Physics Reports 489 (4) (2010) 89–159.

[22] A. Smith, C. R. Bahl, R. Bjørk, K. Engelbrecht, K. K. Nielsen, N. Pryds, Materials challenges for high performance magnetocaloric refrigeration devices, Advanced Energy Materials 2 (11) (2012) 1288–1318.

[23] L. Landau, The theory of phase transitions, Nature 138 (3498) (1936) 840–841.

[24] L. de Medeiros, N. de Oliveira, P. von Ranke, A. Troper, On the magnetocaloric effect of itinerant electron systems with first order transition, Physica A: Statistical Mechanics and its Applications 392 (6) (2013) 1355–1360.

[25] R. Santana, N. De Oliveira, P. Von Ranke, Magnetocaloric properties of compounds with first order phase transition: Hysteresis effect, Journal of Alloys and Compounds 509 (22) (2011) 6346–6349.

[26] T. F. Petersen, N. Pryds, A. Smith, J. Hattel, H. Schmidt, H.-J. Høgaard Knudsen, Two-dimensional mathematical model of a reciprocating room-temperature active magnetic regenerator, International Journal of Refrigeration 31 (3) (2008) 432–443.

[27] P. Li, M. Gong, G. Yao, J. Wu, A practical model for analysis of active magnetic regenerative refrigerators for room temperature applications, International Journal of Refrigeration 29 (8) (2006) 1259–1266.

[28] C. R. H. Bahl, K. K. Nielsen, The effect of demagnetization on the magnetocaloric properties of gadolinium, Journal of Applied Physics 105 (1) (2009) 013916.

[29] M. Kuzmin, K. Skokov, D. Y. Karpenkov, J. Moore, M. Richter, O. Gutfleisch, Magnetic field dependence of the maximum adiabatic temperature change, Applied Physics Letters 99 (1) (2011) 012501.

[30] G. Brown, Magnetic heat pumping near room temperature, Journal of Applied Physics 47 (8) (1976) 3673–3680.

[31] V. K. Pecharsky, K. A. Gschneidner, Advanced magnetocaloric materials: What does the future hold?, International Journal of Refrigeration 29 (8) (2006) 1239–1249.

[32] O. Gutfleisch, M. A. Willard, E. Brück, C. H. Chen, S. Sankar, J. P. Liu, Magnetic materials and devices for the 21st century: stronger, lighter, and more energy efficient, Advanced materials 23 (7) (2011) 821–842.

[33] K. G. Sandeman, Magnetocaloric materials: The search for new systems, Scripta Materialia 67 (6) (2012) 566–571.

[34] V. K. Pecharsky, K. A. Gschneidner Jr, Magnetocaloric effect and magnetic refrigeration, Journal of Magnetism and Magnetic Materials 200 (1) (1999) 44–56.

[35] S. Benford, G. Brown, T-s diagram for gadolinium near the curie temperature, Journal of Applied Physics 52 (3) (1981) 2110–2112.

[36] S. Y. DanKov, A. Tishin, V. Pecharsky, K. Gschneidner, et al., Magnetic phase transitions and the magnetothermal properties of gadolinium, Physical Review B 57 (6) (1998) 3478.

[37] Y. I. Spichkin, A. Derkach, A. Tishin, M. Kuzmin, A. Chernyshov, K. Gschneidner, V. Pecharsky, Thermodynamic features of magnetization and magnetocaloric effect near the magnetic ordering temperature of gd, Journal of Magnetism and Magnetic Materials 316 (2) (2007) e555–e557.

[38] A. Tishin, A. Derkach, Y. Spichkin, M. Kuzmin, A. Chernyshov, K. Gschneidner, V. Pecharsky, Magnetocaloric effect near a second-order magnetic phase transition, Journal of Magnetism and Magnetic Materials 310 (2) (2007) 2800–2804.

[39] R. Teyber, P. Trevizoli, T. Christiaanse, P. Govindappa, I. Niknia, A. Rowe, Permanent magnet design for magnetic heat pumps using total cost minimization, Journal of Magnetism and Magnetic Materials.

[40] A. Tura, A. Rowe, Permanent magnet magnetic refrigerator design and experimental characterization, International Journal of Refrigeration 34 (3) (2011) 628–639.

[41] J. A. Barclay, W. A. Steyert, Active magnetic regenerator, uS Patent 4,332,135 (Jun. 1 1982).

[42] W. Steyert, Stirling-cycle rotating magnetic refrigerators and heat engines for use near room temperature, Journal of Applied Physics 49 (3) (1978) 1216–1226.

[43] J. He, J. Chen, C. Wu, Heat-transfer effect on the performance of a magnetic ericsson refrigerator, Journal of Non-Equilibrium Thermodynamics 27 (1) (2002) 57–69.

[44] A. Kitanovski, J. Tušek, U. Tomc, U. Plaznik, M. Ožbolt, A. Poredoš, Active magnetic regeneration, in: Magnetocaloric Energy Conversion, Springer, 2015, pp. 97–166.

[45] O. Gutfleisch, K. Sandeman, Magnetic cooling: from fundamentals to high efficiency refrigeration, John Wiley & Sons, 2018.

[46] J. Barclay, The theory of an active magnetic regenerative refrigerator, in: Refrig. for for Cryogenic Sensors, Vol. 1, 1983, pp. 375–387.

[47] C. B. Zimm, A. Sternberg, A. G. Jastrab, A. M. Boeder, L. M. Lawton, J. J. Chell, Rotating bed magnetic refrigeration apparatus, uS Patent 6,526,759 (Mar. 4 2003).

[48] C. R. H. Bahl, K. Engelbrecht, R. Bjørk, D. Eriksen, A. Smith, K. K. Nielsen, N. Pryds, Design concepts for a continuously rotating active magnetic regenerator, International Journal of Refrigeration 34 (8) (2011) 1792–1796.

[49] J. Romero Gómez, R. Ferreiro Garcia, J. Carbia Carril, M. Romero Gómez, A review of room temperature linear reciprocating magnetic refrigerators, Renewable and Sustainable Energy Reviews 21 (2013) 1–12.

[50] K. L. Engelbrecht, G. F. Nellis, S. A. Klein, C. B. Zimm, Review article: recent developments in room temperature active magnetic regenerative refrigeration, HVAC&R Research 13 (4) (2007) 525–542.

[51] J. Tušek, A. Kitanovski, A. Poredoš, Geometrical optimization of packed-bed and parallel-plate active magnetic regenerators, International Journal of Refrigeration 36 (5) (2013) 1456–1464.

[52] T. F. Petersen, K. Engelbrecht, C. R. Bahl, B. Elmegaard, N. Pryds, A. Smith, Comparison between a 1D and a 2D numerical model of an active magnetic regenerative refrigerator, Journal of Physics D: Applied Physics 41 (10) (2008) 105002.

[53] J. Roudaut, A. Kedous-Lebouc, J.-P. Yonnet, C. Muller, Numerical analysis of an active magnetic regenerator, International Journal of Refrigeration 34 (8) (2011) 1797–1804.

[54] A. Tura, K. K. Nielsen, A. Rowe, Experimental and modeling results of a parallel plate-based active magnetic regenerator, International Journal of Refrigeration 35 (6) (2012) 1518–1527.

[55] F. Shir, C. Mavriplis, L. H. Bennett, E. D. Torre, Analysis of room temperature magnetic regenerative refrigeration, International Journal of Refrigeration 28 (4) (2005) 616–627.

[56] J. Tušek, A. Kitanovski, I. Prebil, A. Poredoš, Dynamic operation of an active magnetic regenerator (AMR): numerical optimization of a packed-bed AMR, International Journal of Refrigeration 34 (6) (2011) 1507–1517.

[57] C. Aprea, A. Greco, A. Maiorino, Modelling an active magnetic refrigeration system: A comparison with different models of incompressible flow through a packed bed, Applied Thermal Engineering 36 (2012) 296–306.

[58] A. Sarlah, A. Kitanovski, A. Poredos, P. W. Egolf, O. Sari, F. Gendre, C. Besson, Static and rotating active magnetic regenerators with porous heat exchangers for magnetic cooling, International Journal of Refrigeration 29 (8) (2006) 1332–1339.

[59] K. K. Nielsen, J. Tusek, K. Engelbrecht, S. Schopfer, A. Kitanovski, C. R. H. Bahl, A. Smith, N. Pryds, A. Poredos, Review on numerical modeling of active magnetic regenerators for room temperature applications, International Journal of Refrigeration 34 (3) (2011) 603–616.

[60] K. K. Nielsen, C. R. H. Bahl, A. Smith, R. Bjørk, N. Pryds, J. Hattel, Detailed numerical modeling of a linear parallel-plate active magnetic regenerator, International Journal of Refrigeration 32 (6) (2009) 1478–1486.

[61] J. Tušek, A. Kitanovski, S. Zupan, I. Prebil, A. Poredoš, A comprehensive experimental analysis of gadolinium active magnetic regenerators, Applied Thermal Engineering 53 (1) (2013) 57–66.

[62] K. Engelbrecht, D. Eriksen, C. Bahl, R. Bjørk, J. Geyti, J. Lozano, K. K. Nielsen, F. Saxild, A. Smith, N. Pryds, Experimental results for a novel rotary active magnetic regenerator, international journal of refrigeration 35 (6) (2012) 1498–1505.

[63] J. B. Jensen, K. Engelbrecht, C. R. Bahl, N. Pryds, G. F. Nellis, S. A. Klein, B. Elmegaard, Modeling of parallel-plate regenerators with non-uniform plate distributions, International Journal of Heat and Mass Transfer 53 (23) (2010) 5065–5072.

[64] D. Christensen, R. Bjørk, K. K. Nielsen, C. R. H. Bahl, A. Smith, S. Clausen, Spatially resolved measurements of the magnetocaloric effect and the local magnetic field using thermography, Journal of Applied Physics 108 (6) (2010) 063913.

[65] Z. Lei, X. Yang, C. Haberstroh, B. Pulko, S. Odenbach, K. Eckert, Space-and time-resolved interferometric measurements of the thermal boundary layer at a periodically magnetized gadolinium plate, International Journal of Refrigeration 56 (2015) 246–255.

[66] O. Sari, M. Balli, From conventional to magnetic refrigerator technology, International Journal of Refrigeration 37 (2014) 8–15.

[67] X. Yang, K. Eckert, K. Seidel, M. Uhlemann, The start-up of natural convection during copper electrolysis in the presence of an opposing Lorentz force, Electrochimica Acta 54 (2) (2008) 352–359.

[68] S. Mühlenhoff, G. Mutschke, D. Koschichow, X. Yang, A. Bund, J. Fröhlich, S. Odenbach, K. Eckert, Lorentz-force-driven convection during copper magnetoelectrolysis in the presence of a supporting buoyancy force, Electrochimica Acta 69 (2012) 209–219.

[69] S. Mühlenhoff, G. Mutschke, M. Uhlemann, X. Yang, S. Odenbach, J. Fröhlich, K. Eckert, On the homogenization of the thickness of Cu deposits by means of MHD convection within small dimension cells, Electrochemistry Communications 36 (2013) 80–83.

[70] Z. Lei, C. Haberstroh, S. Odenbach, K. Eckert, Heat transfer enhancement in magnetic cooling by means of magnetohydrodynamic convection, International Journal of Refrigeration 62 (2016) 166–176.

[71] Y. Chiba, Enhancements of thermal performances of an active magnetic refrigeration device based on nanofluids, Mechanics 23 (1) (2017) 31–38.

[72] Z. Lei, D. Raebiger, S. Eckert, K. Eckert, Liquid metal based magnetic cooling: velocity measurement, Magnetohydrodynamics (0024-998X) 53 (2).

[73] N. Morley, J. Burris, L. Cadwallader, M. Nornberg, Gainsn usage in the research laboratory, Review of Scientific Instruments 79 (5) (2008) 056107.

[74] U. Müller, L. Bühler, Magnetofluiddynamics in channels and containers, Springer Science & Business Media, 2013.

[75] Y. Plevachuk, V. Sklyarchuk, S. Eckert, G. Gerbeth, R. Novakovic, Thermophysical properties of the liquid ga–in–sn eutectic alloy, Journal of Chemical & Engineering Data 59 (3) (2014) 757–763.

[76] S. C. Chelgani, M. Rudolph, T. Leistner, J. Gutzmer, U. A. Peuker, A review of rare earth minerals flotation: monazite and xenotime, Int. J. Min. Sci. Technol. 25 (6) (2015) 877–883.

[77] N. Krishnamurthy, C. K. Gupta, Extractive metallurgy of rare earths, CRC press, 2004.

[78] A. Powell, Treatment of rare-earth minerals, British Patent 510.

[79] L. Shastri, J. Mittal, N. Krishnan, T. Murthy, Development of a photochemical route for upgrading europium from aqueous lanthanide mixtures, in: Materials Science Forum, Vol. 30, Trans Tech Publ, 1988, pp. 57–60.

[80] J. G. Parker, C. T. Baroch, J. Adams, Rare-earth elements, yttrium, and thorium. a materials survey., Tech. rep., Bureau of Mines, Washington, DC (1971).

[81] F. Xie, T. A. Zhang, D. Dreisinger, F. Doyle, A critical review on solvent extraction of rare earths from aqueous solutions, Miner. Eng. 56 (2014) 10–28.

[82] K. Binnemans, P. T. Jones, B. Blanpain, T. Van Gerven, Y. Yang, A. Walton, M. Buchert, Recycling of rare earths: a critical review, J. Clean. Prod. 51 (2013) 1–22.

[83] E. V. Kleber, B. Love, The technology of scandium, yttrium and the rare earth metals.

[84] B. Elvers, S. Hawkins, W. Russey, Ullmann's encyclopedia of industrial chemistry, Wiley Online Library, 1989.

[85] M. Simon, L. Heflinger, A. Geim, Diamagnetically stabilized magnet levitation, Am. J. Phys. 69 (6) (2001) 702–713.

[86] M. Simon, A. Geim, Diamagnetic levitation: flying frogs and floating magnets, J. Appl. Phys. 87 (9) (2000) 6200–6204.

[87] J. Oberteuffer, Magnetic separation: A review of principles, devices, and applications, IEEE T. Magn. 10 (2) (1974) 223–238.

[88] J. Svoboda, Magnetic techniques for the treatment of materials, Kluwer Academic Publisher, 2004.

[89] N. Pamme, C. Wilhelm, Continuous sorting of magnetic cells via on-chip free-flow magnetophoresis, Lab Chip 6 (8) (2006) 974–980.

[90] M. Franzreb, M. Siemann-Herzberg, T. J. Hobley, O. R. Thomas, Protein purification using magnetic adsorbent particles, Appl. Microbiol. Biotechnol. 70 (5) (2006) 505–516.

[91] L. Bromberg, E. P. Chang, C. Alvarez-Lorenzo, B. Magarinos, A. Concheiro, T. A. Hatton, Binding of functionalized paramagnetic nanoparticles to bacterial lipopolysaccharides and dna, Langmuir 26 (11) (2010) 8829–8835.

[92] M. Uhlemann, K. Tschulik, A. Gebert, G. Mutschke, J. Fröhlich, A. Bund, X. Yang, K. Eckert, Structured electrodeposition in magnetic gradient fields, Eur. Phys. J. Spec. Top. 220 (1) (2013) 287–302.

[93] L. M. Monzon, J. Coey, Magnetic fields in electrochemistry: The kelvin force. a mini-review, Electrochem. Commun. 42 (2014) 42–45.

[94] N. Leventis, X. Gao, Magnetohydrodynamic electrochemistry in the field of nd- fe- b magnets. theory, experiment, and application in self-powered flow delivery systems, Anal. Chem. 73 (16) (2001) 3981–3992.

[95] G. Mutschke, K. Tschulik, T. Weier, M. Uhlemann, A. Bund, J. Froehlich, On the action of magnetic gradient forces in micro-structured copper deposition, Electrochim. Acta 55 (28) (2010) 9060–9066.

[96] K. Ngamchuea, K. Tschulik, R. G. Compton, Magnetic control: Switchable ultrahigh magnetic gradients at fe3o4 nanoparticles to enhance solution-phase mass transport, Nano Res. 8 (10) (2015) 3293–3306.

[97] P. Dunne, J. Coey, Patterning metallic electrodeposits with magnet arrays, Physical Review B 85 (22) (2012) 224411.

[98] K. Tschulik, C. Cierpka, G. Mutschke, A. Gebert, L. Schultz, M. Uhlemann, Clarifying the mechanism of reverse structuring during electrodeposition in magnetic gradient fields, Anal. Chem. 84 (5) (2012) 2328–2334.

[99] X. Yang, K. Tschulik, M. Uhlemann, S. Odenbach, K. Eckert, Enrichment of paramagnetic ions from homogeneous solutions in inhomogeneous magnetic fields, J. Phys. Chem. Lett. 3 (23) (2012) 3559–3564.

[100] O. Y. Gorobets, Y. I. Gorobets, I. Bondar, Y. A. Legenkiy, Quasi-stationary heterogeneous states of electrolyte at electrodeposition and etching process in a gradient magnetic field of a magnetized ferromagnetic ball, J. Magn. Magn. Mater. 330 (2013) 76–80.

[101] X. Yang, K. Tschulik, M. Uhlemann, S. Odenbach, K. Eckert, Magnetic separation of paramagnetic ions from initially homogeneous solutions, IEEE T. Magn. 50 (11) (2014) 4600804.

[102] B. Pulko, X. Yang, Z. Lei, S. Odenbach, K. Eckert, Magnetic separation of dy (iii) ions from homogeneous aqueous solutions, Appl. Phys. Lett. 105 (23) (2014) 232407.

[103] C. Udagawa, A. Maeda, A. Katsuki, S. Maki, S. Morimoto, Y. Tanimoto, Magnetic field effects on copper metal deposition from copper sulfate aqueous solution, J. Phys. Chem. B 118 (18) (2014) 4889–4894.

[104] O. Y. Gorobets, Y. I. Gorobets, V. Rospotniuk, Magnetophoretic potential at the movement of cluster products of electrochemical reactions in an inhomogeneous magnetic field, Journal of Applied Physics 118 (7) (2015) 073902.

[105] X. Jiang, J. Qiao, I. M. Lo, L. Wang, X. Guan, Z. Lu, G. Zhou, C. Xu, Enhanced paramagnetic cu 2+ ions removal by coupling a weak magnetic field with zero valent iron, Journal of hazardous materials 283 (2015) 880–887.

[106] K. Kołczyk, M. Wojnicki, D. Kutyła, R. Kowalik, P. Żabiński, A. Cristofolini, Separation of ho3+ in static magnetic field, Archives of Metallurgy and Materials 61 (4) (2016) 1919–1924.

[107] A. Franczak, K. Binnemans, J. Fransaer, Magnetomigration of rare-earth ions in inhomogeneous magnetic fields, Physical Chemistry Chemical Physics.

[108] K. Binnemans, P. T. Jones, B. Blanpain, T. Van Gerven, Y. Pontikes, Towards zero-waste valorisation of rare-earth-containing industrial process residues: a critical review, J. Clean. Prod. 99 (2015) 17–38.

[109] O. Y. Gorobets, Y. I. Gorobets, V. Rospotniuk, A. Kyba, Y. A. Legenkiy, Liquid-liquid phase separation occurring under the influence of inhomogeneous magnetic field in the process of the metal deposition and etching of the magnetized ferromagnetic ball, Journal of Solid State Electrochemistry 19 (10) (2015) 3001–3012.

[110] J. M. D. Coey, R. Aogaki, F. Byrne, P. Stamenov, Magnetic stabilization and vorticity in submillimeter paramagnetic liquid tubes, Proceedings of the National Academy of Sciences 106 (22) (2009) 8811–8817.

[111] Z. Lei, B. Fritzsche, K. Eckert, Evaporation-assisted magnetic separation of rare-earth ions in aqueous solutions, The Journal of Physical Chemistry C 121 (44) (2017) 24576–24587.

[112] R. E. Rosensweig, Ferrohydrodynamics, Courier Corporation, 2013.

[113] P. A. Davidson, An introduction to magnetohydrodynamics, Vol. 25, Cambridge university press, 2001.

[114] J. M. Coey, Magnetism and magnetic materials, Cambridge University Press, 2010.

[115] B. Pulko, X. Yang, Z. Lei, S. Odenbach, K. Eckert, Magnetic separation of dy (iii) ions from homogeneous aqueous solutions, Applied Physics Letters 105 (23) (2014) 232407.

[116] W. M. Haynes, CRC handbook of chemistry and physics, CRC press, 2014.

[117] P. Sipos, A. Stanley, S. Bevis, G. Hefter, P. M. May, Viscosities and densities of concentrated aqueous NaOH/NaAl (OH) 4 mixtures at 25°C, Journal of Chemical & Engineering Data 46 (3) (2001) 657–661.

[118] M. C. F. Magalhães, E. Königsberger, P. M. May, G. Hefter, Heat capacities of concentrated aqueous solutions of sodium sulfate, sodium carbonate, and sodium hydroxide at 25°C, Journal of Chemical & Engineering Data 47 (3) (2002) 590–598.

[119] Z. Lei, K. Eckert, Towards a quantitative analysis of spatial and temporal resolution of mach-zehnder interferometer.

[120] R. M. Rao, A. S. Bopardikar, Wavelet transforms-introduction to theory and applications., Addison-Wesley-Longman, 1997.

[121] D. C. Ghiglia, M. D. Pritt, Two-dimensional phase unwrapping: theory, algorithms, and software, Wiley New York, 1998.

[122] G. Mie, Beiträge zur optik trüber medien, speziell kolloidaler metallösungen, Annalen der physik 330 (3) (1908) 377–445.

[123] C. Kasai, K. Namekawa, A. Koyano, R. Omoto, Real-time two-dimensional blood flow imaging using an autocorrelation technique, IEEE Transactions on sonics and ultrasonics 32 (3) (1985) 458–464.

[124] I. Lashuk, A. Chandramowlishwaran, H. Langston, T.-A. Nguyen, R. Sampath, A. Shringarpure, R. Vuduc, L. Ying, D. Zorin, G. Biros, A massively parallel adaptive fast-multipole method on heterogeneous architectures, in: Proceedings of the Conference on High Performance Computing Networking, Storage and Analysis, ACM, 2009, p. 58.

[125] L. Ying, G. Biros, D. Zorin, H. Langston, A new parallel kernel-independent fast multipole method, in: Supercomputing, 2003 ACM/IEEE Conference, IEEE, 2003, pp. 14–14.

[126] I. Lashuk, A. Chandramowlishwaran, H. Langston, T.-A. Nguyen, R. Sampath, A. Shringarpure, R. Vuduc, L. Ying, D. Zorin, G. Biros, A massively parallel adaptive fast multipole method on heterogeneous architectures, Communications of the ACM 55 (5) (2012) 101–109.

[127] H. Langston, Parallel algorithms for data analysis and simulation, http://padas.ices.utexas.edu/software/.

[128] J. H. Ferziger, M. Peric, Computational methods for fluid dynamics, Springer Science & Business Media, 2012.

[129] S. Patankar, Numerical heat transfer and fluid flow, CRC press, 1980.

[130] W.-Q. Tao, Numerical heat transfer, Vol. 220, Xi'an Jiaotong University Press, Xi'an, 2001 (in Chinese).

[131] Z. Lei, K. Eckert, Interferometric measurement of the heat transfer enhancement driven by a magnetohydrodynamic flow at a magnetized gadolinium plate, in: International Conference of Refrigeration, Yokohama, Japan, 2015.

[132] A. Smith, K. K. Nielsen, D. Christensen, C. R. H. Bahl, R. Bjørk, J. Hattel, The demagnetizing field of a nonuniform rectangular prism, Journal of Applied Physics 107 (10) (2010) 103910.

[133] M. Rahman, Q. Galand, M. Soliman, S. Van Vaerenbergh, M. Saghir, Measurement of refractive indices of binary mixtures using digital interferometry and multi-wavelength abbemat refractometer, Optics and Lasers in Engineering 51 (5) (2013) 503–513.

[134] R. Bjørk, C. R. H. Bahl, M. Katter, Magnetocaloric properties of lafe 13- x- y co x si y and commercial grade gd, Journal of Magnetism and Magnetic Materials 322 (24) (2010) 3882–3888.

[135] M. Griffel, R. Skochdopole, F. Spedding, The heat capacity of gadolinium from 15 to 355 k, Physical Review 93 (4) (1954) 657.

[136] G. Bednarz, D. Geldart, M. A. White, Heat capacity of gadolinium near the curie temperature, Physical Review B 47 (21) (1993) 14247.

[137] D. Simons, M. Salamon, Specific heat and resistivity of gadolinium near the curie point in external magnetic fields, Physical Review B 10 (11) (1974) 4680.

[138] P. A. Nikrityuk, K. Eckert, R. Grundmann, Numerical study of a laminar melt flow driven by a rotating magnetic field in enclosed cylinders with different aspect ratios, Acta Mechanica 186 (1-4) (2006) 17–35.

[139] X. Yang, K. Eckert, S. Mühlenhoff, S. Odenbach, On the decay of the Lorentz-force-driven convection in vertical concentration stratification during magnetoelectrolysis, Electrochimica Acta 54 (27) (2009) 7056–7065.

[140] S. Eckert, G. Gerbeth, Velocity measurements in liquid sodium by means of ultrasound doppler velocimetry, Experiments in Fluids 32 (5) (2002) 542–546.

[141] T. Vogt, D. Räbiger, S. Eckert, Inertial wave dynamics in a rotating liquid metal, Journal of Fluid Mechanics 753 (2014) 472–498.

[142] Z. Lei, D. Raebiger, S. Eckert, K. Eckert, Liquid metal based magnetic cooling: velocity measurements, in: proceedings PAMIR 2016, 2016.

[143] O. Zikanov, D. Krasnov, T. Boeck, A. Thess, M. Rossi, Laminar-turbulent transition in magnetohydrodynamic duct, pipe, and channel flows, Applied Mechanics Reviews 66 (3) (2014) 030802.

[144] C. F. Baes, R. E. Mesmer, et al., Hydrolysis of cations, Wiley, 1976.

[145] G. Mutschke, K. Tschulik, M. Uhlemann, A. Bund, J. Froehlich, Comment on magnetic structuring of electrodeposits, Phys. Rev. Lett. 109 (22) (2012) 229401.

[146] S. Chandrasekhar, Hydrodynamic and hydromagnetic stability, Courier Corporation, 2013.

[147] B. Finlayson, Convective instability of ferromagnetic fluids, Journal of Fluid Mechanics 40 (04) (1970) 753–767.

[148] L. Schwab, Thermal convection in ferrofluids under a free surface, J. Magn. Magn. Mater. 85 (1-3) (1990) 199–202.

[149] H. Engler, S. Odenbach, Parametric modulation of thermomagnetic convection in magnetic fluids, J. Phys.: Condens. Matter 20 (20) (2008) 204135.

[150] A. Lange, S. Odenbach, Patterns of thermomagnetic convection in magnetic fluids subjected to spatially modulated magnetic fields, Phys. Rev. E 83 (6) (2011) 066305.

[151] M. Cowley, R. E. Rosensweig, The interfacial stability of a ferromagnetic fluid, Journal of Fluid mechanics 30 (04) (1967) 671–688.